

**BULETINUL
INSTITUTULUI
POLITEHNIC
DIN IAȘI**

Tomul LVI (LX)

Fasc. 3

ȘTIINȚA ȘI INGINERIA MATERIALELOR

2010

Editura POLITEHNIUM

BULETINUL INSTITUTULUI POLITEHNIC DIN IAȘI
PUBLISHED BY
„GHEORGHE ASACHI” TECHNICAL UNIVERSITY OF IAȘI
Editorial Office: Bd. D. Mangeron 63, 700050, Iași, ROMANIA
Tel. 40-232-278683; Fax: 40-232 237666; e-mail: polytech@mail.tuiasi.ro

Editorial Board

President : Prof.dr.eng. **Ion Giurma**, Member of the Academy of Agricultural Sciences and Forest, *Rector* of the "Gheorghe Asachi" Technical University" of Iași

Editor-in -Chief : Prof.dr.eng. **Carmen Teodosiu**, *Vice-Rector* of the "Gheorghe Asachi" Technical University of Iași

Honorary Editors of the Bulletin: Prof.dr.eng. **Alfred Braier**

Prof.dr.eng. **Hugo Rosman**

Prof.dr.eng. **Mihail Voicu**, Corresponding Member of the Romanian Academy, *President* of the "Gheorghe Asachi" Technical University of Iași

Editors in Chief of the MATERIALS SCIENCE AND ENGINEERING Section

Assoc. prof. dr. eng. **Iulian Ioniță**

Assoc. prof. dr. eng. **Gheorghe Bădărău**

Prof. dr. eng. **Petrică Vizureanu**

Honorary Editors: Prof. dr. eng. **Dan Gelu Gălușcă**

Prof. dr. eng. **Adrian Dima**

Associated Editor: Assoc. prof. dr. eng. **Ioan Rusu**

Editorial Advisory Board

Prof.dr.eng. **Agustin Santana Lopez**, La Palmas de Gran Canaria University (Spain)

Prof.dr.eng. **Julia Mirza Rosca**, La Palmas de Gran Canaria University (Spain)

Prof.dr.eng. **Roy Buchan**, Colorado State University (U.S.A.)

Prof.dr.eng. **Yuri A. Burennikov**, Vinnitsya National Technical University (Ukraine)

Prof.dr.hab. **Zbigniew Gronostajski**, Technical University of Wroclaw (Poland)

Prof. dr. **Oronzio Manca**, Seconda Università degli Studi di Napoli (Italy)

Assoc. prof. **Shizutoshi Ando**, Tokyo University of Sciences (Japan)

Dr. **Koichi Tsuchiya**, National Institute for Materials Science (Japan)

Dr.eng. **Burak Özkal**, Istanbul Technical University (Turkey)

Prof. dr. eng. **Vasile Cojocaru-Filipiuc**, "Gheorghe Asachi" Technical University of Iași (Romania)

Prof. dr. eng. **Constantin Baciu**, "Gheorghe Asachi" Technical University of Iași (Romania)

Prof. dr. **Viorel Păun**, University "Politehnica" Bucharest (Romania)

ȘTIINȚA ȘI INGINERIA MATERIALELOR

SUMAR

	<u>Pag.</u>
DRAGOȘ CRISTIAN ACHIȚEI, DAN-GELU GĂLUȘCĂ, PETRICĂ VIZUREANU și ROXANA-GABRIELA ȘTEFĂNICĂ, Aplicații biomedicale ale aliajelor cu memoria formei (engl. rez. rom.)	9
MIHAI APREUTESEI, IONELA ROXANA ARVINTE și DIDA CONSTANTIN, Proprietățile electrice ale straturilor subțiri de tip ZrO_x obținute prin pulverizare reactivă în sistem magnetron (engl. rez. rom.)	17
MARIUS BENȚA, MARIN CLAUDIU GARGAZ, ANCA IFTODE și ȘTEFAN HULUȚA, Cercetarea experimentală a metodelor de măsurare a suprafețelor metalice (engl. rez. rom.)	27
EMIL BRUJ, DOREL NEMEȘ și VALENTIN MOLDOVAN, Studiu comparativ asupra obținerii agenților poroși din pulberi de NaCl (engl. rez. rom.)	33
DOREL BUTNACIUC, DAN-GELU GĂLUȘCĂ, MIHAI DUMITRU și NICANOR CIMPOEȘU, Curgerea și solidificarea componentelor de tăiere cu ajutorul simulării numerice (engl. rez. rom.)	41
DOREL BUTNACIUC, DAN-GELU GĂLUȘCĂ, MIHAI DUMITRU și NICANOR CIMPOEȘU, Simularea solidificării și umplerii a unui proces de turnare în vederea obținerii unei piese tip corp (engl. rez. rom.)	51
SANDA CREȚU și DAN-GELU GĂLUȘCĂ, Cercetări privind analiza aderenței zonei de îmbinare a bușelor metalice (engl. rez. rom.)	59
BOGDAN-LUCIAN GAVRILĂ, MIHAI SUSAN, PETRU DUMITRAȘ, DRAGOȘ CRISTIAN ACHIȚEI, VIOREL ILIESCU și BRIAN-TUDOR LANDKAMMER, Analiza efectului de suprafață al ultrasunetelor la tragerea țevilor în sistem SONODRAW (engl. rez. rom.)	65

ADRIAN GRECU, DAN-GELU GĂLUȘCĂ, CARMEN NEJNERU și NICANOR CIMPOEȘU, Influența temperaturii apei asupra răcirii materialelor (engl. rez. rom.)	77
BRIAN-TUDOR C. LANDKAMMER, BOGDAN GAVRILĂ, MIHAI SUSAN și CONSTANTIN BACIU, Unele considerații asupra procedului de durificare și finisare cu vibrații ultrasonice (engl. rez. rom.)	83
RĂZVAN IULIAN LIȚOIU, ANCA ELENA LĂRGEANU și ZERICHIOTIS IOANNIS, Transportul de impuls în materialele fractale (engl. rez. rom.)	91
LAURENȚIU MARIN și ADRIAN DIMA, Cercetări asupra schimbărilor structurale din fonta încălzită cu sursă concentrată de laser GIC200 pentru a crește rezistența la uzură (engl. rez. rom.)	97
MIHAELA MARIN și ELENA DRUGESCU, Studiul influenței carburării asupra produselor sinterizate (engl. rez. rom.)	103
VALENTIN MOLDOVAN, DOREL NEMEȘ și EMIL BRUJ, Factorii de influența ai sedimentării centrifugale (engl. rez. rom.)	113
DOREL-ȘTEFAN NEMEȘ, EMIL BRUJ și VALENTIN MOLDOVAN, Materiale poroase obținute prin anodizarea aluminiului (engl. rez. rom.)	121
TIBERIU POTECASU, Sistem acustic de control al calității produselor ceramice	125
BOGDAN PRICOP, NICOLETA-MONICA LOHAN (MAHU) și LEANDRU GHEORGHE BUJOREANU, Efectele ciclării asupra reversiei martensitei în AMF pe bază de Cu (engl. rez. rom.)	135
EMANUELA DANIELA STOICA, Cercetare privind pregătirea implanturilor protetice (engl. rez. rom.)	143
IRINA-ELENA SURDU și DAN-GELU GĂLUȘCĂ, Ce este depunerea chimică de vapori (C-CVD)? (engl. rez. rom.)	151

MATERIALS SCIENCE AND ENGINEERING

CONTENTS

	<u>Pp.</u>
DRAGOȘ CRISTIAN ACHIȚEI, DAN-GELU GĂLUȘCĂ, PETRICĂ VIZUREANU and ROXANA-GABRIELA ȘTEFĂNICĂ, Biomedical Applications of Shape Memory Alloys (English, Romanian summary) . .	9
MIHAI APREUTESEI, IONELA ROXANA ARVINTE and DIDA CONSTANTIN, Electrical Properties of ZrO _x Thin Films Prepared by Reactive Magnetron Sputtering (English, Romanian summary)	17
MARIUS BENȚA, MARIN CLAUDIU GARGAZ, ANCA IFTODE and ȘTEFAN HULUȚA, Experimental Research on the Measuring Methods of Metallic Surfaces (English, Romanian summary).	27
EMIL BRUJ, DOREL NEMEȘ and VALENTIN MOLDOVAN, Comparative Study on Obtaining Porous Agents from NaCl Powders (English, Romanian summary)	33
DOREL BUTNACIUC, DAN-GELU GĂLUȘCĂ, MIHAI DUMITRU and NICANOR CIMPOEȘU, Metal Flow and Solidification of Blade Type Components Numerical Simulation Results (English, Romanian summary)	41
DOREL BUTNACIUC, DAN-GELU GĂLUȘCĂ, MIHAI DUMITRU, NICANOR CIMPOEȘU, Filling and Solidification Simulation of a Molding Process Concerning Obtaining of a Body Piece (English, Romanian summary)	51
SANDA CREȚU and DAN-GELU GĂLUȘCĂ, Research on Analysis of Joint Area Bimetallic Bushes Grip (English, Romanian summary).	59
BOGDAN-LUCIAN GAVRILĂ, MIHAI SUSAN, PETRU DUMITRAȘ, DRAGOȘ CRISTIAN ACHIȚEI, VIOREL ILIESCU and BRIAN-TUDOR LANDKAMMER, Analysis of the Ultrasounds Surface Effect During the Tubes Drawing in SONODRAW System (English, Romanian summary)	65

ADRIAN GRECU, DAN-GELU GĂLUȘCĂ, CARMEN NEJNERU and NICANOR CIMPOEȘU, Water Temperature Influence on Metallic Materials Cooling (English, Romanian summary).	77
BRIAN-TUDOR C. LANDKAMMER, BOGDAN GAVRILĂ, MIHAI SUSAN and CONSTANTIN BACIU, Some Considerations Concerning the Hardening and Finishing Proceeding with Ultrasonic Vibrations (English, Romanian summary).	83
RĂZVAN IULIAN LIȚOIU, ANCA ELENA LĂRGEANU and ZERICHIOTIS IOANNIS, On the Momentum Transport in the Fractal Materials (English, Romanian summary).	91
LAURENȚIU MARIN and ADRIAN DIMA, Research on Structural Changes of Cast Iron Heated with Concentrated Sources GIC200 Laser Beam of Electrons to Increase Wear Resistance (English, Romanian summary) . .	97
MIHAELA MARIN and ELENA DRUGESCU, A Study of Influence of Carburizing on Sintered Products (English, Romanian summary)	103
VALENTIN MOLDOVAN, DOREL NEMEȘ and EMIL BRUJ, Influencing Factors of Centrifugal Sedimentation Process (English, Romanian summary)	113
DOREL-ȘTEFAN NEMEȘ, EMIL BRUJ and VALENTIN MOLDOVAN, Porous Materials Obtained by Aluminum Anodization (English, Romanian summary)	121
TIBERIU POTECASU, Acoustic Quality Control System for Ceramic Products (English, Romanian summary).	125
BOGDAN PRICOP, NICOLETA-MONICA LOHAN (MAHU) and LEANDRU GHEORGHE BUJOREANU, Cycling Effects on Martensite Reversion in Cu-Based SMAs (English, Romanian summary).	135
EMANUELA-DANIELA STOICA, Preparation of Prosthetic Implants Research (English, Romanian summary).	143
IRINA-ELENA SURDU and DAN-GELU GĂLUȘCĂ, What is Submitted by Chemical Vapor (C-CVD)? (English, Romanian summary).	151

BIOMEDICAL APPLICATIONS OF SHAPE MEMORY ALLOYS

BY

**DRAGOȘ CRISTIAN ACHIȚEI, DAN-GELU GĂLUȘCĂ,
PETRICĂ VIZUREANU and ROXANA-GABRIELA ȘTEFĂNICĂ**

Abstract. Shape memory alloys found in various biomedical applications. The paper presents a documentary synthesis of these applications and some chemical-metallurgical issues related to their biocompatibility.

Key words: shape memory alloys, biomaterials, corrosion, prostheses.

1. Introduction

Biomaterials are synthetic materials used to replace a part of a living system or to function closely with a living tissue.

Most commonly known are metallic biomaterials. Living tissues in very small quantities tolerate most metallic materials, Fe, Cr, Co, Ni, Ti, Ta, Mo and W, used for most implants, although some metallic elements are essential for cellular functions.

A special category of biomaterials is shape memory alloys, which after plastic deformation return, by heating, to the initial shape. It provides medical applications such as for intracranial aneurysms, filters for vena cava, orthopedic implants etc.

Vanadium was the first metal used in the manufacture of plates and screws used for bone fractures. Human body can accept the most metals used for implants within few minutes.

Biocompatibility of metallic implants is a problem because they tend to corrode into hostile environments. The consequence of corrosion is loss of material, which weakens the strength of the implant and perhaps even more important than that, corrosion produces damages in tissues, leading to unwanted effects.

2. Medical Applications of Shape Memory Alloys

Shape memory alloys are a unique group of alloys with the ability to remember a form even after quite severe plastic deformations.

At low temperatures, shape memory alloys can be deformed apparently like other metallic alloys, but this deformation can recover with a relatively modest increase in temperature. This behavior is called shape memory effect.

Alloys with perfect shape memory effect are listed in the table below as follows:

Table 1
Materials, Composition, Structural Transformation

No.	Alloy	Composition % (at.)	Structural transformation
1	Ag – Cd	44 – 49 Cd	$B_2 \rightarrow 2H$
2	Au – Cd	46.5 – 50 Cd	$B_2 \rightarrow 2H$
3	Cu – Zn	38.5 – 41.5 Zn	$B_2 \rightarrow 9R$ rhombohedra M9R
4	Cu – Zn – X X = Si, Sn, Al, Ga	X = max. 4%	$B_2 (DO_3) \rightarrow 9R$ M9R (18R, M18R)
5	Cu – Al – Ni	28 – 29 Al 3 – 4.5 Ni	$DO_3 \rightarrow 2H$
6	Cu – Sn	15 Sn	$DO_3 \rightarrow 2H, 18R$
7	Cu – Au – Zn	23 – 28 Au 45 – 47 Zn	Heusler $\rightarrow 18R$
8	Ni – Al	36 – 38 Al	$B_2 - 3R$
9	Ti – Ni	49 – 51 Ni	$B_2 \rightarrow B19$ monoclinic $B_2 \rightarrow$ rhombohedric \rightarrow monoclinic
10	Fe – Pt	~ 25 Pt	$L_{12} \rightarrow$ t.v.c. ordinate
11	In – Ti	18 – 23 Ti	c.f.c. \rightarrow t.f.c.
12	In – Cd	4 – 5 Cd	c.f.c. \rightarrow t.f.c.
13	Mn – Cd	5 – 35 Cd	c.f.c. \rightarrow t.f.c.
14	Fe – Pd	~ 30 Pd	c.f.c. \rightarrow t.f.c.

These features allow the use of shape memory alloys in smart structures, micro actuators, some advanced composites, medical and dental implants.

These types of materials are porous materials made of shape memory alloys and used in medicine to replace certain bone parts.

In time, the organism will embed them, by developing inside the pores of characteristic organic bone cells.

Table 2
Medical Applications of Shape Memory Alloys Present Bellow

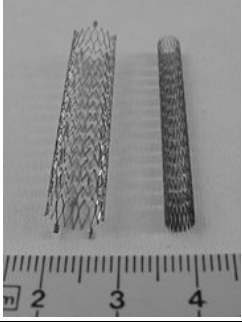
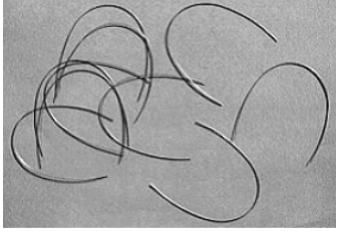
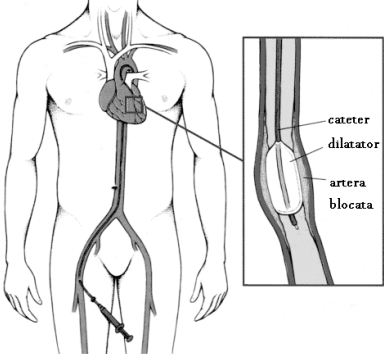
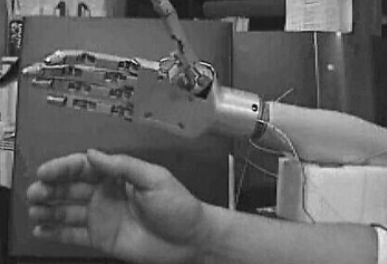
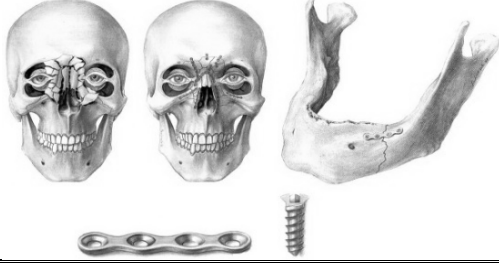
Coronary dilator	
Drilling tools	
Clips and clamps for bone system	
Arch wires for dental corrections	
Frames for glasses	

Table 2
Continuation

Laser cutter	
Dilator for blocked arteries	 <p>Diagram illustrating the use of a dilator for blocked arteries. The main diagram shows a human torso with a catheter and dilator inserted into the neck. The inset diagram shows a cross-section of an artery with a dilator and a blocked artery (artera blocata).</p>
Brain spatula	
Locomotors prostheses	
Recovery elements of bone structures (clips & screws)	

In this way, internal micro prosthesis integrates with the entire body and within with only a minimum risk of side effects.

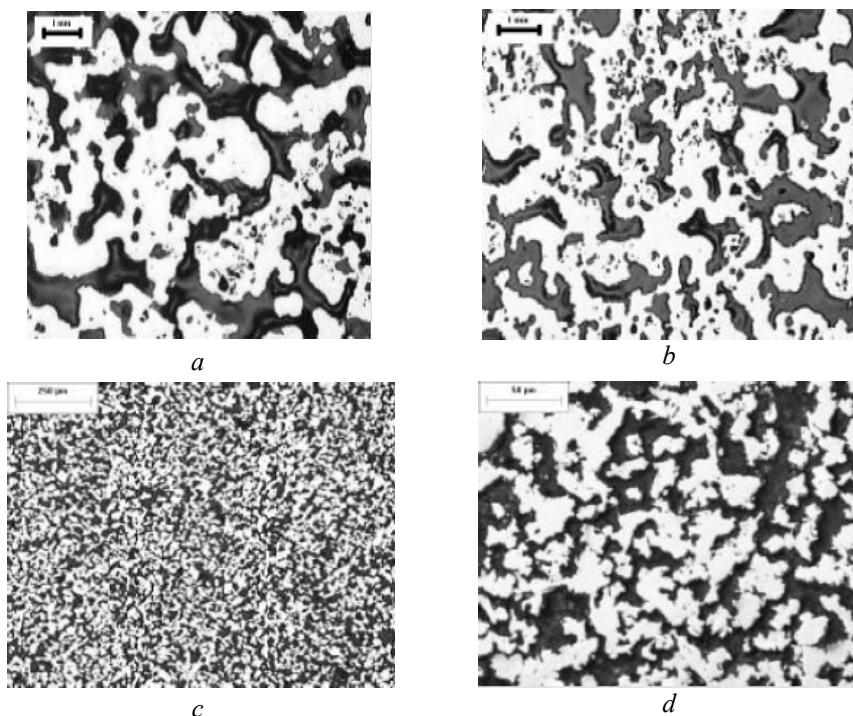


Fig. 1 – *a, b* – large pores: porosity 42% ; scale 2.5x ;
c, d – large pores: porosity 50% ; scale 10x, respective 50x.

Porous materials used in medical field for prostheses present besides the above mentioned biocompatibility and elastic proprieties, mimicking the behavior of bone part that substitute.

In the last 25...30 years points out a great diversification of metallic alloys in the field of dental materials used to realize the gnato-prosthetic devices.

Diversification has been made towards achieving both superior material proprieties, both in terms of biocompatibility and physiognomic appearance, but with high prices, as well as achieving not noble metallic alloys (alloys of nickel or chromium, cobalt or titanium – with improved composition) or inferior alloys (brasses and bronzes) – with extremely low prices.

Copper alloys, initially used as training alloys, has begun to be promoted as dental alloys from the seventh decade of last century, from economic reasons – due to the significant increase in the price of precious metals.

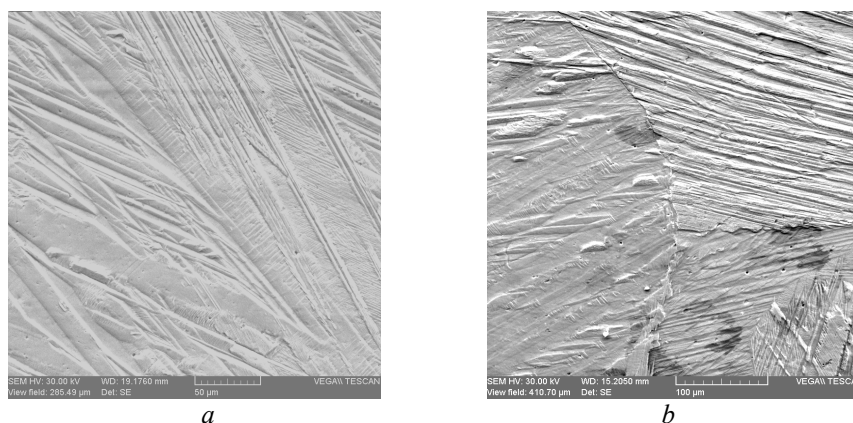


Fig. 2 – Microstructures of shape memory alloys type CuZnAl:
a – x1000, cast state; *b* – x700, forged state.

In many countries, particularly in Europe, and a series of prosthetic clinics in Romania, copper alloys are considered incompatible with the qualities required to some prosthetic biomaterials, being presented as risk materials. They present cytotoxic or allergic risk and have low resistance to corrosion placing them at the inferior limit of acceptability.

After nearly three decades of use *in vivo* has imposed the need for more careful studies on the behavior and properties of these materials, with respect to chemical composition, cytotoxicity, and corrosion.

Copper and its alloys are recognized as materials with good corrosion resistance and thus, they use in many fields. Good resistance of these materials is related to the formation of a uniform and adherent film (oxides, hydroxides etc.) protecting the substrate from the environment.

Corrosion phenomenon is related to the formation and stability of this film. If the film is not formed or is destroyed, the metal is corroded generalized – on the entire surface, or localized (crevices, cracks, pitting corrosions).

Protective oxide film destroys locally when environment composition changes, increasing the concentration of aggressive ions (Cl^- , SO_4^{2-} , etc.) while decreasing the oxygen content of the solution.

Copper is an essential metal for living organisms, but too much copper can harm if it is in a biological available form. However, the biologic impact of any available excess depends on environmental factors interacting with the organism.

The excess capacity of biological available copper to limit biologic activity makes it particularly useful in controlling some types of unwanted growth. For example, it was shown that some copper alloys have antitumoural,

anticancer activity. However, it was revealed that cytotoxic activity is related to the amount of bivalent copper content in the compounds tested. Also, copper has been recognized as an algacides to treat parasites.

Although, copper is a useful metal in small quantities, its presence in excess may have unintended harmful effects under certain conditions. As a result, copper is commonly regarded as a risk environment. Pronounced toxic effects of alloys containing these metals were confirmed when they were implanted subcutaneously or intramuscularly. The analysis of actual data indicates that these material lead to changes in tissues such as necrosis and inflammations.

Copper may have role of chemical modifier, inducing greater carcinogenic activity for nickel, from which it has normally.

Chronic copper poisoning is still a controversial problem, often associated with muscular pains, hypertension, neuro-psychological phenomena, hair loss etc. However, the World Health Organization considers copper a non-toxic metal.

5. Conclusions

Shape memory alloys based on copper can be used as biocompatible materials with human body only when corrosion tests allow this.

In addition, the manufacture of parts made of shape memory alloys must take into account the fatigue phenomena that can occur, embodied in the degradation of shape memory effect.

Received: May 14, 2010

“Gheorghe Asachi” Technical University of Iași
Department of Materials Science
e-mail: dragos_adc@yahoo.com

REFERENCES

1. Stanciu S., *Materiale cu memoria formei – metode de investigație și aplicații în tehnică*. Edit. Universitas, **XXI**, 2009.
2. Ungureanu G., Mareci D., Aelenei D., Nemțoi Gh., Mirza-Roșca J., *The Gaudent – a Biocompatible Material?*. Al V-lea Simpozion National de Biomateriale – Biomateriale și Aplicații Medico-Chirurgicale, Iași, 28 – 29 octombrie 2005.
3. Mareci D., Ungureanu G., Aelenei D., Mârza-Roșca J., *Electrochemical Behaviour of Some Copper-Based Dental Materials in Artificial Saliva*. Central Europ. J. (2006).
4. Bulancea V., *Materiale metalice avansate utilizate in medicina – curs*.

APLICAȚII BIOMEDICALE ALE ALIAJELOR CU MEMORIA FORMEI

(Rezumat)

Aliajele cu memoria formei se regăsesc în diverse aplicații biomedicale. Lucrarea prezintă o sinteză documentară a acestor aplicații și aspecte chimico-metalurgice legate de biocompatibilitatea acestor aliaje.

BULETINUL INSTITUTULUI POLITEHNIC DIN IAȘI
Publicat de
Universitatea Tehnică „Gheorghe Asachi” din Iași
Tomul LVI (LX), Fasc. 3, 2010
Secția
ȘTIINȚA ȘI INGINERIA MATERIALELOR

ELECTRICAL PROPERTIES OF ZrO_x THIN FILMS PREPARED BY REACTIVE MAGNETRON SPUTTERING

BY

APREUTESEI MIHAI, ARVINTE IONELA ROXANA
and CONSTANTIN DIDA

Abstract. In this article we present the investigation of the electrical properties of the ZrO_x thin films deposited at 200°C by the reactive magnetron sputtering method with the variation of O_2 reactive gas flow and deposition time. In terms of composition it can be observed two concentration regions, the first zone rich in Zr (max. 8 sccm for O_2 flow), where the deposition rate was high, and second zone, rich in O_2 (for O_2 flow between 8 and 16 sccm), where the deposition rate decreased considerably. Films from zone I revealed relatively low values of resistivity, ranging from $\sim 90 \mu\Omega \cdot \text{cm}$ to values around $200 \mu\Omega \cdot \text{cm}$ which allows indexing these films as of a “roughly” metallic-type. In zone II films show low conductivity and the resistivity can not be measure because of the oxygen high content from this region.

Key words: thin films, ZrO_x , electrical properties, reactive sputtering.

1. Introduction

The fourth-group transition metal, MeN (Me = Ti, Zr, Cr, V, etc.), have been of extensive commercial interest for many years due to their optical and mechanical properties. The unique combination of metallic and covalent bonding characteristics lead to properties such as high melting point, hardness, wear resistance, brittleness as well as good thermal and chemical stability and corrosion resistance. Metallic properties such as electrical conductivity and metallic reflectance, together with the aesthetic property of their prominent colorations in the visible wavelength region make their applications as coatings for decorative objects advantageous [1],..., [3].

Reactive magnetron sputtering is one of the most used techniques which can be used for deposition of any work piece, and is currently used for a wide

variety of thin films, from any solid metal or alloy to a variety of compounds. The term “sputtering” comes from the Dutch word “sputteren” and is mean “to spit out in small particles and with a characteristic explosive sound”. Groves was the first how discovered the sputtering phenomena in 1852, but Plucker, in 1858 suggest that this discovery can be used as tool to achieve metallic films. At the beginning Groves named the phenomena “cathodic disintegration”, but in 1921, Sir John Thompson renamed into “spluttering”, and after two years Thompson dropped the “l” and term become “sputtering” which is used nowadays [4]. Sputtering is a physical vapour deposition (PVD) process where the material is removed form a target because of the energetic ion bombardment, and is driven by momentum transfer between the ions and atoms in the material, presented in Fig. 1. Collisions are elastic or inelastic, depending on whether the internal energy of the colliding specie is preserved. In an elastic collision, only kinetic energy is interchanged and there is conservation of the momentum and kinetic energy of translational motion, and no atomic excitation occurs and potential energy is conserved [4],..., [8].

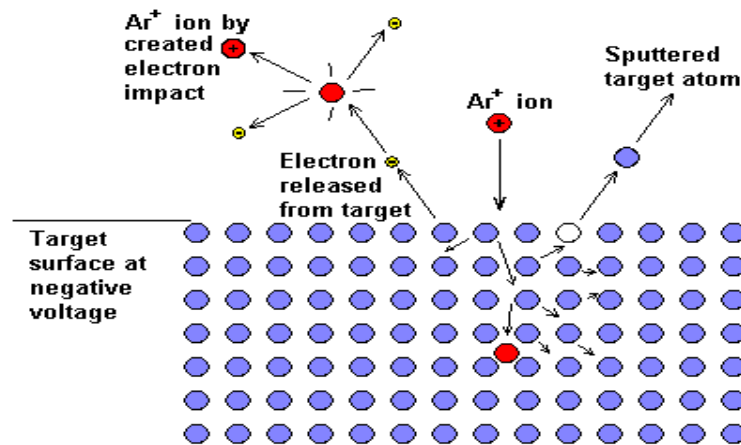


Fig. 1 – Scheme of the sputtering of the target atoms.

Magnetron sputtering dominates industrial production of metals and alloys because it is fast, inexpensive and easily scaled up in size. Large deposition areas and low substrate heating are added benefits. The films are generally polycrystalline or amorphous. Metal deposition is used to make electrical contacts on a variety of semiconductor substrates and for interconnects. Metallization of plastic parts is utilized by the automotive industry extensively. Reflective, darkened and decorative coatings on glass also employ sputtering of metals. Metal films are deposited on plastic bags that contain food to preserve freshness. Optical coatings, decorative coatings on costume jewelry are among some of the other areas where sputtering of metals

is used. The purity of the film is limited by the purity of the gas used to initiate sputtering. In sputtering the metal target remains close to the room temperature because of cooling, so that it is not a source for impurity gas [9].

2. Experimental Procedure

The ZrO_x samples were deposited by d.c. reactive magnetron sputtering in homemade system from high purity Zr (99.6 at. %) target onto polished stainless steel (AISI 316) ~ 0.5 mm thick for residual stresses analysis, standard silica (100) for composition analysis and glass substrates (~ 1.2 mm) used for optical characterization. Films were prepared in static mode (substrates to be coated were fixed in front of the target), using a gas atmosphere composed of argon and oxygen with a base pressure in the deposition chamber $\sim 5 \times 10^{-3}$ mbar using constant values of temperature (200°C).

In Fig. 2 in presented a schematic representation of the home-made deposition system with the pre-chamber, chamber, turbo molecular pumps, gate valve and rotatory pumps.

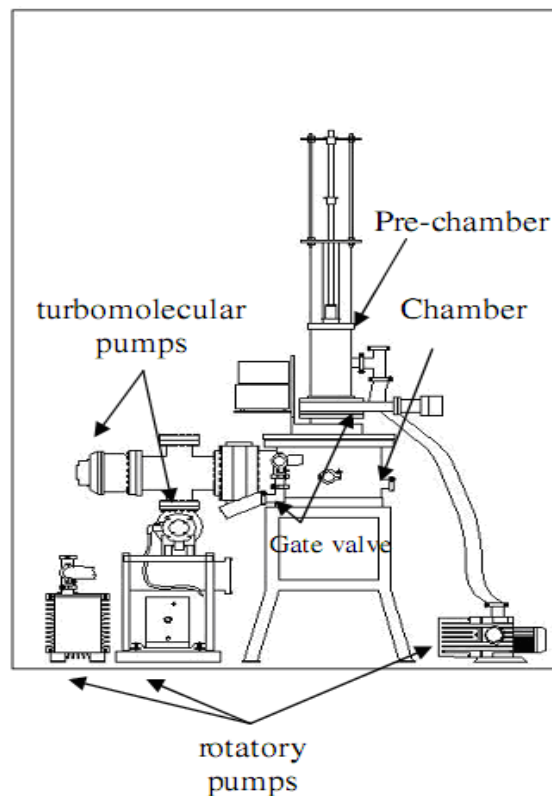


Fig. 2 – Schematic representation of the home-made deposition system.

Reactive gas flows varied from 1 to 15 sccm, with a total pressure around 5×10^{-3} mbar and deposition times between 3000 and 3600s. The experimental parameters are presented in Table 1.

The substrates were heated at $T_s=200^\circ\text{C}$ using d.c. bias grounded. Argon flow was kept constant at 60 sccm. The substrate rotation used was 7 rpm with the substrate holder positioned at 65 mm in all runs. Evolution of temperature was monitored with a thermocouple placed close to the surface of the substrate holder.

Table 1
Experimental Parameters Used for ZrO_x Films

Parameter	Probe	ZO1	ZO2	ZO3	ZO4	ZO5	ZO6	ZO7	ZO8	ZO9	ZO10
O ₂ flow(sccm)		1	1.5	2	2.5	3	4	5	6	9	15
Deposition time(s)		3000	3000	3000	3000	3000	3600	3600	3600	3600	3600
Substrate bias(V)		Grounded									
Argon flow(sccm)		60									
Total pressure(mbar)		$\sim 5 \times 10^{-3}$									
Current(A)		2									
Substrate rotation(rpm)		7									

2.1. The Characterization Technique Used for Electrical Proprieties. Four Point Probe Technique

The electrical resistivity of a material is a number describing how much that material resists the flow of electricity. Resistivity is measured in units of ohm-meters ($\Omega \text{ m}$). If electricity can flow easily through a material, that material has low resistivity. If electricity has great difficulty flowing through a material, that material has high resistivity. The electrical wires in overhead power lines and buildings are made of copper or aluminum. This is because copper and aluminum are materials with very low resistivities (about $20 \text{ n}\Omega \text{ m}$), allowing electrical power to flow very easily. If these wires were made of high resistivity material like some types of plastic (which can have resistivities about $1 \text{ E}\Omega \text{ m}$ ($1 \times 10^{18} \Omega \text{ m}$)), very little electric power would flow [10], [11].

The four-point collinear probe technique of resistivity measurement involves bringing four, equally spaced, electrical conducting pins in contact with the material of unknown resistance [12], [13]. The array is placed in the center of the material. A diagram of this technique is shown in Fig. 3.

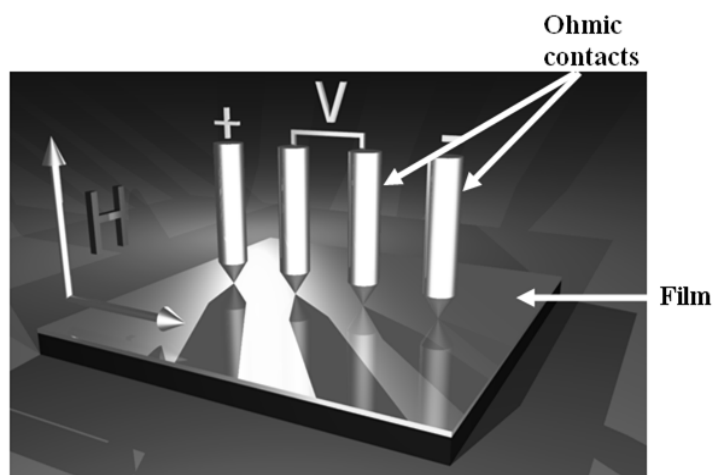


Fig. 3 – The four-point probe method for measuring resistivity.

A known current is passed through the two outside pins and the voltage is sensed at the two inside pins [14]. The resistivity is then calculated from the following equation:

$$(1) \quad \rho = \frac{\pi}{\ln 2} \times \frac{V}{I} \times t \times k ,$$

V – the measured voltage in volts

I – the source current in amps

t – the wafer thickness in centimeters

k – a correction factor based on the ratio of the probe to wafer diameter, and on the ratio of wafer thickness to probe separation

2.2. Results

For this work it was used the four point technique in order to measure the resistivity of the ZrO_x thin films. The reactive gas flow and the thickness of the produced coatings are presented in Table 3. In Fig. 4 is represented the deposition rate of produced ZrO_x films as function of the reactive gas flow. From Fig. 1 it can be observed that the evolution of the deposition rate is a function of reactive gas flow can be divided in two different regimes.

In first regime, corresponding to the samples deposited with the reactive gas flow below 8 sccm, the deposition rate has a stabilization where the obtain values are roughly 6×10^{-2} nm/s.

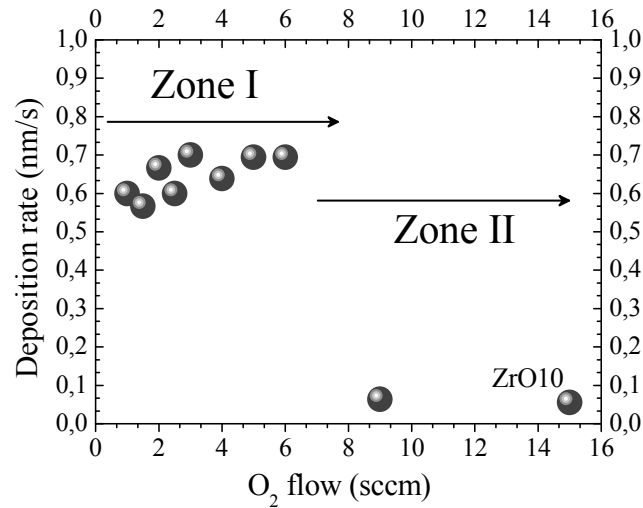


Fig. 4 – Deposition rate of the produced ZrO_x coatings as function of the gas flow rate.

In second regime there is a decrease of the deposition rate with the increase of the reactive gas flow from $\sim 6.9 \times 10^{-2}$ nm/s to the lowest value of the deposition rate ($\sim 0.5 \times 10^{-2}$ nm/s) corresponding to the ZrO10 sample with 200 nm thickness presented in Table 2.

Table 2
Reactive Gas Flow Rate During Depositions and Thickness of ZrO_x Films

Sample	Gas flow (sccm)	Thickness (nm)
ZrO1	1	1800
ZrO2	1.5	1700
ZrO3	2	2000
ZrO4	2.5	1800
ZrO5	3	2100
ZrO6	4	2300
ZrO7	5	2500
ZrO8	6	2500
ZrO9	9	230
ZrO10	15	200

The ZrO_x coatings have a wide range of different behaviors, as it can be observed by the evolution of the electrical resistivity at room

temperature, as a function of the reactive gas flow, presented in Fig. 5. From the plot, the first conclusion to be drawn is that the evolution of the electrical resistivity evidences the existence of two different zones.

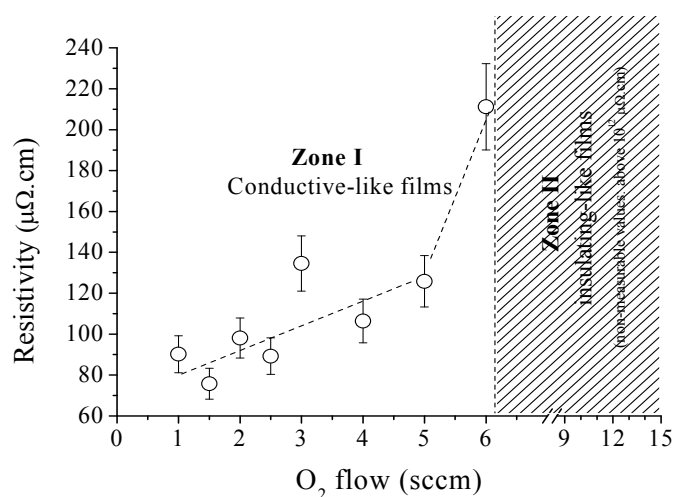


Fig. 5 – Electrical resistivity variations at room temperature as a function of the oxygen flow.

As you can see in the plot in zone I the amount of oxygen flow is varying from 0 to 6 sccm and is significant that the films are in the conductive phases.

In this phase the samples have a low resistivity because the electricity can flow easily through the material. In the same time the samples have a high value of conductivity which is increasing with the increase of the oxygen flow. For instance, at 1 sccm the resistivity value is around $\sim 90 \Omega\mu\text{.cm}$ and it is get to 6 sccm where the resistivity value is around $\sim 200 \Omega\mu\text{.cm}$. At the end of zone I where the oxygen flow is 6 sccm starts the transition zone and also the films are in a insulating phases. In zone II, the samples show high values of the electrical resistivity and the conductivity is thermally activated. Also, is significant the tendency to have highly insulating phases. Therefore, the films tend to be of insulating type. In this zone the resistivity is high and the electricity can not pass through the material easy.

For these samples with higher resistivity it is impossible to measure the electrical resistivity because the electricity instead of passing through the coating will pass through the substrate. Therefore, it is very difficult to measure the resistivity of the films because of the low conductivity; which means that above $10^{12} \Omega\mu\text{.cm}$ the resistivity can not be measure because the films have a high content of oxygen.

3. Conclusion

Electrical properties of thin films have practical importance and theoretical interest. The solid-state revolution has created important new roles for thin film electrical conductors, insulators, and devices.

The experimental data presented above offers an image of the reactive sputter deposition of zirconium oxide. The electrical properties of ZrO₂ films deposited by the reactive magnetron sputtering technique have been investigated at varying O₂ flow rates. The O₂ flow rate is found to be an important parameter in controlling the film composition, and properties.

The zirconium oxide films electrical behavior present straight correlation between the crystalline and electronic structure. The initial low values of resistivity were found to be related with the roughly metallic nature of the films. For the higher reactive gas flows (zone II) the resistivity of the films are increased, which can be explained by the decrease of the metallic bond contribution. Regarding the last zone, the coatings present high electrical resistivity and the conductivity is thermally activated.

One of most important fact is that during the experimental work all 10 coatings presented different evolution, but the two regimes (zone I and zone II) remain clearly definite even that we use different characterization technique.

Received: May 14, 2010

University "Transilvania" Braşov,
Department of Technological Equipment and Materials Science
e-mails: roxy_18_lo!@yahoo.com, dida.constantin@yahoo.com
m.apreutesei@gmail.com

REFERENCES

1. Harsha K.S.Sree, *Principles of Vapor Deposition of Thin Films*. First Edition, Ed. Elsevier, 2006.
2. Jimenez H., Restrepo E., Devia A., *Surface Coatings Technology*. 201-1594 (2006).
3. Chou W.J., Sun C.H., Yu G.P., J. H. H., *Mat. Chem. Phys.*, 82, 228 (2003).
4. Rizzo A., Sigore M.A., Mirengi L., Dimaio D., *Thin Solid Films*. 515, 1486 (2006).
5. Liu C.P., Yang H.G., *Thin Solid Films*. 444, 111 (2003).
6. Ivanovskii A.I., Medvedeva N.I., Okatov S.V., *Inorganic Materials*. 37, 459 (2001).
7. Benia H.M., Guemmaz M., Scmerber G., Mosser A., J. C. Parlebas, *Appl. Surf. Sci.* 200- 231 (2002).
8. Pilloud D., Dehlinger A.S., Pierson J.F., Roman A., Pichon L., *Surface Coatings Technology*. 174 – 175, 338-344 (2003).
9. Kumar A., Chung Y.W., Moore J.J., Smugeresky J.E., *Surface Engineering, Science and Technology I*. The Minerals, Metals & Materials Society, Warrendale (1999).

10. Lamni R., Martinez E., Springer S.G., Sanjinés R., Schmid P.E., Lévy F., *Thin Solid Films*, 447-448, 316-321 (2004).
11. Sanz J.M., Soriano L., Prieto P., Tyuliev G., Morant C., Elizalde E., *Thin Solid Films*, 332, 209-214 (1998).
12. Meng L.J., Dos Santos M.P., *Thin Solid Films* (1994).
13. Bhuvaneswari H.B., Nithiya Priya I., Chandramani R., Rajagopal Reddy V., Mohan Rao G., *Cryst. Res. Technol.*, **38**, 12, 1047-1051 (2003).
14. Prieto P., Galán L., Sanz J.M., *Phys. Rev.*, **B 47**, 1613 (1993).

PROPRIETĂȚILE ELECTRICE ALE STRATURILOR SUBȚIRI DE TIP ZrO_x
OBȚINUTE PRIN PULVERIZARE REACTIVĂ ÎN SISTEM
MAGNETRON

(Rezumat)

În acest articol am prezentat o investigație a proprietăților electrice ale straturilor subțiri de tipul ZrO_x depuse la temperatura de 200°C prin metoda pulverizării reactive în sistem magnetron cu variația debitului gazului reactiv (O_2) și a timpului de depunere. În ceea ce privește compoziția se pot observa două regiuni de concentrare, prima regiune bogată în Zr (max. 8 sccm pentru debitul de O_2), zonă în care rata de depunere este ridicată și cea de a doua regiune bogată în O_2 (pentru debit de O_2 între 8 și 16 sccm), unde rata de depunere a scăzut considerabil. Filmele din zona I prezintă valori relativ scăzute ale rezistivității, variind de la $\sim 90 \mu\Omega\cdot\text{cm}$ până la valori în jur de $200 \mu\Omega\cdot\text{cm}$ care permite indexarea acestor straturi ca fiind de tipul metalic. În zona II filmele prezintă o conductibilitate scăzută și rezistivitatea nu poate fi măsurată datorită conținutului ridicat de oxigen din această regiune.

EXPERIMENTAL RESEARCH ON THE MEASURING METHODS OF METALLIC SURFACES

BY

MARIUS BENȚA, MARIN CLAUDIU GARGAZ, ANCA IFTODE
and ȘTEFAN HULUȚA

Abstract. This paper contains the investigation of metallic surfaces using AFM technology. This method provides the possibility to map out surface topography with atomic resolution in all three dimensions. The data are digitally stored, allowing the computer to manipulate and display the data as a three-dimensional rendition, viewed from any altitude and azimuth as shown in Fig.1. For topographic analysis and profilometry, the resolution and three-dimensional nature of the data is unequalled by other techniques. The ease of use and nondestructive nature of the imaging are notable.

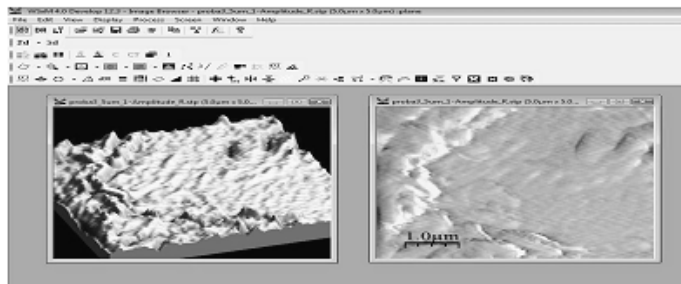


Fig. 1 – AFM image of the investigated metallic surface.

Key words: nanometers, AFM, metallic.

1. Introduction

Thermally sprayed coatings are now used extensively in a variety of applications. However, their application has often preceded detailed knowledge or understanding of their corrosion mechanisms or rates.

Previous studies involving plasma sprayed coatings [5] have shown that good quality coatings, in terms of low porosity, are essential to protect the substrate from corrosion.

There are many thermal spray processes available to date: the high velocity oxygen fuel (HVOF) process, which uses higher exhaust velocities and lower flame temperatures than other processes, can produce coatings of low porosity levels (1%) and avoids alteration of the mechanical properties of the substrate [7]. The corrosion characteristics of thermal sprayed coatings in static saline environments are extremely important where the flow of aqueous solution over components intermittently ceases.

It has been established [1], [2] that where coatings are applied by a high-quality process and under stringent quality control procedures, the coatings can provide a very effective barrier to the substrate and prevent any corrosion from occurring.

In this situation, however, it is very important to appreciate that corrosion of the coating can occur and that initiation and propagation of corrosion, associated with microstructural features of the composite system, are a real issue. For improvements to the coating corrosion resistance to be made, a full understanding of the corrosion rates and mechanisms, and in particular the resistance of the metallic binder (in cermets systems), is required. In addition, an understanding of static corrosion behavior can help reveal the mechanisms of the coating degradation in erosion-corrosion environments [9], [10].

This article investigates the corrosion rates and mechanisms of two HVOF coatings (WC-Co-Cr and WC-Co).

2. Experimental Procedure

Two HVOF sprayed coatings are studied in this work: a WCCo-Cr coating with nominal composition 86%WC 10%Co-4% Cr, and a WC-Co coating with a nominal composition 86% WC-14% Co. The coatings were applied to a stainless steel substrate (UNS S31603). Specimens were soldered on the rear side to an electrical conducting wire and subsequently encapsulated in nonconducting resin.

The exposed coated face of the specimen was then ground with silicon carbide abrasive papers and polished to a 6 μm diamond finish. The main seawater constituents were 19...300 ppm chloride, 11 000 ppm sodium, 2700 ppm sulfate, 1300 magnesium, 400 ppm calcium, 400 ppm potassium, and 150 ppm bicarbonate ions. The specimen-resin interfaces were sealed using Lacomit varnish (Agar Aids, UK) to prevent interference from the substrate.

Electrochemical monitoring was carried out with a standard three-electrode cell, comprising a platinum auxiliary electrode and a saturated calomel reference electrode (SCE). Direct current (DC) anodic polarization tests were carried out after 1 h immersion in the seawater at 18 and 50°C.

The seawater was left open to the atmosphere. The potentiostat was used to scan the electrode potential of the coating samples from the free corrosion potential (E_{corr}) in the positive (anodic) direction until a current in the range of 500-700 $\mu\text{A}/\text{cm}^2$. In addition, an atomic force microscope (AFM) was used to map the topography of the coatings during accelerated corrosion tests. The AFM was configured to probe the surface under water and to record images during anodic polarization tests. Each image took 6 min to produce, during which time the potential had shifted by approximately 90 mV.

3. Results

During the decrease in current (points B to C), the matrix is dissolving at a steady rate, defining the hard phase particles more clearly (Fig. 2 *c*). As the current increases (points C to D in Fig. 2 *d*), the matrix dissolves further, revealing the smaller hard phases from point D to E (Fig. 2 *e*).

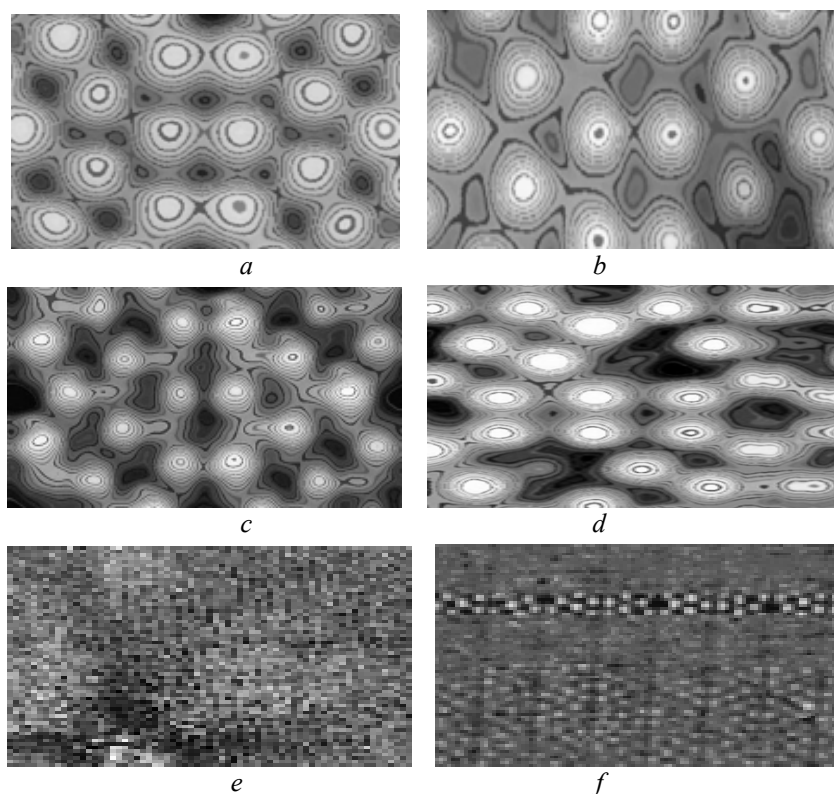


Fig. 2 – In situ AFM images: *a* – Polished coating prior to polarization; *b* – points A to B; *c* – points B to C; *d* – points C to D; *e* – points D to E; *f* – end of anodic polarization.

At the end of the anodic polarization, areas where the matrix has dissolved in some regions and areas of attack around the matrix-hard phase interface can be seen (Fig. 2 *f*).

In a similar manner, the corrosion mechanisms during anodic polarization of the WC-Co-Cr coating were examined. Fig. 3 *a*) shows the coating at the free corrosion potential with the light grey hard phases encased in the darker grey matrix.

The rapid increase in current with the potential corresponds to dramatic matrix dissolution and leaves the hard phase protruding from the matrix (Fig. 3 *c*). As the current stabilizes at point D, carbides begin to fall out from the matrix and leave voids behind (Fig. 3 *d*).

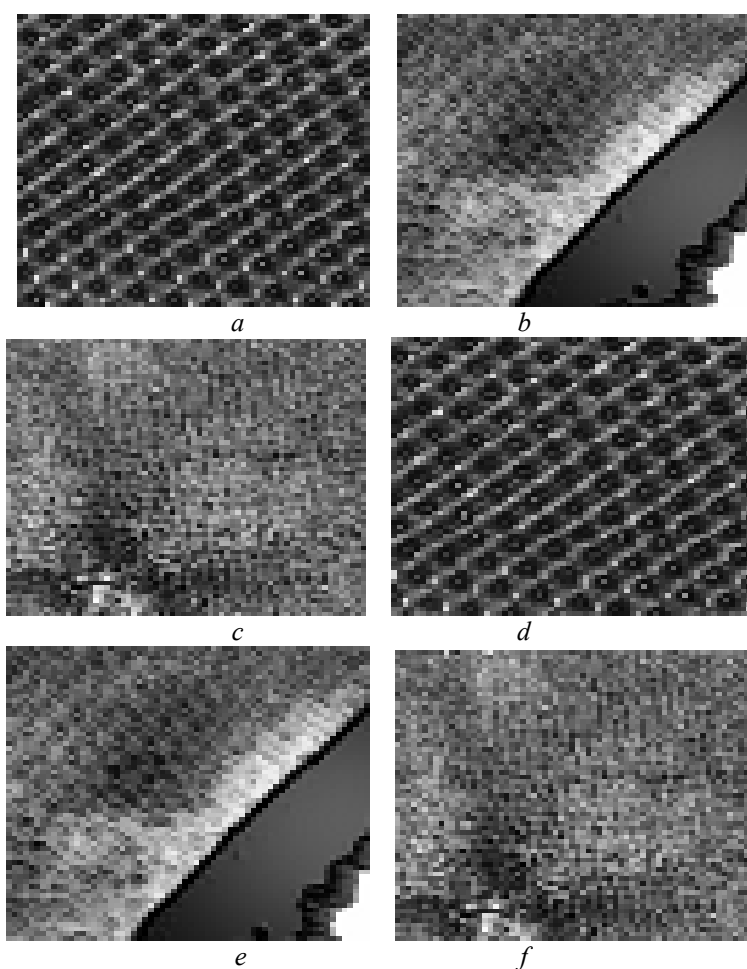


Fig. 3 – In situ AFM images: *a* – Polished coating prior to polarization; *b* – point B; *c* – point C; *d* – point D; *e* – end of anodic polarization.

This progresses until the end of the scan at point E, where the matrix consists mainly of voids left by the carbide particles and a few carbides on the next layer are visible (Fig. 3 e). After immersion in seawater for 1 h at 50°C, the kinetics of the anodic polarization processes are accentuated on both coatings.

3. Conclusion

1. The use of an AFM can aid the determination of corrosion mechanisms on a microscale.

2. The addition of chromium to a cobalt matrix increases the corrosion resistance of a WC-based HVOF sprayed cermet coating and its extent of this has been quantified.

3. Although the WC-Co-Cr coating undergoes more localized attack at 18°C, accentuated at the hard phase-matrix interface, the WC-Co has more uniform corrosion affecting the entire matrix.

4. An increase in temperature results in extensive dissolution of the cobalt matrix, whereas on the CoCr matrix more severe attack is further localized in regions not associated with any specific microstructural features.

Received: May 14, 2010

Transilvania University of Brașov,
Department of Science and Materials
e-mail: mariusbenta@yahoo.com

REFERENCES

1. Tsai S.T., Shih H.C., *The Use of Thermal-Spray Coatings for Preventing Wet H₂S Cracking in HSLA Steel Plates*. Corros. Prev. Control, 44, 42-48 (1997).
2. Duncan R.J., Thompson C.B., *A Guide to Weld and Thermal Spray Hardfacing in the Pulp and Paper Industry*. Part 2: Applications, Mater. Des., 11, 71-75 (1991).
3. Thompson C.B., Garner A., *Identification and Control of Wear in the Pulp and Paper Industry*. Pulp Paper Can, 53-56 (1986).
4. Pejryd L., Wigren J., Greving D.J., Shadley J.R., Rybicki E.F., *Residual Stresses as a Factor in the Selection of Tungsten Carbide Coatings for a Jet Engine Application*. J. Therm. Spray Technol., 4, 268-274, (1995).
5. Ashary A.A., Tucker R.C., *Electrochemical Corrosion Studies of Alloys Plasma Sprayed With Cr₂O₃*. Surf. Coat. Technol., 39/40, 701-709 (1989).
6. Ashary A.A., Tucker R.C., *Electrochemical and Longterm Corrosion Studies of Several Alloys in Bare Condition and Plasma Sprayed with Cr₂O₃*. Surf. Coat. Technol., 43/44, 567-576 (1990).
7. Pawlowski L., *The Science and Engineering of Thermal Spray Coatings*. John Wiley and Sons, New York, 1994.
8. Perry J.M., Neville A., Wilson V., Hodgkiess T., *Assessment of the Corrosion Rates and Mechanisms of a WC-Co-Cr HVOF Coating in Static and Liquid - Solid Impingement Saline Environment*. Surf. Coat. Technol., 137, 143 (2001).

9. Neville A., Hodgkiess T., *Corrosion Behavior and Microstructure of Two Thermal Spray Cermet Coatings*. Surf. Eng., 12, 303-312 (1996).
10. Guilemany J.M., Fernandez J., De Paco J.M., Sanchez J. *Corrosion Resistance of HVOF WC-Co and TiC/Ni-Ti Coatings Sprayed on Commercial Steel*. Surf. Eng., 1998, 14, 133-135; Coatings, Mater. Sci. Forum, 280-292, 641-654 (1998).

CERCETAREA EXPERIMENTALĂ A METODELOR DE MĂSURARE A SUPRAFETELOR METALICE

(Rezumat)

Acest document conține investigarea suprafețelor metalice folosind tehnologia AFM. Această metodă oferă posibilitatea de a reda topografia de suprafață, cu rezoluție atomică în toate cele trei dimensiuni. Datele sunt stocate digital permițând computerului să manipuleze și să afișeze datele ca o vedere tridimensională, privită de la orice configurație, așa cum se arată în figura 1. Pentru analiza topografică și profilometrie, rezoluția și natura tridimensională a datelor sunt de neegalat în alte tehnici. Ușurința de utilizare și natura nedestructivă a imaginilor sunt notabile.

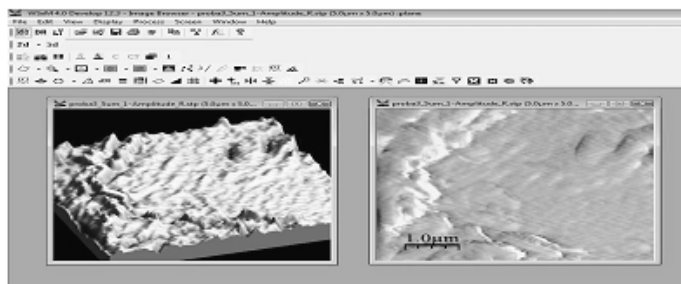


Fig. 1 – Imagine AFM pentru investigarea materialelor metalice.

COMPARATIVE STUDY ON OBTAINING POROUS AGENTS FROM NaCl POWDERS

BY

EMIL BRUJ, DOREL NEMEȘ and VALENTIN MOLDOVAN

Abstract. Coarse NaCl powder is used to manufacture leachable preforms as prerequisites for obtaining metallic foams. This method is less time consuming because leachable preforms can be obtained in approximately 45 minutes, compared to 2-100 hours by sintering. Samples obtained by these methods were characterized by optical and electron microscopy.

Key words: NaCl powder, sintering, preforms, water vapor bonding.

1. Introduction

Powdered sodium chloride were used for a long time as a model system for the investigation of ceramic sintering behavior; however, the system is also interesting from a practical point of view, because NaCl sintered preforms are used in the manufacture of highly porous microcellular metals or ceramics by the replication process [1].

NaCl preforms are used as porous agents for obtaining metal foams by infiltration [2].

Previous work on NaCl sintering, provide some observations of powders of different particle size exposed to a variety of sintering temperatures [3],..., [7].

The present paper propose an alternative method of sintering the NaCl particles in a much shorter time, all at once with the same properties with those obtained by conventional sintering methods. Also, high temperatures are not necessary. The only heat source is used to heat water.

This method is less time consuming because leachable preforms can be obtained in approximately 45 minutes, compared to 2-100 hours by sintering.

2. Materials and Experimental Procedures

Irregularly shaped NaCl powder was used, with grain sizes of 315 μm , 500 μm , 630 μm , 800 μm and 1.25 mm. NaCl preforms were obtained by two methods: sintering in air at temperatures between 700-780°C and sintering the salt particles in water vapor. For each size fraction sintering times were 2, 4, 8, 16, 32 and 72 hours.

When sintering the NaCl particles in water vapor, interparticle links similar to those obtained by conventional sintering are formed due to condensation and dissolution. Thus, a solid matrix of salt is obtained, which after leaching will become the intercommunicating porous structure of the metallic foam.

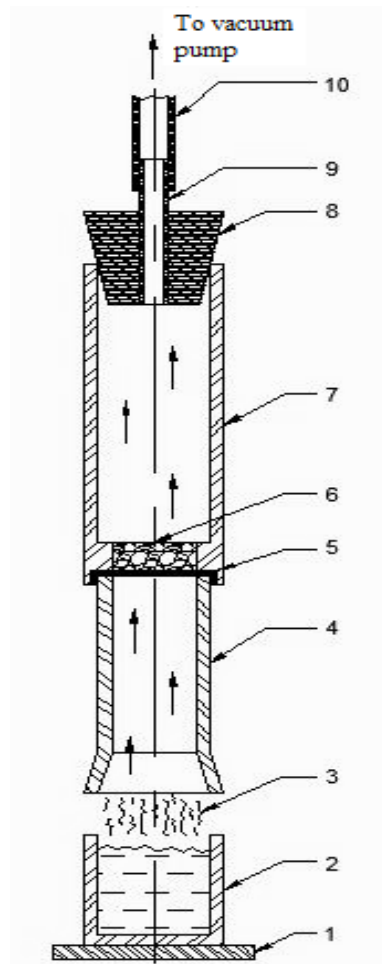


Fig. 1 – Schematic diagram of the NaCl particle sintering in water vapor.

Schematic diagram of the method of sintering the NaCl particles in the water vapor is shown in Fig. 1. A bowl of water 2 is placed on a heat source 1, and when reaching the input temperature begins to vaporize. The vapors 3 are collected and directed through the collection tube 4. Between the collection and directing tube 4 and directing tube 7, a sieve 5 is placed and on top of the sieve the NaCl particles 6 are freely poured. Targeting end of the tube 7 is closed with a rubber cork 8 troughs which is placed a tube of smaller section 9 which connects the vacuum pump through the hose 10. In the water vapor sintering experiment, the exposure was 5, 10, 15 and 30 minutes.

Samples obtained by the two methods were characterized by means of optical and electronic microscopy and compared. The obtained preforms were then infiltrated with a PbSn alloy, the salt was then dissolved and the final porous structure was characterized using optical microscopy.

3. Results and Discussions

NaCl particles were freely poured in the die and sintered in air at a temperature of 700°C, 720°C, 740°C, 760°C and 780°C. After studying the samples, was found that the best regime of sintering temperature is at 760°C. From the obtained results one could draw a curve of particles size as a function of the sintering time. It was found that on the larger particles, the sintering time is longer. For the particle size of 315 μm the sintering time is 2 hours and for the particle size over 1 mm the sintering time exceeds 70 hours (Fig. 2).

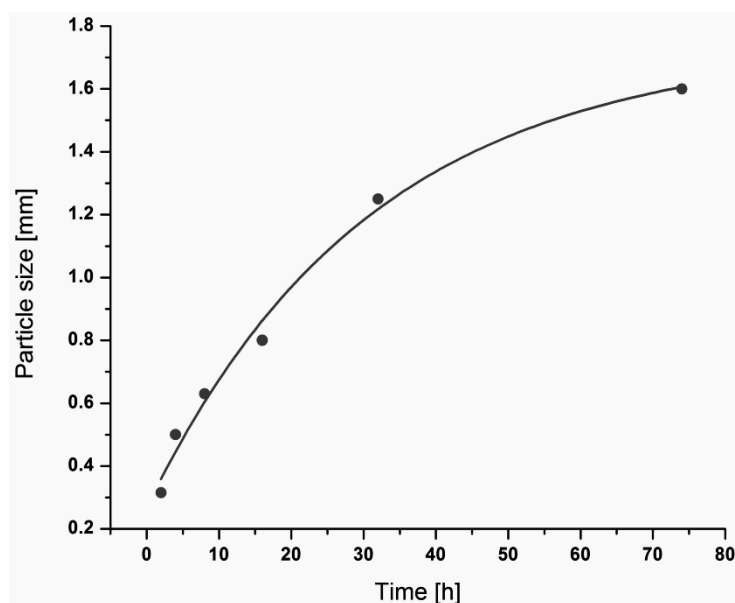


Fig. 2 – Particles size as a function of the sintering time.

One can see in Fig. 3, that for the particles of 1.2 to 1.6 mm size fraction the sintering time of 2 hours is too short for the formation of solid sintering necks (sufficient to give good mechanical strength).



Fig. 3 – Optical microscopy image obtained by sintering salt in air (particles of 1.2–1.6 mm).

By increasing the time, the sintering necks between the particles are growing, providing increased strength to the sample during the alloy infiltration. Depending on the desired porosity and strength of the final sample an optimum sintering time can be chosen. When choosing a short sintering time, the final sample will have a high density and strength, while a longer sintering time gives a much lower density and resistance.

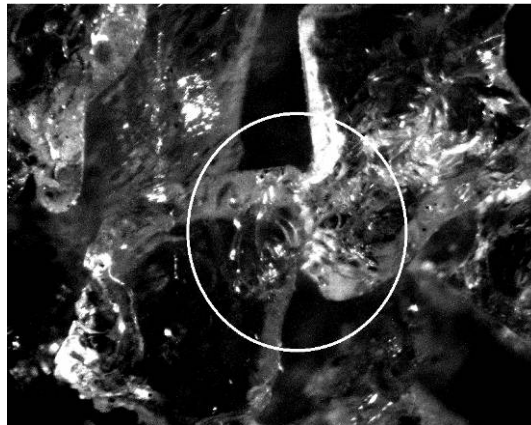


Fig. 4 – Optical microscopy image of salt obtained by sintering in air (1.2 to 1.6 mm particle size, for 72 hours).

On a longer sintering time as shown in Fig. 4, the sintering necks between the particles grow and become stronger, giving good resistance to the preform during the infiltration. If the particle sizes of NaCl are larger, the sintering time should be longer. A very short sintering time of NaCl larger particles cannot ensure a good resistance of precursor during the melt infiltration.

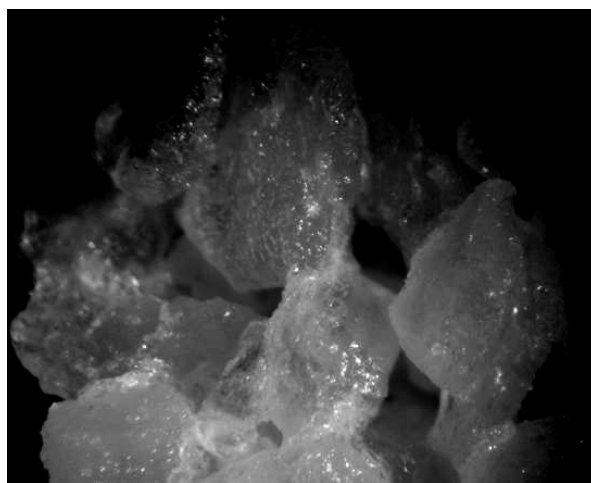


Fig. 5 – Optical microscopy image obtained by sintering salt in water vapor (1.2 to 1.6 mm particle sizes for 10 minutes).

Preforms with good resistance to infiltration were obtained in a much shorter time of about 10 minutes for the same particle sizes by sintering salt in water vapors (Fig. 5).

Optimal sintering time for particle sizes of 1.2 mm was at a temperature of 760°C with a maintaining time of 72 hours. By comparison, the optimal time of sintering the same particle sizes in water vapor is 10 minutes, achieving the same results.

A balance must be found between the amount of vapor generated and the vacuum created to circulate an optimum quantity of water vapors between the NaCl particles in the experimental setup. If the amount of steam is too high, dissolution of salt particles occurs too quickly, and condensation builds up in the sample destroying its structure. If the amount of vapor is too low sintering cannot occur. Therefore, an optimum amount of vapor need to pass through the setup. To better highlight the structure, samples were infiltrated with an PbSn alloy (Fig. 6).

After solidification of the alloy, the salt is dissolved, leaving a solid metal matrix with open porosity which represents the "negative" of the infiltrated preform.



Fig. 6 – Photo image with a PbSn sample obtained by infiltration of preforms and dissolution of NaCl.

To better highlight the obtained porous structure, the samples were embedded in resin, polished and studied with a metallographic microscope (Fig. 7).

As one can see, the open porosity of the preform was filled completely, and after cooling and dissolving the salt the final sample obtained was the „negative” of the preform.



Fig. 7 – Metallographic microscope image of a porous metal structure obtained by sintering the NaCl particles in water vapor for 10 minutes.

3. Conclusions

A balance must be found between the amount of vapor generated and the vacuum created to circulate an optimum quantity of vapors between the NaCl particles in the experimental setup.

Metal foams were obtained by two different methods using preforms of salt, achieving the same result.

This method is less time consuming because leachable preforms can be obtained in approximately 45 minutes, compared to 2-100 hours by classic sintering.

A c k n o w l e d g e m e n t s. The authors would like to thanks the UEFISCSU for financial support in "Program IDEI", Project no: 749/19.01.2009

Received: May 14, 2010

Technical University of Cluj-Napoca
Department of Materials Science and Technology
e-mail: Emil.BRUJ@stm.utcluj.ro

REFERENCES

1. Goodall R., Despois J.F., Mortensen A., *Sintering of NaCl Powder: Mechanism and First Stage Kinetics*. J. of the Europ. Ceramic Soc., 26, 3487-3497 (2006).
2. Abd-Elmouneim, Sid-Ali Kaoua, Mohammed Azzaz, Jean Dominique Bartout, Yves Bienvenu, *Elaboration and Characterization of Metallic Foams Based on Tin-Lead*. Materials Sci. a. Engng., A 494, 425-428 (2008).
3. Hakamada M., Yamada Y., Kuromura T., Asao Y., Chen Y., Kusuda H., Mabuchi M., *Porous Metals Produced by Spacer Method as Ecomaterials*. Adv. Materials Res., 15-17, 416-421 (2007).
4. Russell Goodall, Jean-Francois Despois, Ariane Marmottant, Luc Salvo, Andreas Mortensen, *The Effect of Preform Processing on Replicated Aluminum Foam Structure and Mechanical Properties*. Scripta Materialia, 54, 2069-2073 (2006).
5. Despois J.F., Marmottant A., Salvo L., Mortensen A., *Influence of the Infiltration Pressure on the Structure and Properties of Replicated Aluminum Foams*. Materials Sci. a. Engng., A 462, 68-75 (2007).
6. Jiang B., Zhao N.Q., Shi C.S., Du X.W., Li J.J., Man H.C., *A Novel Method for Making Open Cell Aluminum Foams by Powder Sintering Process*. Materials Let., 59, 3333-3336 (2005).
7. Sermin Ozan, Seda Bilhan, *Effect of Fabrication Parameters on the Pore Concentration of the Aluminum Metal Foam, Manufactured by Powder Metallurgy Process*. Int. J. Adv. Manuf. Technol., 39, 257-260 (2008).

STUDIUL COMPARATIV ASUPRA OBTINERII AGENȚILOR
POROȘI DIN PULBERI DE NaCl

(Rezumat)

Preforme din NaCl sunt folosite ca agenți porogeni la obținerea spumelor metalice. S-a folosit pulberea de NaCl cu granulația între 400 μm – 1,25 mm. Au fost obținute preforme de NaCl prin două metode: sinterizarea în aer la temperaturi cuprinse între 700-780°C și prin expunerea particulelor de sare în baie de vapori. La expunerea particulelor de NaCl în vapori de apă se formează legături interparticule datorită condensării și dizolvării, similare cu cele obținute prin sinterizare. Se obține astfel o matrice solidă de sare ce va reprezenta, după eliminare, în urma infiltrării materialului metalic, rețeaua poroasă de pori intercomunicați a spumei metalice. Metoda obținerii agenților porogeni în baie de vapori este mai economică deoarece se pot obține preforme în circa 45 de minute față de metoda sinterizării care durează 2-100 ore. Probele obținute prin cele două metode au fost caracterizate prin microscopie optică și electronică.

BULETINUL INSTITUTULUI POLITEHNIC DIN IAȘI

Publicat de

Universitatea Tehnică „Gheorghe Asachi” din Iași

Tomul LVI (LX), Fasc. 3, 2010

Secția

ȘTIINȚA ȘI INGINERIA MATERIALELOR

METAL FLOW AND SOLIDIFICATION OF BLADE TYPE COMPONENTS NUMERICAL SIMULATION RESULTS

BY

**DOREL BUTNACIUC, DAN-GELU GĂLUȘCĂ, MIHAI DUMITRU
and CIMPOEȘU NICANOR**

Abstract. A virtual casting and solidification analyze method is used for a magnesium based alloy investigation. As product was analyze the pouring of a magnesium based sample with much utilization like blades, pump components, small gears, water impellers and housings, marine fittings, flanges, low pressure valves and fittings, pipe fittings, plumbing fixtures, ornamental fixtures. Advantages of virtual casting and solidification analyze method are clearly connected to price and time process, an almost 90% correspondence between practical results and numerical result being helpful in any case.

Key words: metal flow, solidification, numerical simulation, prostheses.

1. Introduction

Computer simulation packages have been successful in predicting filling behavior in extremely complicated geometries, and most of the current numerical solutions are based on a hybrid finite-element/finite-difference scheme and the middle-plane model. This imported model causes some inconvenience during applications. This study introduces surface model as the datum plane, instead of the traditional middle-plane model and additional boundary conditions in the gap wise direction are employed to keep the flows in the surfaces at the same section coordinative. The simulation presented here is compared with the experimental results obtained with instrumented test mold and C-Mold results. It is demonstrated that the present formulation is well suited to handle cavities generated directly by mold design process with computer aided design (CAD) tools.

Numerical solutions allow researchers to observe and quantify what is not usually visible or measurable during real casting processes. The goal of such simulations is to help shorten the design process and optimize casting parameters to reduce scrap, use less energy and, of course, make better castings. Simulation produces a tremendous amount of data that characterize the transient flow behavior (*e.g.*, velocity, temperature), as well as the final quality of the casting (*e.g.*, porosity, grain structure).

Numerical simulation provides a powerful means of analyzing various physical phenomena occurring during casting processes. It gives an insight into the details of fluid flow, heat transfer and solidification.

The capability to produce investment casting components of high quality while at the same time reducing product costs and development times is the challenge the foundry industry faces today. Increasingly complicated parts are being made through the investment casting process with less castable alloys. It takes good understanding of the actual casting process, and experience in numerical simulation, for a designer to be able to relate one to the other and derive useful conclusions from the results. Computer aided modeling has been helping the foundry industry for the past several years, not only with the design of new components, but also in the redesign of existing products. By eliminating product defects and reducing scrap and rework, the investment caster can achieve improvements and more consistent product quality and obtain higher yields. Even though computer aided process simulation has been available for the past fifteen years, many investment casters still use the conventional trial and error approach for process development. In many foundries, new cast components are often put together in different departments working independently of each other. When a new customer's need is identified, the design group generates the part drawings [1].

In this paper with known input parameters a casting process is simulated based on a numerical model obtaining a blade part.

2. Experimental Details

Choosing a complex part like blade we analyze the material behavior at melting using a mathematical model evolve earlier [2].

In all researches concerning the melting process modeling, solidification and alloys contraction the simulation was realize on paralelipipedic bench marks type plate. Choosing this configuration is justified by problems complexity connected with modulation and established limit conditions [3].

As simulated melt material was used a B199 AZ92A alloy, commercial material with extended applications [4] characterizes by a chemical composition

presented in Table 1.

Table 1
Chemical Composition of Investigated Alloy

Material: B 199 AZ92A Standard: ASTM Country: USA			
General Composition Mechanical properties SmartCross			
Chemical Composition (%)			
Criteria	Min.	Max.	Approx
Si		0,3000	
Cu		0,2500	
Mn	0,1000	0,3500	
Zn	1,6000	2,4000	
Ni		0,0100	
Al	8,3000	9,7000	
Total Others		0,3000	

In alloy, a magnesium based alloy type C83600 elaboration the loading consist from

- proper waste materials;
- magnesium ingot of technical purity;
- zinc waste as span and wires;
- brass waste materials;
- Pb10 alloy waste products [5].

Paying respect for material properties, presented in Table 2, for pouring simulation the behavior of thermal expansion coefficient with temperature present more interest.

Table 2
Melt Material Properties

Property	Value	Unit
Density	1820	kg/...
Specific Heat	1050	J/kg*K
Thermal Cond...	Variable	W/...
Liquidus Temp...	593	
Solidus Tempe...	443	
Latent Heat	373000	J/kg
Dynamic Visco...	0.001456	kg/...
Coeff. of Ther...	2.6e-005	/K
Vol. Change o...	4.1	%
Critical Solid Fr...	0.3	
Surface Tension	0.55	N/m

All materials change their size when subjected to a temperature change as long as the pressure is held constant. In the special case of solid materials, the pressure does not appreciably affect the size of an object, and so for solids, it is usually not necessary to specify that the pressure be held constant. The coefficient of thermal expansion describes how the size of an object changes with a change in temperature. Specifically, it measures the fractional change in volume per degree change in temperature at a constant pressure.

The volumetric thermal expansion coefficient is the most basic thermal expansion coefficient. All substances expand or contract when their temperature changes, and the expansion or contraction always occurs in all directions. Substances that expand at the same rate in any direction are called isotropic. Unlike gases or liquids, solid materials tend to keep their shape. For solids, one might only be concerned with the change along a length, or over some area. Experimental results concerning the thermal coefficient behavior are presented in diagram from Fig. 1.

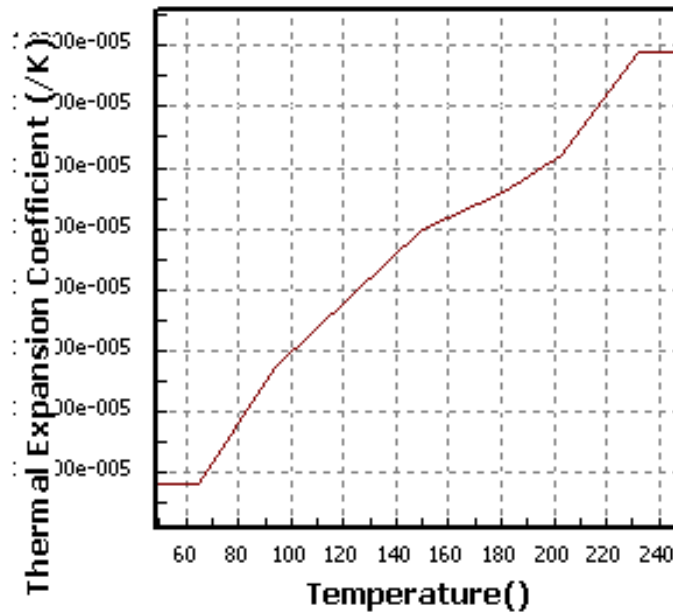


Fig. 1 – Thermal expansion coefficient variation with temperature.

Expansion coefficients are specially defined for these cases, and they are known as the linear and area expansion coefficients. However, they all come from the volume expansion coefficient, which explains how the substance expands in any direction.

3. Blend use for Forming

For preparation of the used forming blend was used a quart sand mono granular delivered by S.C. MINDO S.A. Dorohoi, Botosani with next characteristics

- Medium granulation M50 = 0,220 mm
- Uniformity degree G.U. = 72%.

At forming blend preparation was used a sodium silicate as binding element added in 6% proportion from sand mass. Sodium silicate was purchased from S.C. CHIMFOREX S.A. Pleasa, Prahova, having next characteristics:

- Relative density 1,54 kg/dm³
- Silicon dioxide 31,5%
- Full alkalinity, Na₂O 14 %

Strengthening of forms is realized by CO₂ insufflations in proportion of 60% from sodium silicate mass.

Preparing of forming mixture was realized in a swirl mixer with discontinuous functioning.

Choosing the forming mixture by sand bind with sodium silicate was made based on next advantages:

- was not necessary the form drying;
- stuffing special operations of forming mixture was not requested;
- was not necessary forming frames which allow the placement after desire of thermocouples for temperature measurement from form cavity and from form wall;
- high mechanical resistance of form fact that permit a good manipulation of them, without degradation risks;
- big dimensional precision.

Thermo-physic parameters of forming blend bind with sodium silicate are [5;7]

- density $\rho_{mixture} = 1550$ [kg/m³];
- caloric capacity $C_{pmixture} = 1170$ [J/kg grad];
- thermal conductivity $\lambda_{mixture} = 0,4$ [W/mK].

Elaboration process takes place in a casting furnace with heating by induction with 1000 Hz frequency and carborundum crucible.

After charge calculation in furnace was put the proper waste materials and brass waste alloys [5].

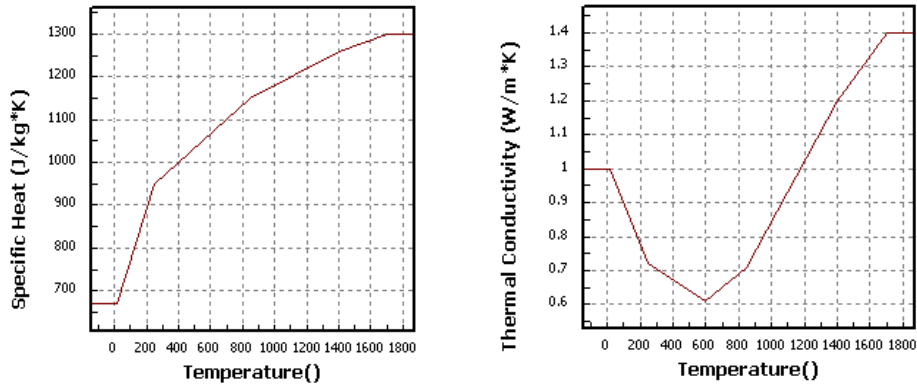


Fig. 2 – Sand properties as specific heat and thermal conductivity variation with temperature.

After heating, but before of liquid phase appearing, was added protection and de-oxidation fondant with content made by NaCl, KCl, NaF, Na_3AlF_6 in proportion of 1% from loading, made by S.C. BENTOFLEX S.A. Satu Mare, named flux I-2 [3]. In casting bath already form was add the calculated quantities of high purity zinc and ferrous-manganese. After taking a sample and fast chemical analysis effectuation using a spectrometer METALSCAN 2500, was made the adjusting ads of composition with clean waste alloy and technical zinc ingot. Simultaneous with this was used the fondants for degassing 0,5% chloride zinc [6].

Before pouring the bath must be extra heated at 750°C , extract the slag, take the final sample for chemical analyze and pouring the necessary alloy for a sample in a hand caldron sheathed with refractor material. Approximate time of pouring was around 5 seconds.

After form heating at 50°C the burner is put away the intermediary semi-form is elevated and after the removal of sustain supports is set on inferior semi-form. All experimental details were insert in numerical model and take in calculus.

4. Experimental Results

As all computational programs, which conduit simulations, a series of parameters must be set at the experiment begging like material properties (density, specific heat, thermal conductivity, liquidus temperature or solidus temperature) fact realize in the previous step. Using a numerical model, already discussed in [8],..., [10], we analyze some base parameters of pouring process.

Paying respect for model functioning was realized a careful study of numerical, physical and technological parameters.

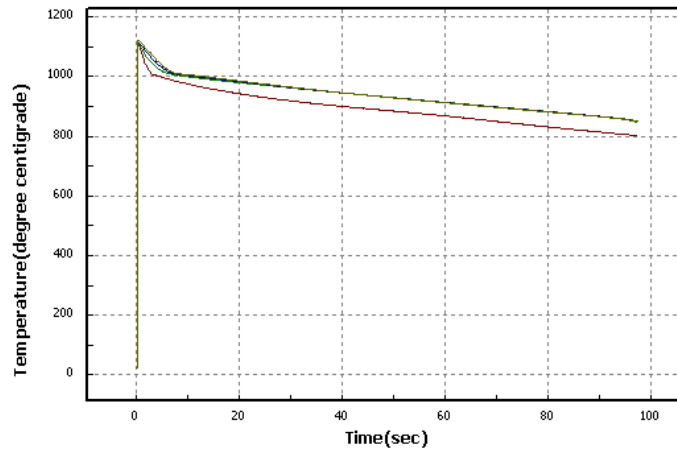


Fig. 3 – Variation of material temperature at the pouring beginning with time.

Temperature variation with time at the beginning of pouring is represented in Fig. 3 given important parameters of process.

During the analysis take place on our investigation we try to establish some process parameters given by process like solidification time – presented in Fig. 4a with precious information's about problem areas in solidification process like the yellow or red parts. In second image Fig. 4b is presented the registered result of the filling time showing the last part for fill were can also appear problems of solidification or material properties.

Figs. 5a and b present the solidification and filling sequence characterizing the pouring process by geometrical point of view of the sample.

Analyzing all computed results we can conclude on melting characteristics and improve the process parameters of each alloy we try to obtain paying respect for his properties.

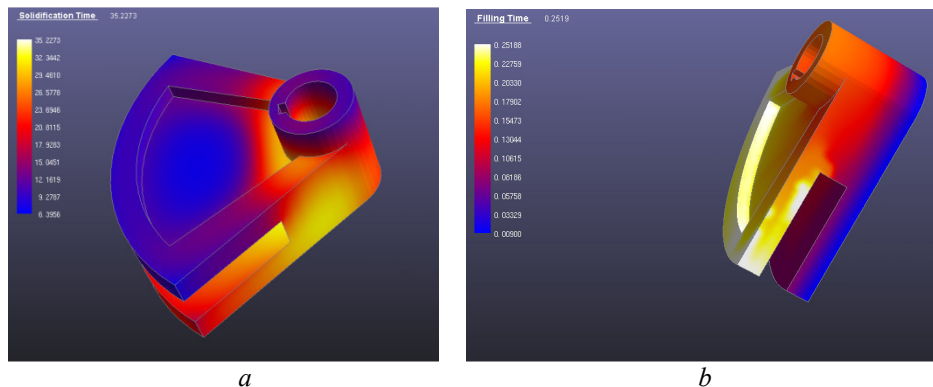


Fig. 4 – Backing sample: *a* – solidification time; *b* – filling time.

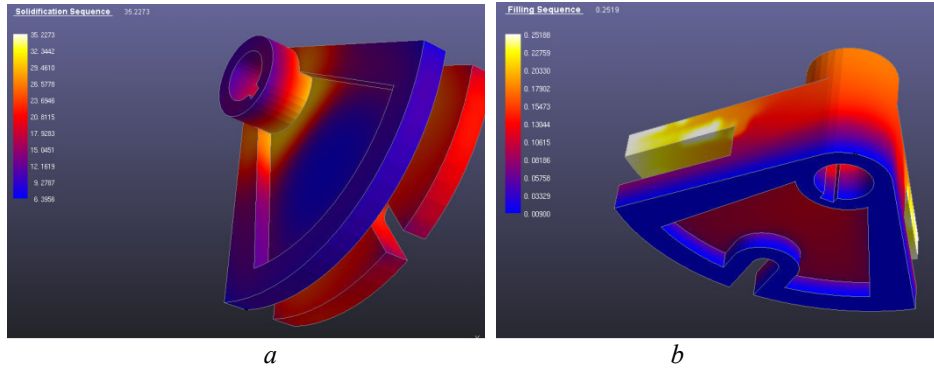


Fig. 5 – Backing sample: *a* – solidification sequence; *b* – filling sequence.

In Fig. 5 are present other two important properties the temperature gradient and reciprocal interface moving velocity that gives also information's on material pouring.

All the registered data, obtain by theoretical evaluation are presented in Table 3. Solidification time appreciation represent the most important parameter that influence material properties and his geometrical shape, to avoid problems that can appear like cavities that's the reason to investigate the numerical model response by this point of view. Results, except the first case, after five second, the model appreciate right the experiment being very close for total solidification point.

Table 3
Theoretical Results of Melting and Pouring Simulation of C83600 Commercial Alloy

Property	Filling time s	Solidification time s	Temperature gradient s	Local solidification time s	Reciprocal interface moving velocity	Retained melt modulus	Retained melt surface area	Cooling rate s
Value	0.0135 - 0.25	6.3390 - 35.22	1.2896 - 77.3466	41.0923 - 91.1055	0 - 39.6489	0.03214 - 0.39746	0.315 - 127.22	1.5887 - 3.6760

A simulation model was developed to simulate the filling and the solidification behaviours of the blade components, cast in an automatic sand casting production line.

The verified model based on the experimental observations [11], showed that the virtual mould is suitable and getting a uniform cast quality of properties for all cast parts. The model also represented a different performance between the gates for each cast part, suggesting a smaller cross-sectional area

for the first gate to reduce the risk of air absorption. The present simulation model is able to study the effects of several casting parameters including the melt superheat, pouring time (velocity), mould surface roughness, gating design, and the mould configuration on the quality of mechanical cast parts.

5. Conclusions

Good result of comparative tests between experimental registered results and numerical calculus result promote the numerical method to be used in any initial case to reduce charges and gain experience on a special alloy casting. Between normal casting and solidification of a metallic material and virtual simulation, are not big differences using the right numerical model. It is more economical the virtual one, realized on computer obtaining an optimal variant of casting and solidification and faster as well.

Received: May 14, 2010

“Gheorghe Asachi” Technical University of Iași
Department of Materials Science
e-mail: jimlachi@yahoo.com

REFERENCES

1. Gäumann M., Sholapurwalla A., *Investment Casting Simulation*. Calcom SA, Lausanne, Switzerland, www.calcom.ch, 2) UES Software Inc., Annapolis MD, USA, www.ues-software.com.
2. Butnaciuc D., Mihai D., Ștefan M., Cimpoescu N., *Numerical Modeling of Alloys Solidification*. Bul. Inst. Polit. Iași, **LV (LIX)**, 1, s. Materials Science and Engineering, 145, 152 (2009).
3. Vizureanu P., *The Analysis of the Melting Process of the Materials in the Solar Furnaces*. Metalurgia Internat., **14**, 5, 5-9 (2009).
4. Cimpoescu N., Achiței D., Manole V., Hopulele I., Enache A., *Influence of Internal Friction on Shape Memory Alloy Based on Copper*. Metalurgia Internaț. Edit. Științifică F.M.R., 3, 33-36 (2009).
5. Soporan V., Constantinescu V., *Modelarea la nivel macrostructural a solidificării aliajelor*. Edit. Dacia, Cluj-Napoca, 1995.
6. Anders E.W., Jarfors Esa Ervasti, *Simulation and Modelling in Materials Processing*. Edit. Studentlitteratur, 2001.
7. Nelson L.H., *Solidification of Steel in Molds*. Trans. ASM, 22, 193 (1934).
8. Mihai D., *Rezistența materialelor*. Edit. Tehnopress, **II**, Iași, 250 (2004).
9. Ștefan M., Mihai D., et al., *Metode numerice și implementarea lor pe calculator*. Edit. Tehnopress, Iași, 2004.
10. Ștefan M., Mihai D., et al., *Tehnici de regresie și corelație în cercetarea experimentală*. Edit. Tehnopress, Iași, 2006.
11. Butnaciuc D., *Casting and Solidification Simulation of ot550-2 Roller*. Metalurgia International, Vol. **XIV**, 16, 81-86 (2009).

CURGEREA ȘI SOLIDIFICAREA COMPONENTELOR DE TĂIERE CU AJUTORUL SIMULĂRII NUMERICE

(Rezumat)

În lucrare s-a analizat o metodă virtuală de turnare și solidificare, investigându-se un aliaj pe bază de magneziu. S-a analizat o probă din magneziu utilizată în cazul pieselor tăietoare, componente pentru pompe, roți dințate mici, agitatoare și carcase etc. Avantajele metodei virtuale de turnare și solidificare sunt legate de timpul propriu-zis și de bani. O corespondență de aproximativ 90% dintre rezultatele practice și rezultatele numerice sunt de mare ajutor în orice caz.

BULETINUL INSTITUTULUI POLITEHNIC DIN IAȘI
Publicat de
Universitatea Tehnică „Gheorghe Asachi” din Iași
Tomul LVI (LX), Fasc. 3, 2010
Secția
ȘTIINȚA ȘI INGINERIA MATERIALELOR

FILLING AND SOLIDIFICATION SIMULATION OF A MOLDING PROCESS CONCERNING OBTAINING OF A BODY PIECE

BY

**DOREL BUTNACIUC, DAN-GELU GĂLUȘCĂ, MIHAI DUMITRU
and NICANOR CIMPOEȘU**

Abstract. Complex part samples are difficult to coordinate on molding process so simulation of this process is necessary to avoid losses or to improve the process. An aluminum based alloy molding, especially filling and solidification, is analyzed using a numerical model.

Key words: virtual casting, solidification, phase transformation, characteristics of melting, velocity.

1. Introduction

Continuous casting is globally one of the most noted processes of steelmaking or metallic materials and plays the leading role in industry in many countries. During continuous casting, heat transfer, metal solidification and stress-strain evolution in the solid shell in continuous casting mold will directly affect the production quality, and even contribute to the crack formation in the mold [1], [2]. Continuous casting is operated at high temperature above the steel melting point. Therefore, the measurement of temperature and stress is almost impossible. A full-scale physical simulation is also very difficult and expensive. Based on intensive research in the area, the physical phenomena of heat transfer with solidification and stress-strain evolution can be described by the mathematical model, which normally is represented by a set of differential or partial differential equations.

The engineering department then identifies the mechanical stability and establishes guidelines for finalizing the design of the component. Finally, the foundry brings the component into production, conforming to the stringent specifications provided by the designers. Inevitably, the foundry-man is always under tremendous pressure to produce excellent castings within a tight schedule and budget. Unfortunately the traditional approach rarely allows the foundry man to participate in the design and engineering phases prior to the costly production stage. In recent years, thanks to advanced computer aided technologies and casting process modeling, the traditional approach is becoming a thing of the past.

Process Simulation provides valuable information that facilitates participation by the foundry engineer early in the product development stage. This reduces the time between the concept stage and production stage in the life of a new component [2].

2. Blend use for Forming

For preparation of the used forming blend was used a quart sand mono granular delivered by S.C. MINDO S.A. Dorohoi, Botoșani with next characteristics:

- Medium granulation $M_{50} = 0,220$ mm
- Uniformity degree G.U. = 72%.

At forming blend preparation was used a sodium silicate as binding element added in 6% proportion from sand mass. Sodium silicate was purchased from S.C. CHIMFOREX S.A. Pleasa, Prahova, having next characteristics:

- | | |
|--------------------------------------|-------------------------|
| - Relative density | 1,54 kg/dm ³ |
| - Silicon dioxide | 31,5% |
| - Full alkalinity, Na ₂ O | 14 % |
| - Modulus | 2,32 |

Strengthening of forms is realized by CO₂ insufflations in proportion of 60% from sodium silicate mass.

Preparing of forming mixture was realized in a swirl mixer with discontinuous functioning.

In figure 1 are presented most important properties of the sand used for blending all of them in variation with temperature, paying respect for liquid metal temperature from the pouring time, during cooling process and at room temperature. It is very interesting to analyze de material density with temperature variation especially around 1200 °C were the material exhibit a maximum decrease.

Choosing the forming mixture by sand bind with sodium silicate was made based on next advantages:

- was not necessary the form drying;

- stuffing special operations of forming mixture was not requested;
- was not necessary forming frames which allow the placement after desire of thermocouples for temperature measurement from form cavity and from form wall;
- high mechanical resistance of form fact that permit a good manipulation of them, without degradation risks;
- big dimensional precision.

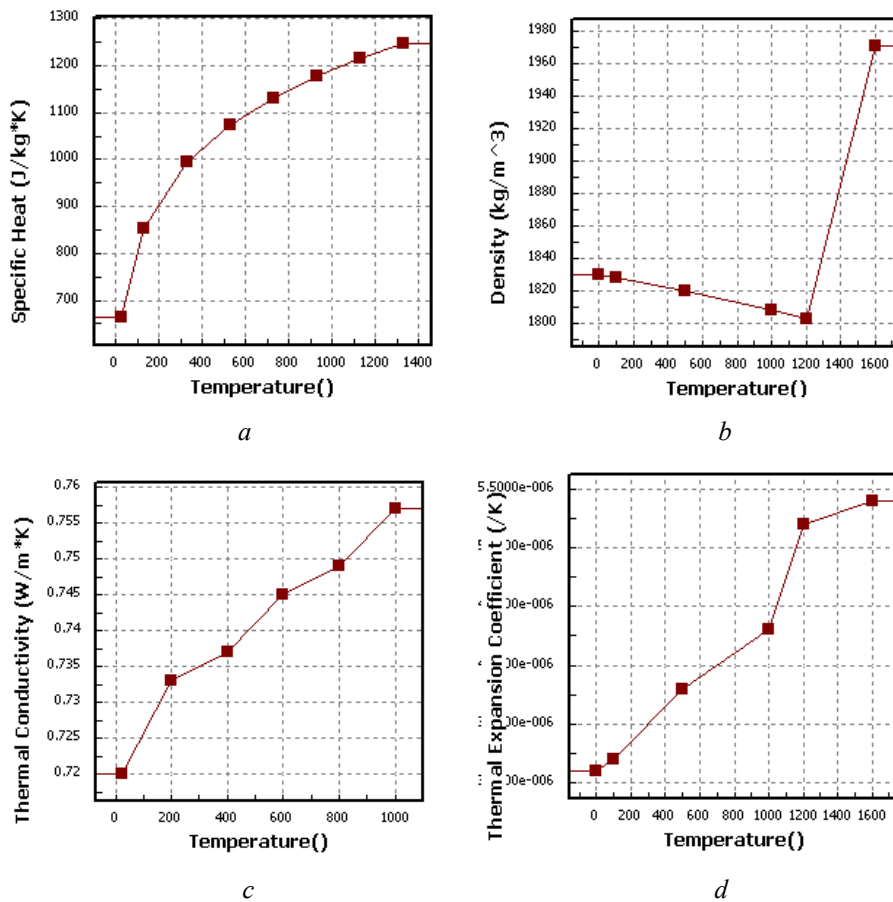


Fig. 1 – Sand use for blend properties: *a* – specific heat; *b* – density; *c* – thermal conductivity; *d* – thermal expansion coefficient.

Thermo-physic parameters of forming blend bind with sodium silicate are [3], [7]:

- density $\rho_{mixture} = 1550$ [kg/m³];
- caloric capacity $C_{pmixture} = 1170$ [J/kg grad];
- thermal conductivity $\lambda_{mixture} = 0,4$ [W/mK].

3. Experimental Details

Choosing a complex part like body part we analyze the material behavior at melting using a mathematical model evolve earlier [2].

In all researches concerning the melting process modeling, solidification and alloys contraction the simulation was realize on paralelipipedic bench marks type plate. Choosing this configuration is justified by problems complexity connected with modelation and established limit conditions [3].

As simulated melt material was used a CS43A- ASTM alloy, commercial material with extended applications [4],..., [6] characterizes by a chemical composition presented in Table 1.

Table 1
Chemical Composition of Investigated Alloy

Material: B 271 C83600				Standard: ASTM		Country: USA	
General	Composition	Cross-Reference	Mechanical properties	SmartCross			
Chemical Composition (%)							
Criteria	Min.	Max.	Approx				
Cu	84,0000	86,0000					
Zn	4,0000	6,0000					
Ni		1,0000					
Pb	4,0000	6,0000					
Sn	4,0000	6,0000					

Table 2
Melt Material Properties

Property	Value	Unit
Density	2790	kg/...
Specific Heat	963	J/kg*K
Thermal Cond...	121	W/...
Liquidus Temp...	625	
Solidus Tempe...	520	
Latent Heat	389000	J/kg
Dynamic Visco...	0.001116	kg/...
Coeff. of Ther...	Variable	/K
Vol. Change o...	7.14	%
Critical Solid Fr...	0.7	
Surface Tension	0.698	N/m

In alloy, an aluminum based alloy type CS43A elaboration the loading consist from:

- proper waste materials;

- copper ingot of technical purity;
- zinc waste as span and wires;
- brass waste materials;
- Pb10 alloy waste products [5].

Paying respect for material properties, presented in Table 2, for pouring simulation the behavior of thermal expansion coefficient with temperature present more interest.

All materials change their size when subjected to a temperature change as long as the pressure is held constant. In the special case of solid materials, the pressure does not appreciably affect the size of an object, and so for solids, it usually not necessary to specify that the pressure be held constant. The coefficient of thermal expansion describes how the size of an object changes with a change in temperature. Specifically, it measures the fractional change in volume per degree change in temperature at a constant pressure.

The volumetric thermal expansion coefficient is the most basic thermal expansion coefficient. All substances expand or contract when their temperature changes, and the expansion or contraction always occurs in all directions. Substances that expand at the same rate in any direction are called isotropic. Unlike gases or liquids, solid materials tend to keep their shape. For solids, one might only be concerned with the change along a length, or over some area.

Experimental results concerning the thermal coefficient behavior are presented in diagram from Fig. 2.

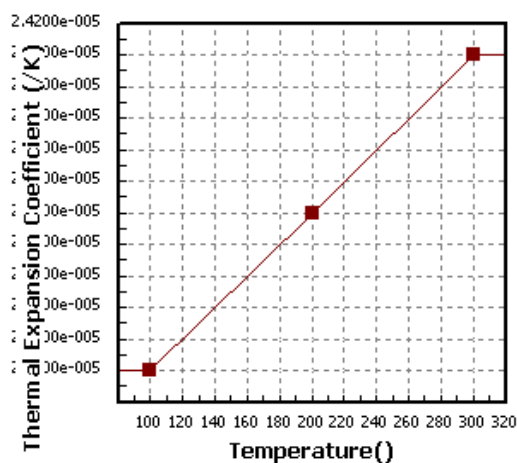


Fig. 2 – Thermal expansion coefficient variations with temperature.

Expansion coefficients are specially defined for these cases, and they are known as the linear and area expansion coefficients. However, they all come from the volume expansion coefficient, which explains how the substance expands in any direction.

4. Experimental Results

Working with a complicated geometry shape the molding process became more difficult having many areas with possible problems or defects appearing. Most important process parameters are centralized on Table 3 with some few different values, differences comparing to other tests [10], [11] appearing on solidification time and sequence with a huge value of 165.756 seconds most of this being because of the complicated geometrical shape.

Table 3
Molding Process Parameters

Properties	Filling time	Solidification time	Filling sequence	Solidification sequence	Temperature gradient	Cooling rate	Local solidification time
Values	0.009 0.6056	16,109 165.756	0.009 0.6056	16,109 165.756	0.122 25.3071	0.281 0.53	195.717 360.819

In Fig. 3 filling time, solidification time, cooling rate and local solidification time parameters are presented, simulated by time variation.

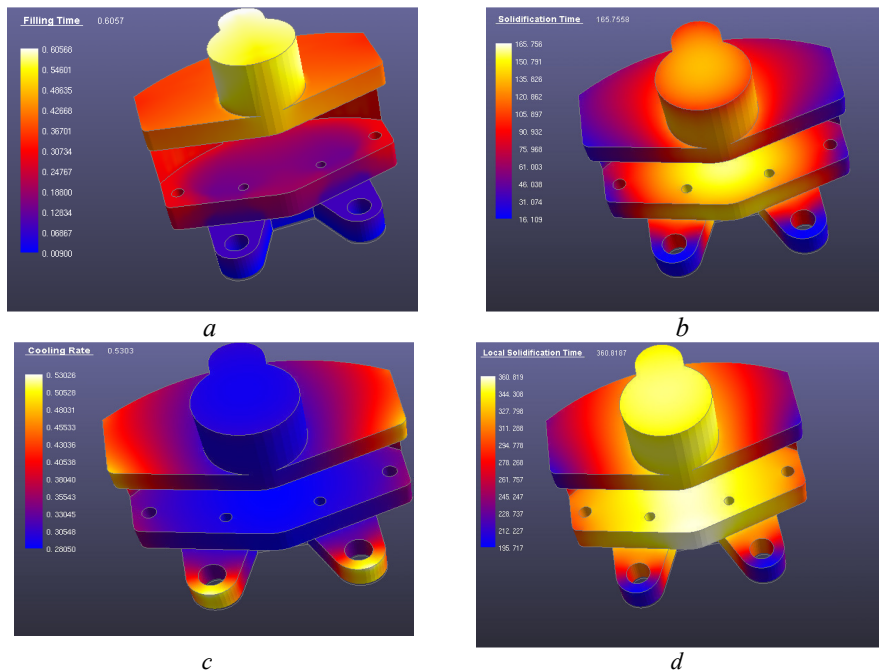


Fig. 3 – Most important molding parameters: *a* – filling time; *b* – solidification time; *c* – cooling rate; *d* – local solidification time.

Concerning the filling time the problems appear at the superior part

were the material reaches in 0.6056 seconds and in joint parts also.

The solidification time start with 16.109 seconds based on material properties and on geometrical piece shape the problematic part being on the inside part of the sample were the materials get to solidify in 165.756 seconds. Cooling rate confirm the filling time parameter so we have a reduce cooling rate were the material gets in the end and the faster rate, 0.53°C per second on the extremities were the material get inside first and meet the blend.

Local solidification time gives important information about critical points were combined with other information can conclude for a solution or to interfere from the parameters process point of view. At 360.819 seconds, the largest solidification period, the material can occur different phenomena and not reaching the propose characteristics.

3. Conclusion

- Good result of comparative tests between experimental registered results and numerical calculus result promote the numerical method to be used in any initial case to reduce charges and gain experience on a special alloy casting.

- Between normal casting and solidification of a metallic material and virtual simulation, are not big differences using the right numerical model. It is more economical the virtual one, realized on computer obtaining an optimal variant of casting and solidification and faster as well.

- Realizing a numerical simulation the producer gain time, materials and energy decreasing the production cost of the final pieces and having the possibility to improve all the process parameters.

- Choosing from a large scale of materials with similar properties for a single piece can be taken the best choice and reduce most of the molding problem.

Received: May 14, 2010

“Gheorghe Asachi” Technical University of Iași,
Department of Materials Science
e-mail: jimlachi@yahoo.com

REFERENCES

1. Samarasekera I.V., Brimacombe J.K., *Steelmaking*. Conf. Proc., 74, 55–67 (1991).
2. Thomas. B.G., In: Dantzig J., Greenwell A., Michalczyk J. (Eds.), *The Encyclopedia of Advanced Materials*. Vol. 2, Pergamon Elsevier Sci. Ltd., Oxford, UK, 1999.
3. Gäumann M., Sholapurwalla A., *Investment Casting Simulation*. Calcom SA, Lausanne, Switzerland, www.calcom.ch, 2) UES Software Inc., Annapolis MD, USA, www.ues-software.com.
4. Butnaciuc D., Mihai D., Ștefan M., Cimpoeșu N., *Numerical Modeling of Alloys*

- Solidification*. Bul. Inst. Polit. Iași, **LV (LIX)**, 1, s. Materials Science and Engineering, 145, 152 (2009).
5. Vizureanu P., *The Analysis of the Melting Process of the Materials in the Solar Furnaces*. Metalurgia Internat., Vol. **14**, 5, 5-9 (2009).
 6. Soporan V., Constantinescu V. *Modelarea la nivel macrostructural a solidificării aliajelor*. Edit. Dacia, Cluj-Napoca, 1995.
 7. Anders E.W., *Jarfors Esa Ervasti – Simulatoir and Modelling in Materials Processing*. Edit. Studentliteratur, 2001.
 8. Ștefan M., Mihai D., et al. *Metode numerice și implementarea lor pe calculator*. Edit. Tehnopress, Iași, 2004.
 9. Ștefan M., Mihai D., et al., *Tehnici de regresie și corelație în cercetarea experimentală*. Edit. Tehnopress, Iași, 2006.
 10. Butnaciuc D., *Casting and Solidification Simulation of ot550-2 Roller*. Metalurgia Internat., Vol. **XIV**, 16, 2009.

SIMULAREA SOLIDIFICĂRII ȘI UMLERII A UNUI PROCES DE TURNARE ÎN VEDEREA OBTINERII UNEI PIESE TIP CORP

(Rezumat)

Probele cu o geometrie complexă sunt dificil de urmărit din punct de vedere al simulării procesului de turnare care este necesară în scopul diminuării pierderilor de proces sau chiar pentru îmbunătățirea acestuia. Folosind un model numeric procesul de turnare, în special umplerea și solidificarea, a fost analizat pentru un aliaj pe bază de aluminiu.

RESEARCH ON ANALYSIS OF JOINT AREA BIMETALIC BUSHES GRIP

BY

SANDA CREȚU and DAN-GELU GĂLUȘCĂ

Abstract: The paper presents a study on the bimetallic bushes joint area grip.

Key words: grip, joint area, bimetallic bushes

1. Theoretical Aspects

Bimetallic bushes characteristics are determined by the characteristics properties of the components metallic materials and by the manufacture process. Big majority of bimetallic bushes characteristics can be assessed through values indicators such as: traction resistance, flow limit, hardness, elasticity module, electric resistance, thermal conductivity, thermal dilatation, technology try behavior, structural component, specify grip and corrosion resistance.

Bimetallic layers mechanical characteristics depend of components characteristics, especially of basis metallic materials properties.

In Table 1 are presented mechanical characteristics guide of some bimetallic layers used in metallurgical industry and cars building.

Besides bushes traction resistance, hardness and the relationships between layers thickness, bimetallic bushes resistance depends by components joint technology. If the metals suffered a hardening through aging and the joint proces is accompanied by a powerfull ecruisare, it can estimate an bimetallic components resistance and hardness growth.

For example, carbon steel-stainless steel bimetal differs from stainless steel through more advantageous properties: higher thermal conductivity advantage the use of bimetal on machines construction in chemical industry, working under heat action (heat changing).

In general, thermal conductivity of bimetallic bushes is much higher than by the laid-down material.

Table 1
Main Mechanical Characteristics of Some Bimetallic Components

Nr. crt.	SD – Layed-down material	MB –Base material	State	Traction resistance R_m (N/mm ²)	Conventional flow limit R_p (N/mm ²)	Elongation A_5 (%)
1.	Copper	Carbon steel	Deposition through casting	520	357	20
2.	Copper	Stainless steel	-	343	252	12,5
3.	Brass	Carbon steel	casting-distortion	428	224	31
4.	Bronze	Carbon steel	-	460	245	35
5.	Carbon steel	Stainless steel	-	550	400	35

Like thermal conductivity, bimetallic components thermal dilatation in perpendicular direction is different from the one in parallel direction. Bimetallic thermal dilatation quotient used in general much lesser than Cr-Ni austenitic steels, and other metals.

Bimetallic layers hardness depends on components hardness and joints nature. Electric conductivity and electric resistance and density is determined by calculating weighted media of these properties, considering components volumetric proportion. Unalloyed carbon steels magnetic permeability is hundreds of times higher than Cr-Ni austenitic steels, which leads to the use of austenitic carbon-steel bimetallic components for heated pots through induction (Cr-Ni austenitic steel pots cannot be heated through induction). The bimetallics formed from different dilatation quotient components tend to deform or to bend, this property characterizing thermobimetallics used at thermoregulators manufacture.

2. Traction Through Breaking Resistance Consideration

Specific adhesion determination is made through developed methods by scientific researchers that are a result of the made researches and field experience. Thus on world plane specific adhesion determination of the components joints and the bimetallic auto pieces are made through bend testing, twisted, shear detachment and avulsion detachment.

A complete relationship of bimetallic auto bushes break resistance

determination has to consider elasticity modules and components flow limits. The proposed formula for bimetallic break resistance determination is given by relationship 1.

$$(1) \quad R_m = R_{m1} \frac{g_1}{g_1 + g_2} + R_{p2} \frac{g_2}{g_1 + g_2} + \frac{1}{2} (R_{m2} - R_{p1}) \frac{g_2}{g_1 + g_2}, [\text{N/mm}^2]$$

where:

- R_m – bimetallic auto components break resistance, $[\text{N/mm}^2]$;
- R_{m1} – basis material break resistance, $[\text{N/mm}^2]$;
- R_{p1} – basis material flow limit, $[\text{N/mm}^2]$;
- R_{m2} – layed-down layer break resistance, $[\text{N/mm}^2]$;
- R_{p2} – layed-down layer flow limit, $[\text{N/mm}^2]$;
- g_1 – basis material thickness, $[\text{mm}]$;
- g_2 – layed-down layer thickness, $[\text{mm}]$.

If during bimetallic specimen traction request, both components reach the plastic state, the tensions between the two layers is determined with relationships:

$$(2) \quad R_1 = E_{r1} \cdot \varepsilon + R_{p1} \left(1 - \frac{E_{r1}}{E_1}\right), [\text{N/mm}^2]$$

$$(3) \quad R_2 = E_{r2} + R_{p2} \left(1 - \frac{E_{r2}}{E_2}\right), [\text{N/mm}^2]$$

where:

- R_{p1}, R_{p2} – basis material flow limit respectively layed-down layer, $[\text{N/mm}^2]$;
- E_1, E_2 – the basis material elasticity modules, respectively layed-down layer, $[\text{N/mm}^2]$;
- E_{r1}, E_{r2} – basis material hardening modules, respectively layed-down layer, $[\text{N/mm}^2]$;
- ε – bimetallic sample axis destortion.

When request forces on traction act parallel with formulas bimetallic semimanufactured layers for E elasticity module calculation, of R_p flow limit, of R_m conventional traction break resistance and R_k real, are the following:

$$(4) \quad E = E_1 b_1 + E_2 b_2$$

$$(5) \quad R_p = R_{p1} b_1 + R_{p2} b_2$$

$$(6) \quad R_m = R_{m2}b_2 + R_{p1}b_1 + \frac{\varepsilon_{u2}}{\varepsilon_{u1}}(R_{m2} - R_{p1}) \cdot b_1, [\text{N/mm}^2]$$

$$(7) \quad R_k = R_{k1}b_2 + R_{m1}b_1 + \frac{\Psi_2}{\Psi_1}(R_{k1} - R_{m1}) \cdot b_1, [\text{N/mm}^2]$$

where:

$b_1 = \frac{A_1}{A}$ - 1 material relatively content;

A_1, A_2 - 1 and 2 materials proper areas in the bimetallic sample of the cross section, [mm^2];

A - bimetallic sample of the cross section area, [mm^2];

$\varepsilon_{u1}, \varepsilon_{u2}$ - 1 and 2 material maximum uniform distorsion;

R_k - real resistance on breaking, [N/mm^2];

Ψ_1, Ψ_2 - 1 and 2 material bottleneck.

Index 1 refers to the metallic material less resistant, and index 2 to the most resistant (in the case of carbon-bronze steel bimetallic auto bushes, 1-bronze, 2-steel carbon).

In the case of components and bimetallic bushes, the type of the tube for the resistance and elasticity mechanical attempts is made after the rules and standards in force for the basis material, considering bimetallic semimanufactured being like a piece formed from the basis material.

3. Bimetallic Layers Structure Analysis

Bimetallic bushes like hypoeutectoid steel - CuNiAl alloy can be hardened through aging treatment for resistance growth to wear. After this treatment, an intensification of the precipitation process take place of the chemical compounds that leads to the layed-down hamdning. For pointing this compounds, is used a modern analysis method of the bimetallic layers-mass spectrometry through ion withdrawal, with the help of laser microprobe. Through laser beam interaction with the sample, we achieve qualitative and quantitative information on presented elements in analyzed sample, pointing the precipitation phenomenon and they're influence on bimetallic layers characteristics.

This method is based upon the sample irradiation with an laser beam with dielectric solid activ environment, respectively a ruby laser doped with Cr³⁺ ion or doped garnet with neodymium. Big powerfull laser beam, focused finely on sample, produces the energy transmission towards the sample, followed by a powerfull warming untill tha sample material evanescence, with the achieving of an minicrater with 3-5 μm diameter, materialized through ions appearance, atoms or molecules, characterized for the irradiated material, that

are captured with the help of an optoelectronic system of ionic withdrawal and analysed with the help of a mass spectrometer. Thus are obtained qualitative and quantitative informations about presented elements in the analyzed sample.

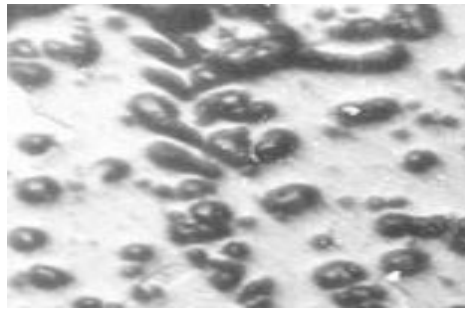


Fig. 1 – CuNiAl type of bronze alloy treated (hardening by solution release+ 484C/1,5h/apa). Electronic microscopy (x2500)-high density of incoherent precipitated in the basis matrix.

The obtained images for analyzed alloy, presented in figure 2, point out a relatively uniform distribution of Ni atoms on the layered-down surface and from near joint area. Samples being in treated state, is possible that nickel crowd pointed out to represent some basis compounds of precipitated nickel, Ni_2Si most probably.

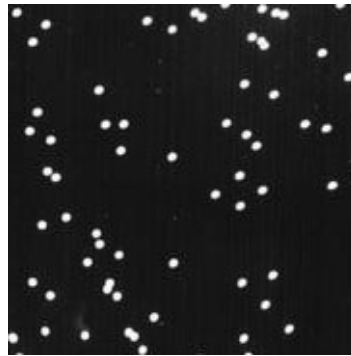


Fig. 2 – Ni atoms repartition in taken samples from CuNiAl layered-down in treated state. Rays X microscopy. X3000 enlarge.

4. Conclusions

The laser beam irradiation has been performed on chemical compounds presented in the bimetallic samples microstructure.

In the sample's microstructure is optic visualised the chemical compounds

categories, pointing out they're composition obtained by spectrometry.

Depending on the percentajes of the chemical elements obtained for chemical compounds categories, it can infer with aproximation the chemical formulas for chemical compounds from near joint area.

Ni₂Si precipitates with an high intensity having a uniform distribution, controbuting at the growth of layed-down layer hardness and at waer out resistance of the bimetalic auto compound.

CuNiAl type of layed-down alloy hardness and thermal treated through aging occurs thanks to the precipitation from Cu oversaturated solid solution with chemical compounds based on Ni respectively Ni₂Al and Ni₂Si₅.

Received: May 14, 2010

“Gheorghe Asachi” Technical University of Iași,
Department of Materials Science
email: cretu.sanda@yahoo.com

REFERENCES

1. Allan M., *Principles of Measurement and Instrumentation*. Prentice Hall Internat. Inc., 1993.
2. Corăbieru P., *Researches Regarding the Influence of the Metalurgical Factors About Layers and Characteristics Structure Bimetallic*. CNM-98, București, 1998.
3. Soporan V, Vermeșan H., *Considerations Regarding Modeling Process Occurring Within the Surface Engineering*. Cap. XVI, vol. Advanced Processes in the Surface Engineering, Edit. UTPRES, Cluj-Napoca, 1998.
4. Gluster P.J., Trueblod K.N., *Crystal Structure Analysis*. Oxford Univ. Press, 1985.
5. Hirst M.D., *Potențial Energy Surface*. Taylor and Francis, Edit. London, 1985.
6. Schmid-Fetzer, R., Grobner, J., *Advanced Engr. Materials*, **3**, 12, 947 (2001).

CERCETĂRI PRIVIND ANALIZA ADERENȚEI ZONEI DE ÎMBINARE A BUCȘELOR METALICE

(Rezumat)

Lucrarea prezintă un studiu asupra aderenței zonei de îmbinare a bușelor bimetalice.

ANALYSIS OF THE ULTRASOUNDS SURFACE EFFECT DURING THE TUBES DRAWING IN SONODRAW SYSTEM

BY

BOGDAN-LUCIAN GAVRILĂ*, **MIHAI SUSAN***, **PETRU DUMITRAȘ****,
DRAGOȘ CRISTIAN ACHIȚEI*, **VIOREL ILIESCU*****
and **BRIAN-TUDOR LANDKAMMER***

Abstract. The paper gives a definition and explains the “ultrasounds surface effect” or the “reduction of the metal-tool contact friction” phenomenon which take place during the tubes without inside guard drawing process; it makes their technological analysis, considering the relative drawing velocity ($v_{tr} / \overline{v_v}$), v_{tr} - rate of drawing which defines the technologic efficiency and $\overline{v_v}$ - vibratory rate of the die ($\overline{v_v} = 2 \pi f A$), which gives enough information about the ultrasound equipment used for the generation and transfer of the ultrasounds energy. The tubes without inside guard drawing process, in SONODRAW system, is used in the processing of the tubes with thin walls, made from metallic materials which are hard malleable by cold drawing / work hardenable, in the next condition: $v_{tr} / \overline{v_v} \ll 1$.

Key words: tubes, ultrasounds, ultrasounds surface effect, ultrasound energy reflectors, relative drawing velocity.

1. Introduction

The tubes drawing may be over inside guard (over supported plug, over floating plug or over mandrel) or without inside guard.

Depending on the ratio g/D (g -thickness of the wall, D -diameter of the processed tube), the tubes may have thin walls ($g/D \leq 0,21$) or thick walls ($g/D > 0,21$), [1], [2]. At the present moment, for the case of without inside guard drawing processes, of the thin walls tubes, made from cold hard malleable

metallic materials and work hardenable, too, SONODRAW system will apply, [3], ..., [6].

The case of without inside guard drawing processes of the tubes, in SONODRAW system, means a processing with ultrasonic vibrations which are sent to the die, along the drawing direction; so, during the plastic deformation, it will obtain the “ultrasounds surface effect” or the “reduction of the metal-tool contact friction”, [3], [7]. The wanted effect of the ultrasonic energy will be obtained when the ultrasounds will have high values of energy-ultrasounds longitudinal waves, as standing waves, with the die placed in a top position of the wave oscillation. The ultrasonic or ultrasounds waves are a variety of the elastic waves which have the frequency values between 16000 Hz and 10^{10} Hz. Fig. 1 presents a stable system of standing waves, with vertexes (minimum amplitude of the wave oscillations) and antinodes (maximum amplitude of the wave oscillations).

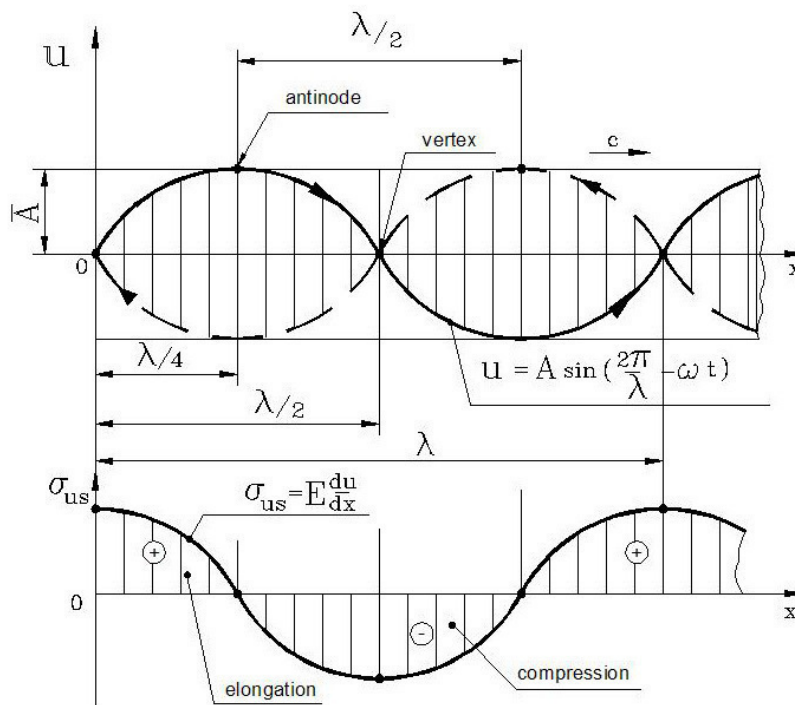


Fig. 1 – Standing waves system [6]: u – motion of the wave; c – ultrasounds wave velocity; λ – wavelength; \bar{A} – oscillation amplitude of the wave / maximum value:
 ——— running wave; - - - - regressive wave.

For the case of without inside guard drawing processes of the tubes, in SONODRAW system, it will use the oscillator systems, as Fig. 2 shows.

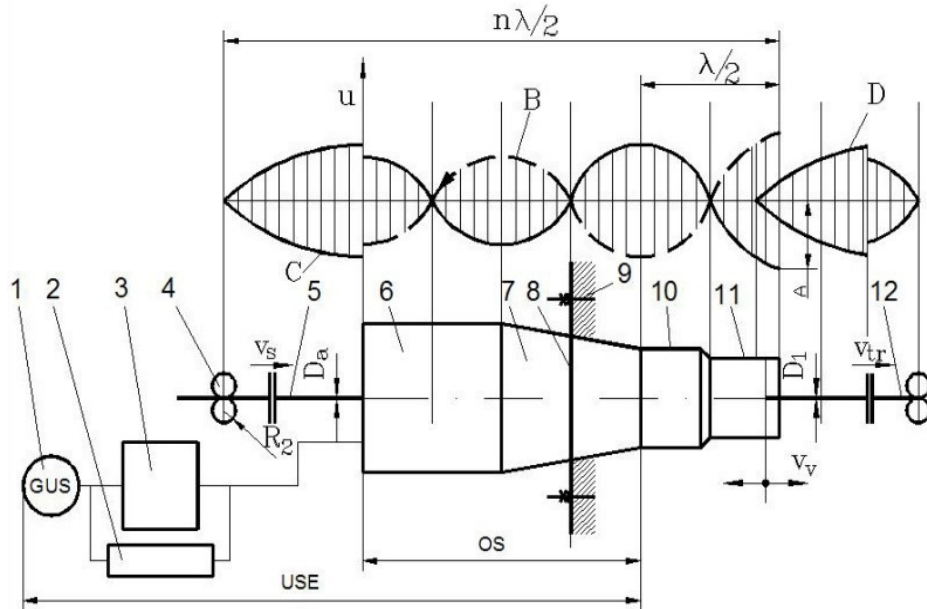


Fig. 2 – Oscillator system of the tubes without inside guard drawing process, in SONODRAW system, [6]: 1 – ultrasounds generator; 2 – direct current source; 3 – polarization block; 4, 13 – ultrasound energy reflector (presser roll); 5 – rough tube; 6 – magnetostrictive magnetic amplifier; 7 – conic concentrator; 8 – nodulated flange; 9 – resistance structure /frame of machine; 10 – graded hardened concentrator; 11 – die; 12 – processed tube: D_0 , D_1 – diameter of the rough and of the processed tube; v_{tr} – rate of drawing; \bar{v}_v – maximum value of the vibratory rate; A – amplitude of the die oscillation; B – wave oscillation at the oscillator system level / OS; C – wave oscillation of the rough tube; D – wave oscillation of the processed tube: ——— running wave; - - - - regressive wave.

The ultrasonic energy reflectors / presser rolls (R_1 and R_2) must limit the effect of the ultrasonic energy on well-known distances, distances which are result of the standing waves stable system forming mechanism, in the tube, [3], [6], [7].

2. Developing of the Ultrasounds Surface Effect

Principle scheme of the tubes without inside guard drawing process, in SONODRAW system, is shown in Fig. 3.

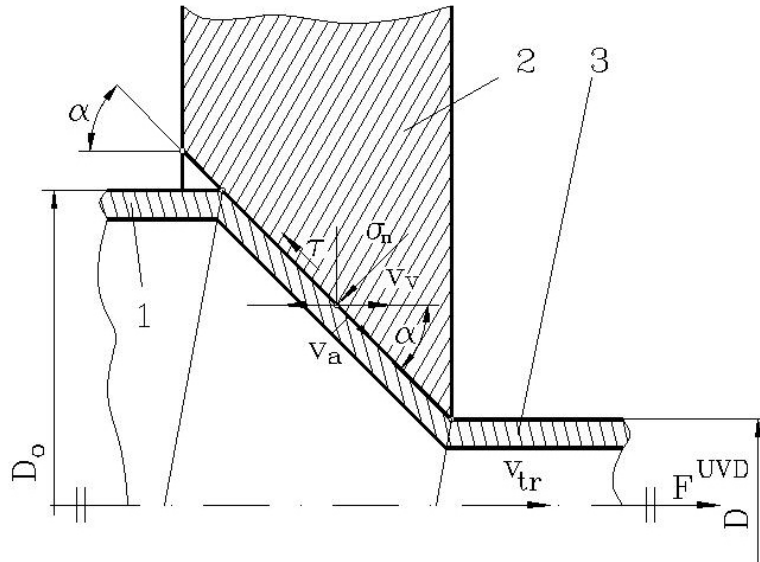


Fig. 3 – Principle scheme of the tubes without inside guard drawing process, in SONODRAW system, [6]: 1 – rough tube; 2 – die; 3 – processed tube; D_o – external diameter of the rough tube; D_1 – external diameter of the processed tube; P – arbitrary point placed at the metal-tool interface; α – semiangle of the die cone; σ_n – normal stress in the considered point; τ – shear stress at the metal-tool interface; F^{UVD} – drawing force / SONODRAW system; v_v – vibratory rate of the mould; v_a – moving velocity of the metal; v_{tr} – rate of drawing.

The developing of the “ultrasounds surface effect” or of the “reduction of the metal-tool contact friction” during the tubes without inside guard drawing process, in SONODRAW system, is based on the Severdenko’s model, [3] and on the theoretical one, too, [7], when the friction is assumed as a Coulomb-type and considering the “reversion mechanism” of the mean friction force. So, Fig.4 presents the developing of the “reversion mechanism” of the mean friction force at the metal-tool contact, based the Severdenko’s model and on the theoretical one, too, [3], [7].

The Figs. 3 and 4 show that, an arbitrary point P, placed in the deformation focus area, make two kinds of movement: a feed movement, along the cone element of the die, with v_a velocity, and a vibration movement, with v_v velocity.

The vector of the friction force, (\vec{F}_f) , in classical technology-TC, subtends to the direction of the metal moving velocity (\vec{v}_a) , but in the case of SONODRAW technology, it subtends to the resultant vector-the composition vector of the rates (\vec{v}_v) and (\vec{v}_a) .

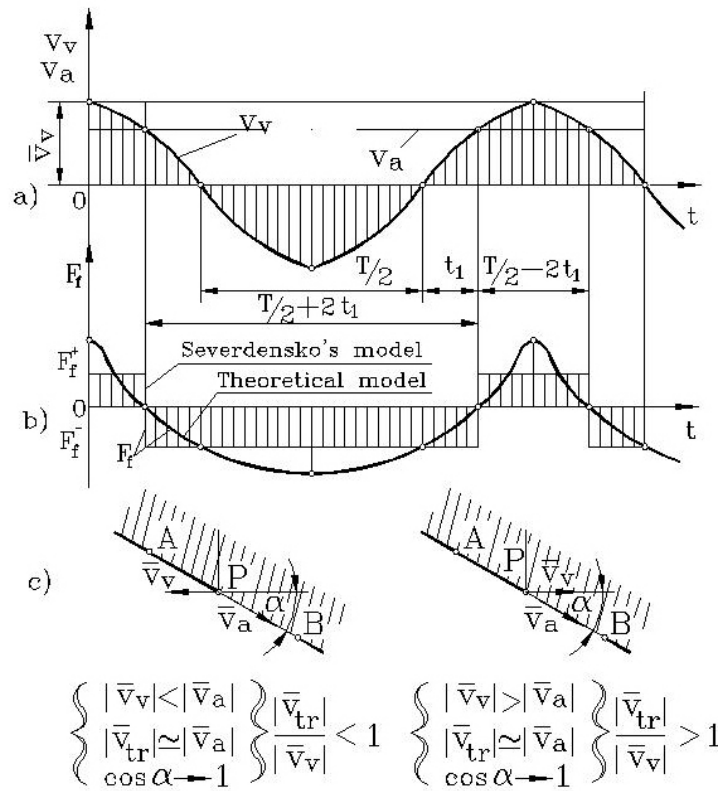


Fig. 4 – The “reversion mechanism” of the mean friction force at the metal-tool contact, [3], [7]: *a* – variation of the metal rate of drawing (v_v) and of the slip rate (v_a); *b* – reversal of the mean friction force (F_f^-, F_f^+)- Severdenko’s model and the theoretical one, too; *c* – reversal of the mean friction force depending on the relative rate of drawing (v_{tr} / v_v).

In the case of SONODRAW technology, the resultant vector of the relative drawing velocity, $(\bar{v}_{tr} / \bar{v}_v)$, will change the motion direction of the point P in this way: during $T / 2 - 2t_1$, at a complete cyclic period level (T), its motion is similarly with those of the metal one, when $|\bar{v}_{tr} / \bar{v}_v| < 1,0$ and, in an opposite direction, during $T / 2 + 2t_1$, $(\bar{v}_{tr} / \bar{v}_v) > 1$. So, this consideration explains the “reversion mechanism” of the mean friction force, in the metal-tool contact area, [3], [7]. This means that, during $T / 2 - 2t_1$, the friction force is positive and during $T / 2 + 2t_1$, (when the proper plastic deformation of the metal takes place), the friction force is negative. During $T / 2 - 2t_1$, it takes place the

elastic deformation at the most. This is the way to explain the fractional character (in impulses), too, of the plastic deformation process, when the mould is placed in the maximal position of the wave oscillation (antinodes) and it is ultrasonic activated, on the drawing direction (for example: when the frequency of the oscillation is 20000 Hz, it takes place the mould removing away from the processed metal, 20000 times per second). Knowing that, in cold drawing technology of the tubes made from hard malleable metallic materials, the semiangle of the die cone is between 6° and 10° ($\cos \alpha \rightarrow 1$), assuming $v_{tr} \approx v_a$, [1],..., [3].

Assuming the Coulomb-type contact friction case, the frictional coefficient in classical technology-TC, (μ^{TC}) is given by the next relation:

$$(1) \quad \mu^{TC} = \frac{\tau}{\sigma_n},$$

where: τ – shear stress due to the friction; σ_n – normal stress in an arbitrary point considered placed at the metal-tool interface area.

The frictional coefficient, (μ^{UVD}), in the case of SONODRAW technology, is smaller than the same coefficient, in the case of classical technology-TC, the difference being a term which includes the influence of the elastic waves, ($4t_1/T$), noted ξ , [3], [7].

In these conditions, the frictional coefficient, (μ^{UVD}), is:

$$(2) \quad \mu^{UVD} = \frac{\tau}{\sigma_n} - \frac{2t_1}{T} \times \frac{\tau}{\sigma_n} = \frac{\tau}{\sigma_n} - \frac{4t_1}{T} \times \frac{\tau}{\sigma_n} = \mu^{TC} \times \left(1 - \frac{4t_1}{T}\right)$$

or

$$\mu^{UVD} = \mu^{TC} \times (1 - \xi), \quad 0 < \xi < 1$$

Assuming the ultrasound wave motion which follows the motion law, $u = A \sin \omega t_1$, the vibratory rate will be determined as the time derivative of the movement:

$$(3) \quad v_v = \frac{du}{dt} = |A\omega \cos \omega t_1|$$

The maximal value of the mould vibratory rate, (\bar{v}_v), will be obtained assuming the condition $\cos \omega t_1 = 1$, meaning:

$$(4) \quad \bar{v}_v = \omega A = 2\pi \cdot f \cdot A = \frac{2\pi}{T} A,$$

where: f is the resonant frequency of the oscillator system.

Considering relations (3) and (4), it will result:

$$(5) \quad v_a = \bar{v}_v \cdot \cos \omega t_1$$

Considering relation (5), it will result t_1 :

$$t_1 = \frac{1}{\omega} \arccos \frac{v_a}{\bar{v}_v}, \quad \left| \frac{v_a}{\bar{v}_v} \right| < 1$$

Assuming, from the technological point of view, $v_{tr} \approx v_a$, it can notice that:

$$(6) \quad t_1 = \frac{1}{\omega} \arccos \frac{v_{tr}}{\bar{v}_v}, \quad \left| \frac{v_{tr}}{\bar{v}_v} \right| \leq 1$$

So, knowing t_1 anterior determined, it will obtain the effective influence factor of the ultrasound oscillations up to the contact friction metal-tool, (ξ):

$$(7) \quad \xi = \frac{2}{\pi} \arccos \frac{v_{tr}}{\bar{v}_v}$$

Considering relations (2) and (7), the frictional coefficient, (μ^{UVD}), in point P, placed at the metal-tool interface, is:

$$(8) \quad \mu^{UVD} = \mu^{TC} \left(1 - \frac{2}{\pi} \arccos \frac{v_{tr}}{\bar{v}_v} \right), \quad \left| \frac{v_{tr}}{\bar{v}_v} \right| \leq 1,0$$

3. Analysis Elements of the Ultrasounds Surface Effect During the Tubes Without Inside Guard Drawing Process, in SONODRAW System

Assuming the Coulomb-type friction for the tubes drawing, in SONODRAW system, and considering some information included in paragraph 2 and Fig.4 above presented, it can observe that, knowing the technological supposition $v_{tr} \approx v_a$ (when $\cos \alpha \rightarrow 1$), the analysis of the

ultrasounds surface effect depends on the ratio v_{tr} / \bar{v}_v which is named *the relative drawing velocity*, [3], [5], ..., [7]. This aspect is considered when $v_{tr} / \bar{v}_v \leq 1,0$. This is the case of without inside guard drawing process of the tubes made from cold hard malleable metallic materials / work hardenable, which have the semiangle of the die cone, (α), between 6° and 10° , [1, ..., [3], [6].

The relative drawing velocity, (v_{tr} / \bar{v}_v), becomes very important, too, because v_{tr} is a variable which defines the technological efficiency and \bar{v}_v gives enough information about ultrasonic equipment / EUS, (Fig.2), used for the generation and the transfer of the ultrasonic energy by parameters f and A , ($\bar{v}_v = 2\pi \cdot f \cdot A$, rel. 4).

Knowing that $\mu^{UVD} < \mu^{TC}$, it can conclude that the forces necessary, for the tubes without inside guard drawing process, will keep the same kind of dependence relation, $F^{UVD} < F^{TC}$, where F^{UVD} is the drawing force in SONODRAW system and F^{TC} is the drawing force in the case of classical technology-TC. So, it can conclude that, in the case of the tubes drawing in SONODRAW system, the safety of drawing increases as the next relation shows, [1], [2]:

$$(9) \quad c_{st} = \frac{S \cdot R_m}{F},$$

where: c_{st} -safety of the draw coefficient; S -cross section area of the processed tube; R_m -mean resistance to rupture of the tube; F -drawing force (F^{UVD} or F^{TC} , $F^{UVD} < F^{TC}$).

The efficiency of the ultrasonic energy, based on the “ultrasounds surface effect”, may be estimate by the relative decreasing of the frictional coefficient, ($\Delta\mu$), as the next relation shows [6]:

$$(10) \quad \Delta\mu = \frac{\mu^{TC} - \mu^{UVD}}{\mu^{TC}} \cdot 100, [\%]$$

Based on the resonant frequency, (f), of the oscillator system/SO, (Fig. 2), it can dimension the concentrators of ultrasound energy (conical or graded cylindrical), using relation, [4], [6]:

$$(11) \quad \lambda = \frac{c}{f}$$

where: λ –wavelength; c –wave velocity of ultrasounds in the certain medium, ($c_{steel}= 5050$ m/s); f –resonant frequency.

Table 1 shows the variation μ^{UVD} and $\Delta\mu$, depending on the relative drawing velocity, v_{tr}/\bar{v}_v , (values which were calculated for \bar{v}_v and μ^{UVD} using relations (4) and (8)).

Tabel 1

Variation μ^{UVD} and $\Delta\mu$ Depending on the Relative Drawing Velocity, v_{tr}/\bar{v}_v

No	A μm	f Hz	v_{tr} m/s	\bar{v}_v m/s	v_{tr}/\bar{v}_v	μ^{TC}	μ^{UVD}	$\Delta\mu$ %
1	5	20000	0,33	0,56	0,58	0,03	0,0123	59
2	10	20000	0,33	1,13	0,29	0,03	0,0060	80
3	15	20000	0,33	1,69	0,19	0,03	0,0040	87
4	20	20000	0,33	2,26	0,14	0,03	0,0030	90
5	25	20000	0,33	2,82	0,11	0,03	0,0027	91
6	30	20000	0,33	3,39	0,09	0,03	0,0024	92
7	35	20000	0,33	3,95	0,08	0,03	0,0021	93
8	40	20000	0,33	4,52	0,07	0,03	0,0018	94

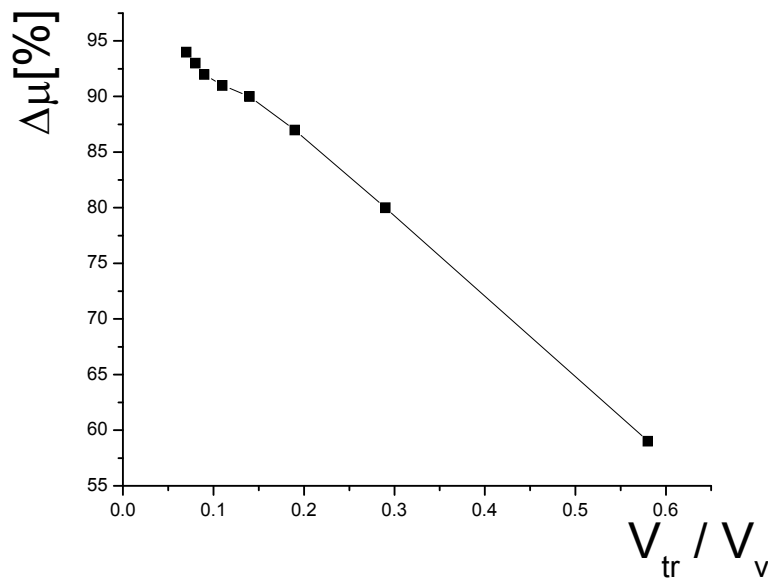


Fig. 5 – The variation of relative decreasing of friction coefficient ($\Delta\mu$) depending on the relative drawing speed (V_{tr} / V_v).

3. Conclusion

The “ultrasounds surface effect” or the “reduction of the metal-tool contact friction” phenomenon, during the tubes without inside guard drawing process, in SONODRAW system, is obtained when the die is placed in the maximal position of the waves oscillations and it is activated on the direction of the drawing. The developing of the “ultrasounds surface effect” is based on Severdenko’s model and on the theoretical one, depending on the “reversal of the mean friction force” in the contact between metal and tool area, assuming the Coulomb-type friction.

The wanted effect of the ultrasound energy during the technological processes of the tubes drawing takes place when it will use ultrasounds which have high energies-longitudinal ultrasound waves as standing waves which generate vertexes/minimal and antinodes/maximal of the waves oscillations. For a better efficiency of the ultrasound energy obtaining, during the tubes without inside guard drawing processes, in SONODRAW system, it will use ultrasound energy reflectors, presser rolls, which are placed at well known distances, calculated considering the forming mechanism of a standing stationary wave system in the tube. The analysis of the “ultrasounds surface effect” is made depending on the relative drawing velocity, v_{tr} / \bar{v}_v , (v_{tr} -rate of drawing, \bar{v}_v -vibratory rate of the die). The rate of drawing defines the technological efficiency and the vibratory rate of the die, ($\bar{v}_v = 2\pi \cdot f \cdot A$) and gives enough information about the ultrasound equipment used for the generation and the transference of ultrasound energy by f and A parameters.

Also, based on the resonant frequency, (f), it will realize the dimensioning of the ultrasound energy concentrators, in $\lambda/2$, ($\lambda=c / f$). The tubes without inside guard drawing processes, in SONODRAW system, will be used for the processing of the tubes with thin walls, made from cold drawing hard malleable metallic materials / work hardenable, (a small dying-out of the ultrasounds into the metal mass), in the next condition: $v_{tr} / \bar{v}_v \ll 1,0$, the safety of the drawing being more better then in the clasical technology-TC case.

A c k n o w l e d g e m e n t. This paper was realised with the support of EURODOC “Doctoral Scholarships for research performance at European level” project, financed by the European Social Found and Romanian Government.

Received: May 14, 2010

* “Gheorghe Asachi” Technical University of Iași,
e-mail: bgdnlcn@yahoo.com

** Institute of Applied Phisics of Sciences of Moldova

*** S.C. Cablero S.R.L

REFERENCES

1. Cazimirovici, E., *et al.*, *Teoria și tehnologia deformării prin tragere*. Edit. Tehnică, București, 1990.
2. Susan M., *Deformarea metalelor prin tragere. Elemente de teoria și tehnologia tragerii sârmelor, barelor și țevelor*. Edit. Tehnopress, Iași, 2002.
3. Severdenko V.P., *Prokatka i volocenie c ultrazvukom*, NAUKA I Tehnică, Minsk, 2002.
4. Dragan O., *et al.*, *Ultrasunete de mari energii*. Edit. Academiei, 1983.
5. Brown B., *et al.*, *High-Intensity Ultrasonic. Industrial Applications*. HLIFFE BOOKS, London, 2004.
6. Susan M., *Tragerea metalelor cu vibrații ultrasonice*. Edit. Cerami, Iași, 2007.
7. Susan M., Bujoreanu L. G., *The Metal-Tool Contact Friction at the Ultrasonic Vibration Drawing of Ball-Bearings Steel Wires*. Rev. Metalurgia de Madrid, Spain, **35**, 6, 379-383 (1999).

ANALIZA EFECTULUI DE SUPRAFAȚĂ AL ULTRASUNETELOR LA TRAGEREA ȚEVELOR ÎN SISTEM SONODRAW

(Rezumat)

În lucrare, pe lângă definirea și explicitarea “efectului de suprafață al ultrasunetelor” sau de “reducere a frecării de contact metal-sculă”, la tragerea țevelor fără ghidaj interior, se face și analiza tehnologică a acestuia pe baza “vitezei relative de tragere, (v_{tr}/\bar{v}_v) ”, v_{tr} -viteza de tragere care definește productivitatea tehnologică și v_v -viteza de vibrație a filierei, $\bar{v}_v = 2\pi \cdot f \cdot A$, care prezintă suficiente informații despre echipamentul ultrasonic de producere și transfer a energiei ultrasonice. Tragerea țevelor fără ghidaj interior în sistem SONODRAW se recomandă pentru procesarea țevelor din materiale metalice greu deformabile prin tragere la rece/puternic ecruisabile, cu pereți subțiri, pentru care este îndeplinită condiția: $v_{tr}/\bar{v}_v \ll 1$.

WATER TEMPERATURE INFLUENCE ON METALLIC MATERIALS COOLING

BY

ADRIAN GRECU, DAN-GELU GĂLUȘCĂ, CARMEN NEJNERU
and NICANOR CIMPOEȘU

Abstract. Water properties are from a long time discussed by different points of view by metallurgical interest in heat treatment area an important subject is water temperature influence on samples properties for different heat treatments that need relative fast cooling. Cooling curves and rates and thermal transfer coefficient were determined using a start temperature of the metallic material of 800°C and as medium water at 60 and 65°C.

Key words: water cooling, thermal transfer coefficient.

1. Introduction

Quenching is the act of rapidly cooling the hot steel to harden the steel.

Water quenching can be done by plunging the hot steel in water. The water adjacent to the hot steel vaporizes, and there is no direct contact of the water with the steel. This slows down cooling until the bubbles break and allow water contact with the hot steel. As the water contacts and boils, a great amount of heat is removed from the steel. With good agitation, bubbles can be prevented from sticking to the steel, and thereby prevent soft spots.

Water is a good rapid quenching medium, provided good agitation is done. However, water is corrosive with steel, and the rapid cooling can sometimes cause distortion or cracking.

Salt water is a more rapid quench medium than plain water because the bubbles are broken easily and allow for rapid cooling of the part. However, salt water is even more corrosive than plain water, and hence must be rinsed off immediately.

Oil is used when a slower cooling rate is desired. Since oil has a very high boiling point, the transition from start of martensite formation to the finish is slow and this reduces the likelihood of cracking. Oil quenching results in fumes, spills, and sometimes a fire hazard.

Polymer quenches that will produce a cooling rate in between water and oil. The cooling rate can be altered by varying the components in the mixture-as these are composed of water and some glycol polymers. Polymer quenches are capable of producing repeatable results with less corrosion than water and less of a fire hazard than oil. But, these repeatable results are possible only with constant monitoring of the chemistry.

Cryogenics or deep freezing is done to make sure there is no retained Austenite during quenching. The amount of martensite formed at quenching is a function of the lowest temperature encountered. At any given temperature of quenching there is a certain amount of martensite and the balance is untransformed Austenite. This untransformed Austenite is very brittle and can cause loss of strength or hardness, dimensional instability, or cracking.

Quenches are usually done to room temperature. Most medium carbon steels and low alloy steels undergo transformation to 100% martensite at room temperature. However, high carbon and high alloy steels have retained Austenite at room temperature. To eliminate retained Austenite, the quench temperature has to be lowered. This is the reason to use cryogenic quenching.

Water has some amazing properties. It is the only natural substance found in all three states — solid, liquid and gas — within the range of natural Earth temperatures. Its solid form is less dense than its liquid form, which is why ice floats. It can absorb a great deal of heat without getting hot, has very high surface tension (helping it move through roots and capillaries — vital to maintaining life on Earth) and is virtually incompressible.

In this paper we analyze a metallic material behavior heated at 800°C and fast cooled in water, varying the water temperature.

2. Experimental Results

Main objective of this study is to analyze the behavior of the material in contact with water from the very first moment.

In Table 1 are present the process parameters that express the temperature variation in time, and the heat transfer coefficient values function of time and temperature.

Interesting at the entire process are the first three stages, especially the calefaction and the boiling stages and in the end the last one the convection phase.

The cooling rate increase until 29.33°C/s at 200°C, corresponding to boiling finish period and decreasing after that until 0.67°C/s at 70°C.

Table 1
Temperature Variation and Other Process Factors at Cooling in 60°C Water

Ta=60°C	H [m ⁻¹]= 0.228								
T [°C]	800	700	600	500	400	300	200	100	70
t [s]	0	13.35	19.42	26.09	32.4	37.51	40.92	84.3	129
Δt	0	13.35	6.07	6.67	6.31	5.11	3.41	43.38	44.7
V=ΔT/Δt	0	7.49	16.47	14.99	15.8	19.57	29.33	2.31	0.67
α [kcal/m ² h grd]	0	62.13	159.91	175.4	233.4	389.4	903.0	164.9	177.1

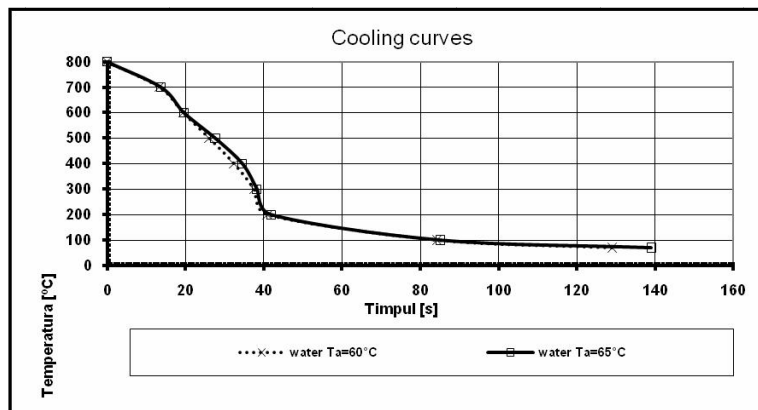


Fig. 1 – Cooling curves of a metallic material in water at 60° and 65°C.

Because of the medium temperature the sample – water temperature transfer occurs for a longer time than other environments but is ideal for sensible sample were cracks can appear and damage the sample.

Fig. 2 present visual the cooling stages with calefaction in *a* represented by a gas protector bubble, in *b* the broken bubble representing the boiling and in *c* the cooled sample in convection range.

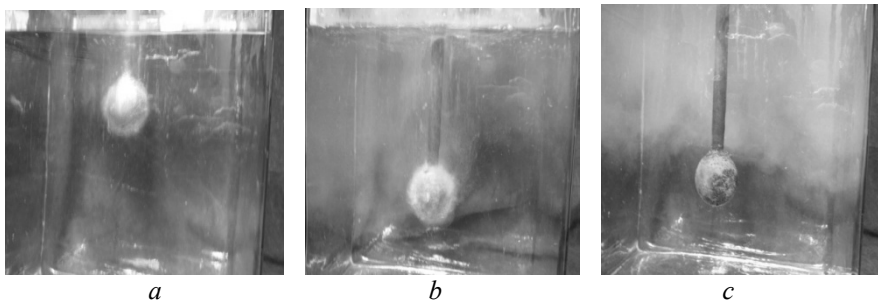


Fig. 2 – Experimental images of a metallic material cooling: *a* – calefaction; *b* – boiling; *c* – convection.

Concerning the cooling rates both mediums behave similar at least for calefaction period, were are identical, and boiling were appear for water at 65°C some variations in transition from calefaction and boiling represented by a decrease of the cooling rate more evident than the material behavior in water at 60°C.

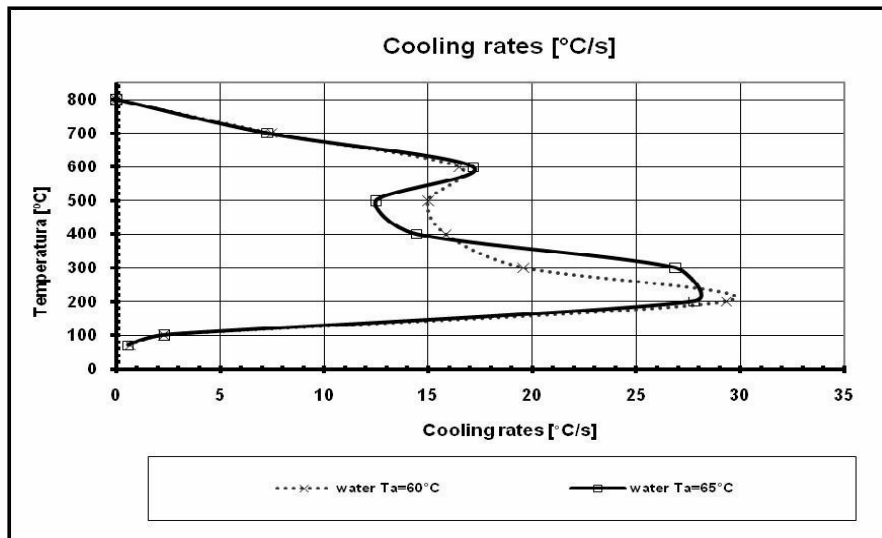


Fig. 3 – Cooling rates variation with temperature for medium temperature 60° and 65°C.

In table are presented most important parameter of cooling in water at 65°C, starting from 800°C decreasing with 100°C until 100°C and after to 70°C. Normally the time of each period increase at the beginning with half of the first period time, almost became equal in 400 – 300°C range, corresponding to boiling period and increase exponentially at entire cooling period.

Table 2

Temperature Variation and Other Process Factors at Cooling in 65°C Water

Ta=65 °C	H [m ⁻¹]= 0.245								
T [°C]	800	700	600	500	400	300	200	100	70
t [s]	0	13.76	19.59	27.6	34.52	38.24	41.84	85.16	139
Δt	0	13.76	5.83	8.01	6.92	3.72	3.6	43.32	53.84
V=ΔT/Δt	0	7.27	17.15	12.48	14.45	26.88	27.78	2.31	0.56
α [kcal/m ² h gd]	0	60.72	167.9	147.5	215.6	544.49	879.65	178.03	206.48

The cooling rate increase until the boiling period finished, around 300°C, reaching a 26,88°C/s rate and decrease until 0.56°C/s at the medium temperature.

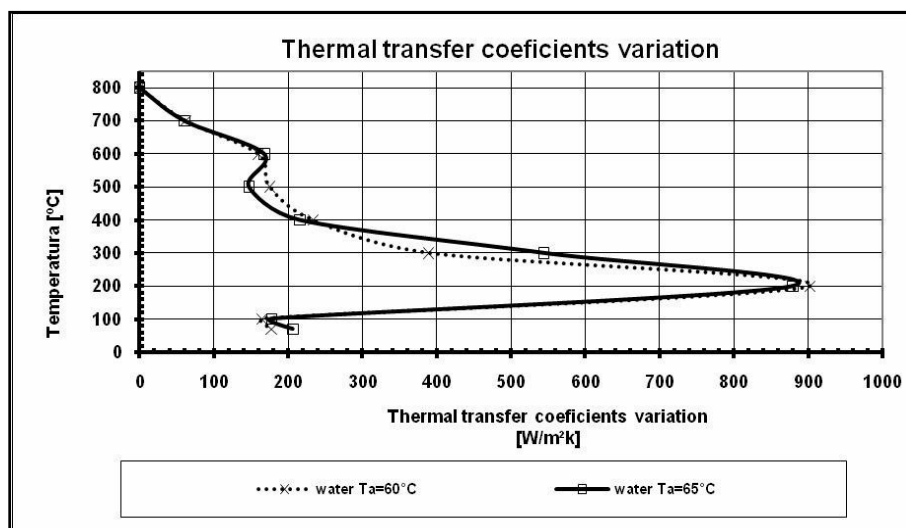


Fig. 4 – Thermal transfer coefficients variation with temperature.

In calefaction period the thermal transfer coefficient, in water at 65°C, decrease around 100 W/m²k and after the break through to boiling increasing passing even the similar coefficient of water at 60°C.

3. Conclusion

- Considering the water as cooling medium for heat treatments can be used at different temperatures considering the purpose of the treatment and the sample state.
- Comparing the warmed water at 60 or 65°C in the first medium the sample reach a cooling rate of 29,33/s at 200°C and the second 26,88°C/s at the 300°C, both with decreasing temperature after this until 2 maybe 1°C/s, enlarging the domain of samples that are sensible in different temperature range.
- All cooling states, calefaction, boiling or convection have a relatively big deployment period considered good for sensitive samples.

Received: May 14, 2010

“Gheorghe Asachi” Technical University of Iași,
Department of Materials Science
e-mail: greuceanu24@yahoo.com

REFERENCES

1. Nejnereu C., Gălușcă D.G., Grecu A., Perju M., Hopulele I., *Researches Concerning Variation of Cooling Intensity of the Synthetical Mediums Like Polialchilenglicol (PAG) 5% Solution in Water Modified by Adding 16% Na₂SiO₄ and CaCO₃ (5%, 10%, 15%)*. Bul. Inst. Polit., Iași, **LIII (LVII)**, 3, s. Materials Science and Engineering, 197-202 (2007).
2. Nejnereu C., Grecu A., Carabet R., Hopulele I., *Researches Concerning the Reconditioning of Hardening Bathes in Synthetic Medium Based on Carbodimethyl Cellulose*. Vol. **II** "Tehnologii și materiale avansate", Galați, 318-324 (2007).
3. Nejnereu C., Gălușcă D.G., Grecu A., Carabet R., *Researches Looking the Modification Cooling Capacity of Hardening Compounds in Magnetic Field*. Vol. **II** "Tehnologii și materiale avansate", Galați, 161-165 (2007).
4. Gălușcă D.G., Nejnereu C., Grecu A., Carabet R.G., *Researches Concerning Cooling Capacity of Heterogeneous Mediums Type Air-Fog Used in Heat Treatment of the Cast Pieces with Big Dimensions*. Conf. Artcast, Galați, 192 (2008).

INFLUENȚA TEMPERATURII APEI ASUPRA RĂCIRII MATERIALELOR

(Rezumat)

Proprietățile apei sunt de mult timp discutate din diferite puncte de vedere, în domeniul metalurgiei, în special domeniul tratamentelor termice, un subiect important este influența temperaturii apei asupra proprietăților probelor pentru diferite tratamente termice ce necesită o răcire relativă rapidă. Curbele și vitezele de răcire cât și coeficientul de transfer termic au fost determinate folosind o temperatură de pornire, a materialului metalic, de 800°C și ca mediu de răcire apa la 60° și 65°C.

SOME CONSIDERATIONS CONCERNING THE HARDENING AND FINISHING PROCEEDING WITH ULTRASONIC VIBRATIONS

BY

**BRIAN-TUDOR C. LANDKAMMER, BOGDAN GAVRILĂ, MIHAI SUSAN
and CONSTANTIN BACIU**

Abstract. This paper presents some technological considerations about the building and the efficiency of oscillating systems for the hardening and finishing with ultrasonic vibrations of metallic pieces.

Key words: hardening, finishing, ultrasonic, oscillating system, efficiency criterions.

1. Introduction

The hardening and finishing proceeding of the superficial layer by plastic deformation in a cool with ultrasonic vibrations applied on the active element (ball or roll), in the head of metallic surfaces having a flat or a cylindrical symmetry, take part from the mechanical treatment category [1],..., [3].

The mechanical treatments are the oldest hardening and finishing proceedings of the superficial layers. Less known than thermal treatments and thermo chemical treatments, they are, at this moment an advantageous alternative available to each mechanical processing department or workshop.

The hardening of the superficial layer is explained by accumulated hammer hardening during the plastic deformation in a cool basing on dislocation theory.

The hardening and finishing superficial layer through plastic deformation in a cool of metals with ultrasonic vibrations - DPS (a recognized symbol for superficial plastic deformation), leads to structural modifications and

physical - mechanical proprieties modifications for the products processed in that way, concomitantly with a finishing or an improvement of the surface quality [1],..., [3].

A classification of hardening and finishing proceedings through plastic deformation of superficial layers / DPS is presented in Fig. 1, [2].

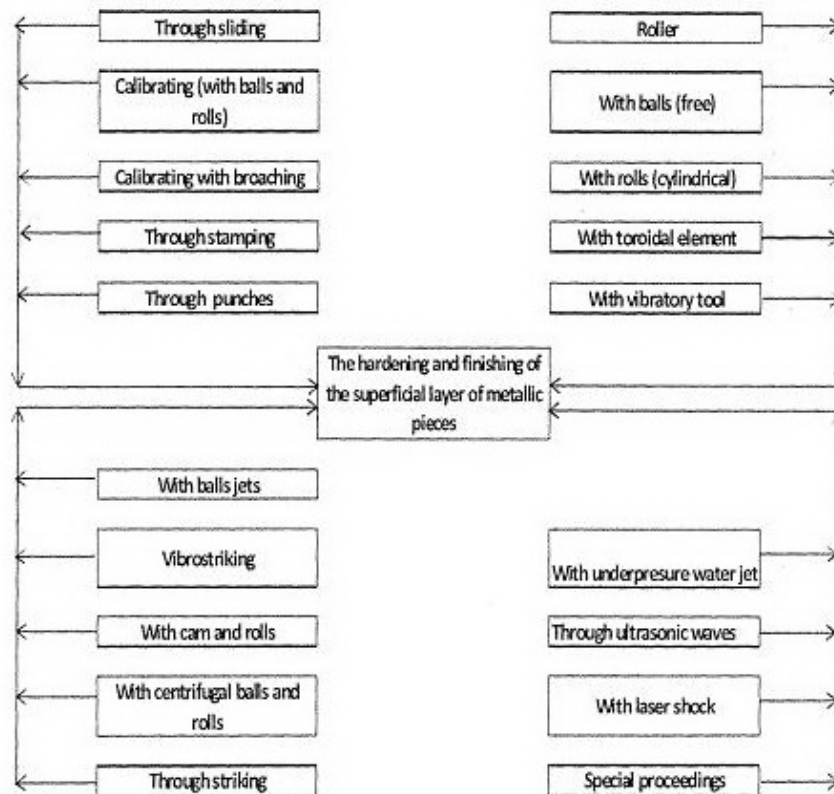


Fig. 1 – The classification of hardening and finishing proceedings through plastic deformation of superficial layers/DPS [2].

2. The Characterization of Proceeded Layer Through DPS

➤ *The surfaces situation* of a metallic piece by DPS is definite by STAS 5730, which expresses [2].

✓ The geometrical situation through geometrical deviation of real surfaces of pieces, as against with that is already geometrical defined one with a technical documentation of the execution.

✓ The physico-chemical condition, through physic-chemical characteristics of the superficial layer for the respective piece.

➤ *The stress situation of a metallic piece* processed through DPS, can be [6].

✓ Simple, when the steering tensors σ and τ of unit stresses keep constant values in each point of the piece body.

✓ Complex, when the steering tensors of the stresses are changing their values.

The relation between the units stresses components and deformation components over the elasticity limit are established by plasticity theories:

a. *Plastic deformation theory*, which formulates direct relations between stresses and deformations;

b. *Plastic flowing theory*, which formulates relations between velocities or deformations increases and increases of stresses.

Iliusin has demonstrated that in the simple charge case (linear level of stresses, the deformational type theories and flowing theories are the same, existing an unique theory of the plasticity - the theory of little elastic deformation (Henckly – Iliusin), available also in DPS in a cool.

➤ As a result of elastic and plastic deformations that took place during the DPS processing, in metal mass it is created, simultaneously or successive, a supplementary stresses situation (residual) which remain in the deformed piece body and which generate linear modifications or volumetrically modifications un uniform residual [5], ..., [7].

These residual stresses are classified in two or three groups as:

✓ Stresses of the first class (1-st), which is coming in equilibrium in the macro volumes of piece and has an oriented direction.

✓ Stresses of the second class, which is coming in equilibrium in the limits of little volumes (measurable with grain dimensions) and has no determinate direction.

✓ Stresses of the third class, which appear at each crystal level of the net (micro stresses limited at some atoms).

On a certain deep of the plastic buckled layer, the axial residual and tangent stresses have the same variation law, passing from negative values (compression) to positive values (extension) and approximately to initial status which exists in the other part of the mass metal.

➤ The processed layer structure has a fibrous character, as a result of DPS processing and it is good to coincide with the fibrous that the piece must have.

➤ It is occurred an increasing of dislocation densities and of internal energy.

➤ The superficial hardness layer of the piece, depending on the material quality and situation and working conditions, can increase to 100% compared to initial hardness.

➤ The initial roughness of the piece can be improved by 3 to 40 times, depending on the piece material and the hardening conditions. The wearing

behavior is improved taking into account that it directly depends on the hardness and roughness of the surfaces.

The essential effect of plastic deformation in a cold place is the formation of compressed residual stresses that determinate a considerable increasing of the weariness strength.

As a result of plastic deformation it is definite as nominal pressure in MN on a one meter square capable to deform the superficial layer with a micron.

The plastic deformation in a cold place/DPS improves sensitive the corrosion resistance. They are modifying the physical proprieties: the electric resistivity increases, the magnetic permeability decreases), [2].

3. Building Elements of the Oscillatory System

The scheme of a hardening and finishing installation with ultrasonic vibrations has, as a rule.

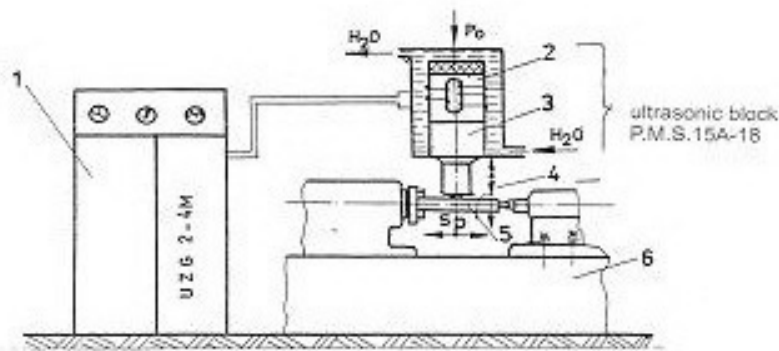


Fig. 2 – The scheme of a hardening and finishing installation with ultrasonic vibrations (7): 1 – ultrasonic generator; 2 – magnetostrictive transducer; 3 – cylindrical concentrator in steps; 4 – contact element-steel ball; 5 – piece for processing; 6 – leithe body; P_0 – pressing strength; S_p – piece advance.

For successful results of the hardening and finishing process with ultrasonic vibrations we used lengthwise ultrasonic waves in stationary waves regime – with knot forming centers of wave's oscillation [5], [7], [10].

The ultrasounds generation is, in fact, a high frequency generator. The high frequency is transformed in oscillations/displacements, on the base of a specific effect of the magnetostrictive transducer, on the scheme from Fig. 2, magnified through the cylindrical concentrator in steps. These oscillations/displacements (for example at 20000 Hz there are 20000 makings and remakings of the contact) are transmitted to the steel ball which comes in contact with the piece for processing through a beating/kicking effect.

In Fig. 3 there is, for example, the scheme of oscillating system and the wave's displacement, [5], [7], [10].

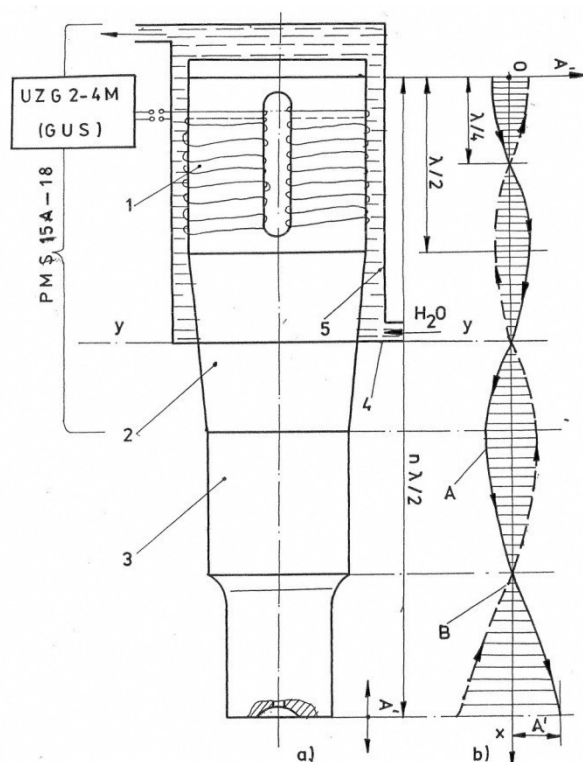


Fig. 3 – The scheme of oscillating system and the waves oscillation: *a* – the properly construction; *b* – the waves oscillation: 1 – magnetostrictive transducer; 2 – conic concentrator; 3 – cylindrical concentrator in work steps; 4 – crucial flange; 5 – carcass: *A* – progressive wave; *B* – regressive wave; *A'* – the amplitude of waves oscillation.

The dimensioning of oscillating system is realized in $\lambda/2$, where *n* is the number of knots and λ is the wave length. The wave length can be determinate with the relation:

$$(1) \quad \lambda = \frac{c}{f}$$

where: *c* – is propagation velocity of the waves in the respective environment ($c_{\text{steel}}=5050\text{m/s}$); *f* – resonance frequency of the oscillating system (magnetostrictive transducer $f_{\text{resonance}} = 20000 \div 22000\text{Hz}$; $f=1/T$, where *T* is oscillation period.

As an estimation criterion of the efficiency of hardening and finishing process with ultrasonic vibrations they are using these notions: “ultrasonic finishing degree” and “ultrasonic hardening degree” defined with the relations [8], [9]:

$$(2) \quad G_{Ra} = (Ra^0 - Ra^{vs}) \cdot 100 [\%]$$

and

$$(3) \quad G_{Hv} = (Hv^{vs} - Hv^0) \cdot 100 [\%]$$

where Ra^0 and Ra^{vs} the parameters of (Ra) - with and without ultrasonic waves; Hv^{vs} and Hv^0 hardening parameters with and without waves.

The reported results by researchers in this domain demonstrate a better efficiency of the hardening and finishing process, as against with classic processes.

4. Applications at a Industrial Level

The applications at an industrial level, for hardening and finishing proceeding with ultrasonic waves, can be realized with success, especially for pieces with cylindrical symmetry in aeronautical, automobiles and nautical industries. Numerous researches were done in the last few years on stainless steels.

5. Conclusions

This paper presents some technological considerations, regarding the construction and the dimensioning of oscillating system and regarding the efficiency of the hardening and

Finishing proceeding with ultrasonic waves. For a better efficiency it is recommended the using of lengthwise waves in working conditions with stationary waves with the knots and centers formation. The dimensioning of oscillating system must be realized in $\lambda/2$. As main assessment criterion of the hardening and finishing process efficiency, process with ultrasonic waves, they are used these notions: “ultrasonic finishing degree” and ultrasonic hardening degree.

A c k n o w l e d g e m e n t. This paper was realised with the support of EURODOC “Doctoral Scholarships for research performance at European level” project, financed by the European Social Found and Romanian Government.

Received: May 14, 2010

*“Gheorghe Asachi” Technical University of Iași,
Department of Materials Science
email: tudor_brian@yahoo.com*

R E F E R E N C E S

1. Gavrilaş I., Maier A., *Netezirea și ecruisarea suprafețelor prin rulare, alunecare și lovire*. Edit. Tehnică, București, 1972.
2. Vermesan H. *et al.*, *Introducere în ingineria suprafețelor*. Edit. Dacia, Cluj-Napoca, 1999.
3. Lupescu O., *Cercetări privind tratamentul mecanic prin rulare și influența lui asupra durificării și calității suprafețelor cilindrice exterioare*. Ph. D. Diss., “Gheorghe Asachi” Technical University of Iași, 1998.
4. Baciuc C. *et al.*, *Știința materialelor metalice*. Edit. Did. și Pedag., București, 1990.
5. Abramov O.V., *Abrabotka materialov*. 2000.
6. Susan M. *et al.*, *Prelucrări plastice speciale*. Edit. “Gh. Asachi”, Iași, 2000.
7. Amza Gh., *Contribuții la studiul fenomenelor de deformare plastică în câmp ultrasonor*. Ph. D. Diss., Inst. Polit. București, 1979.
8. Romanescu I., *Cercetări privind utilizarea vibrațiilor de frecvență înaltă la așchieria metalelor*. Ph. D. Diss., “Gheorghe Asachi” Technical University of Iași, 2000.
9. Susan M., *Tragerea metalelor cu vibrații ultrasonice*. Edit., Ceram, Iași, 2007.

UNELE CONSIDERAȚII ASUPRA PROCEDEULUI DE DURIFICARE ȘI
FINISARE CU VIBRAȚII ULTRASONICE

(Rezumat)

În lucrare sunt prezentate câteva considerații tehnologice despre eficiența fabricării sistemelor oscilante pentru durificarea și finisarea cu vibrații ultrasonice a semifabricatelor metalice.

BULETINUL INSTITUTULUI POLITEHNIC DIN IAȘI
Publicat de
Universitatea Tehnică „Gheorghe Asachi” din Iași
Tomul LVI (LX), Fasc. 3, 2010
Secția
ȘTIINȚA ȘI INGINERIA MATERIALELOR

ON THE MOMENTUM TRANSPORT IN THE FRACTAL MATERIALS

BY

RĂZVAN IULIAN LIȚOIU, ANCA ELENA LĂRGEANU
and IOANNIS ZERICHIOTIS

Abstract. Using the Scale Relativity Theory the momentum transport in fractal materials is analyzed. Two type momentum transport are distinguished by means of non-autonomous structures, or through of quasi-autonomous structures.

Key words: fractal materials, momentum transport, autonomous structures

1. Introduction

The theoretical description of microphysical systems is based on the wave mechanics of Schrödinger [1], the matrix mechanics of Heisenberg [2], or the path-integral mechanics of Feynman [3]. Another approach is the hydrodynamic formulation of quantum mechanics due to Madelung [4], de Broglie [5], Takabayasi [6] and Bohm [7] (idea of ‘subquantum medium’). The hydrodynamic theory of quantum mechanics has been later extended by de Broglie (idea of the ‘double solution’) [8], [9].

The theory of scale relativity (SR) is build by completing the standard laws of classical physics (motion in space-time) by new scale laws (in which “the space-time resolutions are used as intrinsic variables, playing for scale transformations the same role as played by velocities for motion transformations” [10],..., [12]). This model is based both on the fractal space-time concept, that is also introduced by Ord [13] and El Naschie [14] and “on a generalization of Einstein’s principle of relativity to scale transformations. The space-time resolutions are redefined as characterizing the state of scale of reference systems, in the same way as velocity characterizes their state of

motion. Then, one requires that the laws of physics apply for any state of the reference system, of motion (principle of motion-relativity) and of scale (principle of scale-relativity). Mathematically, the principle of SR is achieved by the principle of scale-covariance, requiring that the equations of physics to keep their simplest form under transformations of resolution" [10-12].

Three scales of interaction of SRT were developed: (i) A 'Galileian' version corresponding to the standard fractals with constant fractal dimensions [15] and which involves quantum mechanics [10-12]; (ii) A special scale-relativistic version which implies the high energy physics [10-12,16]; (iii) A 'general scale-relativistic' version which implies the cosmology [10-12,17].

In the present paper, using SRT the transport momentum in materials is analyzed.

2. Mathematical Model

In the Nottale's model of SRT it is supposed that the motion of "micro particles" takes place on fractal (continuous but non-differentiable) curves of fractal dimension $D_F=3$. A manifold compatible with such motion was called fractal space-time. The fractal nature of space-time implied, through non-differentiability, the substitution of the standard time derivative d/dt by the complex operator $\hat{\partial}/\partial t$.

$$(1a) \quad \frac{\hat{\partial}}{\partial t} = \frac{\partial}{\partial t} + \mathbf{V} \cdot \nabla + D \nabla^3$$

where

$$(1b) \quad \mathbf{V} = \mathbf{v} - i\mathbf{u}$$

is the complex speed field, D the fractal-non-fractal transition coefficient and

$$(1c) \quad \nabla^3 = \frac{\partial^3}{\partial x^3} + \frac{\partial^3}{\partial y^3} + \frac{\partial^3}{\partial z^3}$$

In these conditions the microparticle movements are described by the second Newton's laws

$$(1d) \quad \frac{\hat{\partial} \mathbf{V}}{\partial t} = \frac{\partial \mathbf{V}}{\partial t} + \mathbf{V} \cdot \nabla \mathbf{V} + D \nabla^3 \mathbf{V} = 0$$

The means that in the fractal space-time the local acceleration, $\partial \mathbf{V} / \partial t$, the convective effects, $\mathbf{V} \cdot \nabla \mathbf{V}$ and dispersive ones, $\nabla^3 \mathbf{V}$, are reciprocally compensating at any scales.

By substituting (1b) in equation (1d), and separating the real and the imaginary parts, we obtain the following system:

$$(2a,b) \quad \begin{aligned} \frac{\partial \mathbf{v}}{\partial t} + \nabla \left(\frac{\mathbf{v}^2}{2} - \frac{\mathbf{u}^2}{2} \right) + D \nabla^3 \mathbf{v} &= 0 \\ \frac{\partial \mathbf{u}}{\partial t} + \nabla (\mathbf{v} \cdot \mathbf{u}) + D \nabla^3 \mathbf{u} &= 0 \end{aligned}$$

In the one-dimensional differentiable case, for $\mathbf{u} = 0$ or $\rho = const.$, using the dimensionless parameters,

$$(3) \quad \bar{\phi} = (v/v_0), \quad \bar{\tau} = \omega_0 t, \quad \bar{\xi} = k_0 X$$

and the normalizing condition

$$(4) \quad \frac{v_0 k_0}{6 \omega_0} = D \frac{k_0^3}{w_0} = 1$$

the equations (2a,b), takes the standard form [18],

$$(5) \quad \partial_{\bar{\tau}} \bar{\phi} + 6 \bar{\phi} \partial_{\bar{\xi}} \bar{\phi} + \partial_{\bar{\xi} \bar{\xi} \bar{\xi}} \bar{\phi} = 0$$

Through the substitutions,

$$(6a,b) \quad w(\theta) = \bar{\phi}(\bar{\xi}, \bar{\tau}), \quad \theta = \bar{\xi} - v_f \bar{\tau}$$

equation (5), by double integration, becomes

$$(7) \quad \frac{1}{2} w'^2 = F(w) = -(w^3 - \frac{v_f}{2} w^2 - gw - h)$$

with g, h two integration constants. If $F(w)$ has real roots, they are of the form [19]

$$(8) \quad e_1 = \bar{w} + 2a \left[\frac{E(s)}{K(s)} - \frac{1}{s^2} \right], \quad e_2 = \bar{w} + 2a \left[\frac{E(s)}{K(s)} - 1 \right], \quad e_3 = \bar{w} + 2a \frac{E(s)}{K(s)}$$

with

$$(9) \quad a = \frac{e_3 - e_2}{2}, \quad s^2 = \frac{e_3 - e_2}{e_3 - e_1}, \quad K(s) = \int_0^{\pi/2} (1 - s^2 \sin^2 \varphi)^{-1/2} d\varphi,$$

$$E(s) = \int_0^{\pi/2} (1 - s^2 \sin^2 \varphi)^{1/2} d\varphi$$

\bar{w} a reference value and $K(s)$, $E(s)$ the complete elliptic integrals of s modulus [19]. The stationary solution of equation (5) has the expression,

$$(10) \quad \bar{\phi}(\bar{\xi}, \bar{\tau}) = \bar{w} + 2a \left(\frac{E(s)}{K(s)} - 1 \right) - 2a \cdot cn^2 \left\{ \frac{\sqrt{a}}{s} \left[\bar{\xi} - \left(6\bar{w} + 4a \left(\frac{3E(s)}{K(s)} - \frac{1+s^2}{s^2} \right) \right) \bar{\tau} + \bar{\xi}_0 \right]; s \right\}$$

where cn is the Jacobi's elliptic function of s modulus [19] and $\bar{\xi}_0$ an integration constant. As a result, the one-dimensional oscillation modes of the speed field are of cnoidal type [19] – and have the normalized wave length,

$$(11) \quad \lambda = 2sK(s)/\sqrt{a}$$

- the normalized phase speed,

$$(12) \quad v_f = 6\bar{w} + 4a \left[3(E(s)/K(s)) - \left((1+s^2)/s^2 \right) \right]$$

- and the normalized group speed,

$$(13) \quad v_g = 6\bar{w} + 4a \left[3 \frac{E(s)}{K(s)} - 1 - \frac{1}{s^2} + 3 \frac{E^2(s) + 2(s-1)E(s)K(s) - (s-1)K^2(s)}{E(s)K(s) + K^2(s) - sK^2(s)} + \frac{2(s-1)K(s)}{s^2[E(s) + K(s) - sK(s)]} \right]$$

Then, the followings result: (i) Through the D coefficient, the parameter s becomes a ‘measure’ of ‘charge’ transport type in the considered matter. Thus, the solution (10), for $s = 0$, is reduced to one-dimensional harmonic waves, and for $s \rightarrow 0$ to one-dimensional waves packet.

These two subsequences describe the ‘charge’ transport in a non-quasi-autonomous regime [18]. For $s = 1$, the solution (10) becomes an one-dimensional soliton [18], while for $s \rightarrow 1$ one dimensional solitons packet results. These last two subsequences describe ‘charge’ transport in a quasi-

autonomous regime [18]; (ii) By eliminating the parameter a from relations (11) and (13), one obtains:

$$(14) \quad (v_f - 6\bar{w})\lambda^2 = A(s),$$

$$A(s) = 16 \left[3s^2 E(s)K(s) - (1 + s^2)K^2(s) \right]$$

We observe that for $s = 0 \div 0.7$, $A(s) \approx \text{const.}$ and consequently equation (14) takes the form, $(v_f - 6\bar{w})\lambda^2 = \text{const.}$. Therefore, in the differentiable case, the ‘charge’ transport is controlled through the flowing regimes of the fractal fluid, and the separation between them is given by the 0.7 value of the parameter s ; (iii) The previous results show through the normalized group speed (13) an increase of the ‘charge’ transport by means of quasi-autonomous structures. This theoretical result explain some “anomalies” that were experimentally observed in nanostructures, *e.g.* the increase of the thermal conductance in nanofluids [20], [21] etc.

3. Conclusion

The main conclusions of the present paper are as follows:

i) Using the mathematical formalism of the scale relativity theory, the momentum transport in materials is analyzed;

ii) It results, through an equation of motion for the complex speed field, that in a fractal fluid, the local acceleration, the convection, and the dispersion are reciprocally compensating at any scale (differentiable or non-differentiable).

iii) At differentiable scale, the ‘charge’ transport is achieved by one-dimensional cnoidal oscillation modes of the speed field. For different degrees of the ‘charge’ coupling, the one-dimensional cnoidal speed oscillation modes contain the one-dimensional speed harmonic waves, the one-dimensional speed wave’s packet, the one dimensional speed solitons packet and the one dimensional speed soliton. The first two subsequences describe the non-autonomous regime of the ‘charge’ transport, while the last ones describe the quasi-autonomous regime of the ‘charge’ transport. In the non-autonomous regime, a relation between the normalized wave length and the normalized phase speed, *i.e.* a dispersion type relation, is obtained. These two regimes are separated by “0.7 structure” that is experimentally observed for various nanostructures. These results are in according with those obtained in [22],..., [27].

A c k n o w l e d g e m e n t. This paper was realised with the support of BRAIN “Doctoral scholarships as an investment in intelligence” project, financed by the European Social Found and Romanian Government.

Received: May 14, 2010

“Gheorghe Asachi” Technical University of Iași,
e-mail: razvan_cel_cam_bun@yahoo.com

REFERENCES

1. Schrodinger E, *Collected Papers on Wave Mechanics*. W.M. Deans, London, 1928.
2. Green H.S., *Matrix Mechanics*. P. Noordhoff Ltd., Groningen, 1965.
3. Feynman R.P., Hibbs A.R., *Quantum Mechanics and Path Integrals*. McGraw-Hill, New York, 1965.
4. Madelung E., *Z. Physik*, **40**, 322 (1926).
5. De Broglie L., *Compt. Rend.*, **185**, 380 (1927).
6. Takabayasi T., *Progr. Theor. Phys.*, Kyoto, **8**, 143 (1952).
7. Bohm D., *Phys. Rev.* **85**, 66 (1952).
8. De Broglie L., *Compt. Rend.*, **264**, 1041 (1967).
9. Bohm D., Bub J., *Rev. Mod. Phys.*, **38**, 453 (1966).
10. Nottale L., *Fractal Space-Time and Microphysics: Towards a Theory of Scale Relativity*. World Sci., Singapore, 1993.
11. Nottale L., *Int. J. Mod. Phys.*, **A7**, 4899 (1992).
12. Nottale L., Célérier M.N., *J. Phys. A: Math. Theor.*, **40**, 14471 (2007).
13. Ord G.N., *J. Phys.*, **A**, **16**, 1869 (1983).
14. El Naschie M.S., Rösler O.E., Prigogine I (Eds.), *Quantum Mechanics, Diffusion and Chaotic Fractals*. Elsevier, Oxford, 1995.
15. Madelbrot B., *The Fractal Geometry of Nature*. Freeman, San Francisco, 1982.
16. Nottale L., Célérier M.N., Lehner T., *J. Math. Phys.*, **47**, 032303, (2006).
17. Célérier M.N., Nottale L., *J. Phys. A: Math. Gen.*, **3**, 931 (2004).
18. Jackson E.A., *Perspectives in Nonlinear Dynamics*. Vol. **I-II**, Cambridge Univ. Press, Cambridge, 1991.
19. Bowman F., *Introduction to Elliptic Function with Applications*. English Univ. Press, London, 1955.
20. Imry Y., *Introduction to Mesoscopic Physics*. Oxford Univ. Press, Oxford, 2002.
21. Ferry D.K., Goodnick S.M., *Transport in Nanostructures*. Cambridge Univ. Press, Cambridge, 1997.
22. Agop M., Ioannou P.D., Nica P., *J. Math. Phys.*, **46**, 062110 (2005).
23. Agop M., Nica P., Girtu M., *Gen. Relativ. Gravit.*, **40**, 35-55 (2008).
24. Agop M., Nica P., Ioannou P.D., Malandrak I.O., Gavanas-Pahomi I., *Chaos, Solitons and Fractals*. **34**, 1704 (2007).
25. Gottlieb I., Agop M., Ciobanu G., Stroe A., *Chaos, Solitons and Fractals*. **30**, 380 (2006).
26. Agop M., Ioannou P.D., Nica P., *J. Math. Phys.*, **46**, 062110 (2005).
27. Agop M., Nica P.E., Ioannou P.D., Antici A., Paun V.P., *Eur. Phys. J.*, **D 49**, 239–248 (2008).

TRANSPORTUL DE IMPULS ÎN MATERIALELE FRACTALE

(Rezumat)

În lucrarea de față este analizat transportul de impuls în materialele fractale utilizând teoria relativității de scală. Se disting două tipuri de transport de impuls, unul prin intermediul structurilor non-autonome, iar celălalt prin intermediul structurilor cvasi-autonome.

BULETINUL INSTITUTULUI POLITEHNIC DIN IAȘI
Publicat de
Universitatea Tehnică „Gheorghe Asachi” din Iași
Tomul LVI (LX), Fasc. 3, 2010
Secția
ȘTIINȚA ȘI INGINERIA MATERIALELOR

RESEARCH ON STRUCTURAL CHANGES OF CAST IRON HEATED WITH CONCENTRATED SOURCES GIC200 LASER BEAM OF ELECTRONS TO INCREASE WEAR RESISTANCE

BY

LAURENȚIU MARIN and ADRIAN DIMA

Abstract. Surface heat treatment of samples using concentrated energy sources will increase the apparent resistance to wear of parts made from these materials. In structural issues is presented and characteristic micro-hardness.

Key words: surface heat treatment, energy sources, micro-hardness.

1. The Method of Research

The thermal treatments executed with concentrated sources of energy and laser radiations and electron beams are based on thermal phenomenon.

In experimental research we used a laser facility for surface heat treatments (Fig. 1) produced by INTEC Bucharest, plant, which can generate a impulse beam of 10 KW maximum power for a focused diameter of 4 mm, $E = 10 - 100$ J diameter. The gas environment is composed of a mixture of helium, nitrogen and carbon dioxide.

The generation of the free electrons is made through thermo-electrical emission. The electrons send by the cathode are accelerated towards the anode due to the potential difference between the cathode and anode. These electrons are focused in a fascicle/beam according to the confirmed system configuration of polarization of the cathode – anode.

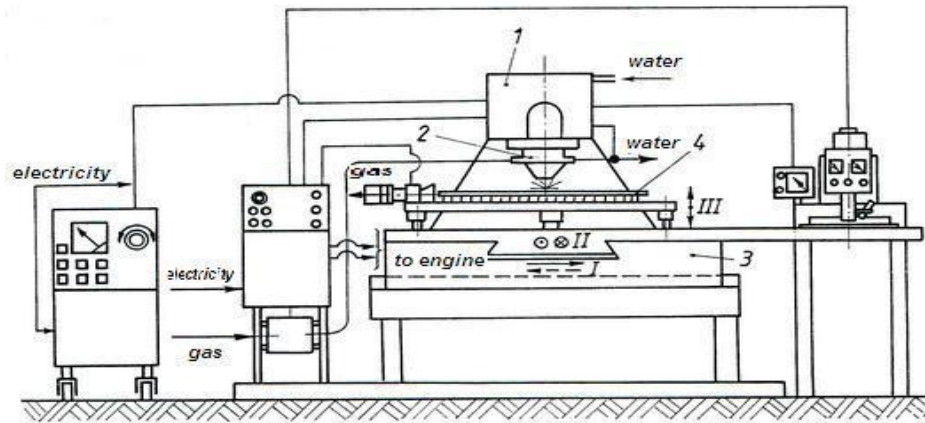


Fig. 1 – Laser installation for the superficial surface heat treatments: 1– laser;
2 – Laser beam focusing system; 3 – Specimen apparatus;
4 – The test-piece which needs to be treated.

Laser heating carried out under the scheme in principle shown in Fig. 2 which noted that serum has a particular importance of focusing the laser beam system to obtain results.

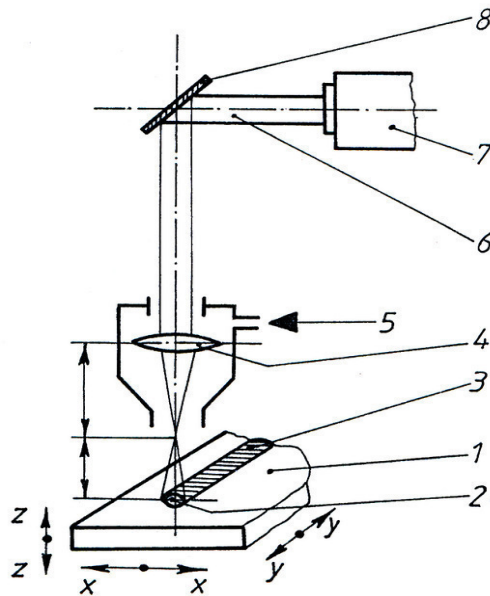


Fig. 2 - The schematic diagram of laser surface heating: 1 – Radiated area;
2 – Light spot; 3 – Radiated band; 4 – Optical focusing system; 5 – Inert gas;
6 – Laser beam; 7 – Device for obtaining the laser beam; 8 – Rotating mirror.

Thermal plant surface with electron beam used in the experiments has the following principle scheme (Fig 3).

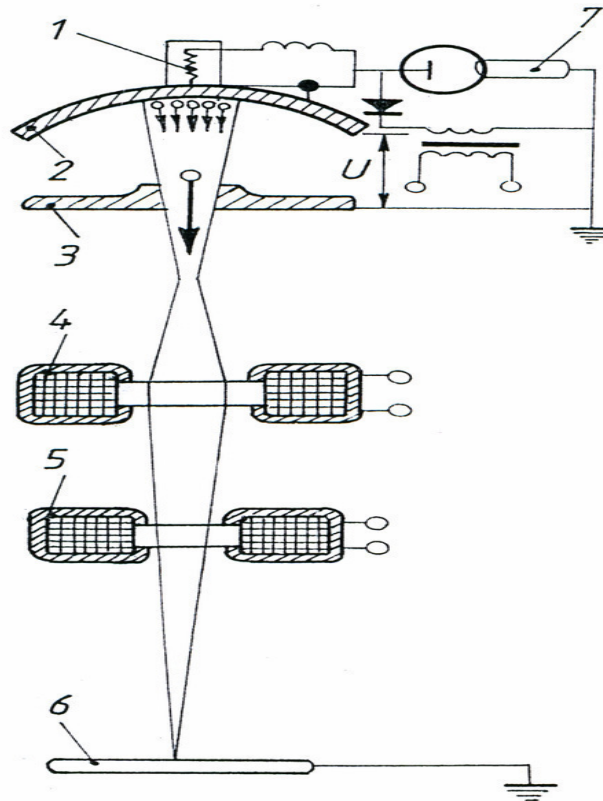


Fig. 3 – Schematic diagram of the installation of the thermal electron beam (e-gun):
 1 – Thermo electronic cathode emission; 2 – Electrode focusing device;
 3 – Anode for acceleration; 4 – Magnetic lenses; 5 – Deflection coil;
 6 – Piece to be treated thermally.

For the trials we used grey cast iron GCI 200 in the given composition: C 3,21%, Si 2%, Mn 0,7 %, Ni 1,5%, Cr 0,7%, P 0,6%. This cast iron depicts a ferro - perlite structure. The 100 x 100 x 8 mm test pieces have been heated with a laser beam in which a 1 mm layer of black carbon coating has been used to obtain a treated layer of 4mm thickness. For the treatment, used a laser system of heating ($P = 10 \text{ kw}$, $v = 7 \text{ mm/s}$) which let to a depth of treated layer of 0,6 mm, gaining a hardness of 672 HV (640 HB). From the same batch of test-pieces we treated superficially with thermal and electrons fascicle/beams (speed 0.7 mm/s, radiation power 7 km, deepness 0,4 mm and $U = 10 \text{ kw}$).

2. Experimental Results

The micro hardness gained as a result of the electron fascicle/beam laser treatment is presented in image no. 4 and 5.

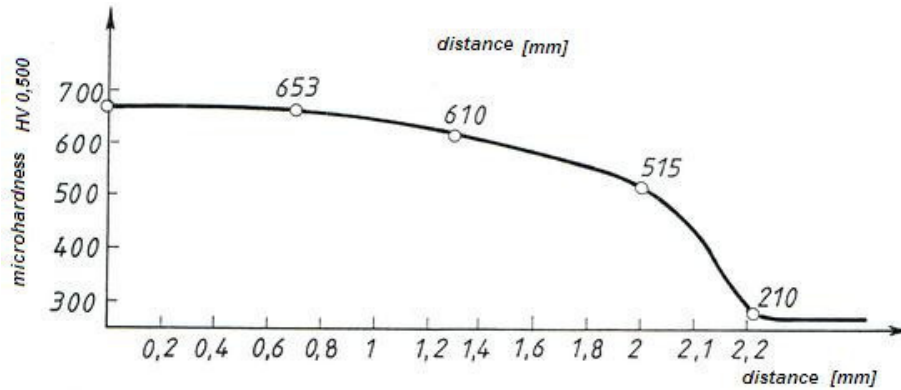


Fig. 4 – Micro hardness variation of sample of GIC 200 as a result of the laser treatment.

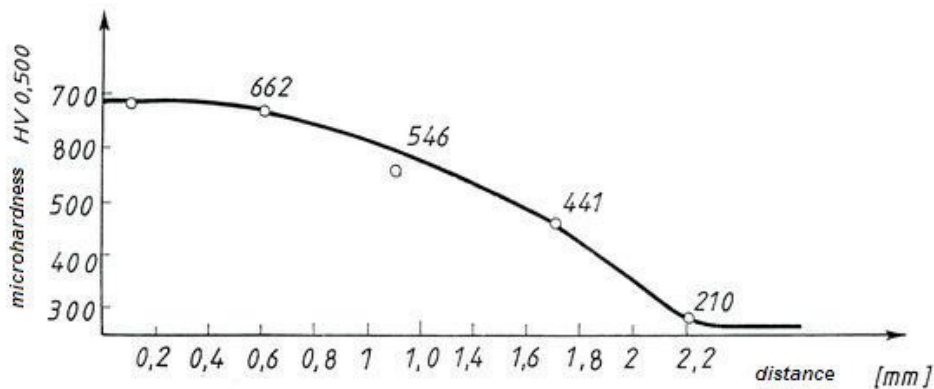


Fig. 5 – Micro hardness variation of iron cast GIC 200 as a result of electrons fascicle thermal treatment.

In both cases it can be seen that due to the finishing structure of the ferro – perlite powder it results an increase of micro hardness at the test-pieces surfaces in comparison with the micro hardness of the cores.

3. Conclusion

It can be clearly seen that the efficiency and timeliness of the surface thermal treatments in order to increase, the hardness and the durability of the grey cast iron pieces subjected to a severe wear out system.

A c k n o w l e d g e m e n t. This paper was realised with the support of BRAIN “Doctoral scholarships as an investment in intelligence” project, financed by the European Social Found and Romanian Government.

Received: May 14, 2010

“Gheorghe Asachi” Technical University of Iași,
Department of Materials Science
e-mail: laurentiumarin@vn

REFERENCES

1. Pavelescu D., *Tribology*. E.D.P., București, 1977.
2. Marin L., Ph. D. Diss., Iași, 2010.
3. Lazăr Gh., Bogdan S.V., Popescu R.M., *Research Concerning Local Heat Treatments for Welds*. Internat. Conf. on Material Sci. a. Engng. Bramat, Welding Engng., Book of Abstracts, Brașov, 229 (2007).

CERCETĂRI ASUPRA SCHIMBĂRILOR STRUCTURALE DIN FONTĂ ÎNCĂLZITĂ CU SURSĂ CONCENTRATĂ DE LASER GIC200 PENTRU A CREȘTE REZISTENȚĂ LA UZURĂ

(Rezumat)

Tratarea termică a suprafețelor epruvetelor prin intermediul surselor concentrate de energie va conduce la creșterea evidentă a rezistenței la uzare a reperelor fabricate din aceste materiale. În lucrare sunt prezentate aspecte structurale și de microduritate caracteristice.

A STUDY OF INFLUENCE OF CARBURIZING ON SINTERED PRODUCTS

BY

MIHAELA MARIN and ELENA DRUGESCU

Abstract. In this paper is presented the influence on thermochemical treatment of sintered products. Were analyzed two types of powders, an iron-based powder (P_1) and an alloyed powder (P_2) with the following elements: Cu, Ni and Mo. Carburizing was carried out in fluidized bed at temperature of 900°C , maintaining 20 minutes and respectively, 40 minutes for the two types of powders studied. It found that the best values of Vickers microhardness were recorded when carburizing time is 40 minutes for powder P_2 .

Key words: powder metallurgy, sintering, carburizing.

1. Introduction

Parts produced by powder metallurgy (PM) are widely used, especially in the automotive industry worldwide. Powder metallurgy parts of complex shapes are obtained and close to final form, with precise surface, so that specific parts produced by powder metallurgy helps to save time, energy, materials, labor and money [1],..., [3]. Compared with conventional metals, additional processes (such as processing, forging, etc.) are minimized in powder metallurgy [4], [5].

To obtain sintered parts metal powders are used, whose characteristics (size, shape, structure, surface quality) are determined by the material they are made and the technological development process. Metal powders by shape, size, structure and type of production, have an important impact on static and dynamic properties of the materials produced.

An important role in shaping and sintering is the powder morphology an dimensions, contributing to the microstructure of sintered material. Sintered material properties are determined by the nature of material, powder

characteristics used by pressing and sintering process parameters and post processing procedures applied [6].

Sintering is the process of compaction, consolidation heat treatment ($T < T_{top}$) of a solid, which is a porous bulk made from powder. Is a process representing a summation of physical and physicochemical phenomena that success or overlap.

Sintering process can be conventionally divided into three stages that succeed in increasing temperature:

- *initial phase* - is to turn the contact point between particles bridges and their expansion to about 25-30% of the particle radius, with the formation of "necks" which cause hardening of the bulk. At this stage the particles retain their individuality, and contractions are small (max. 4-5%).

- *intermediary step* consists in expanding the necks between particles to the particle loss of individuality. At this stage occur 85-90% of total densification and most important growing grain.

- *final stage* starts at a lower porosity - 10% m it consists in transforming the network channels in isolated pores, ring-shaped their large grain growth by including the fine particles. This step is very important for completing the material microstructure.

Mechanisms involved in the transport of material in sintering are the surface diffusion, intergranular limits diffusion and the volume diffusion (Fig. 1).

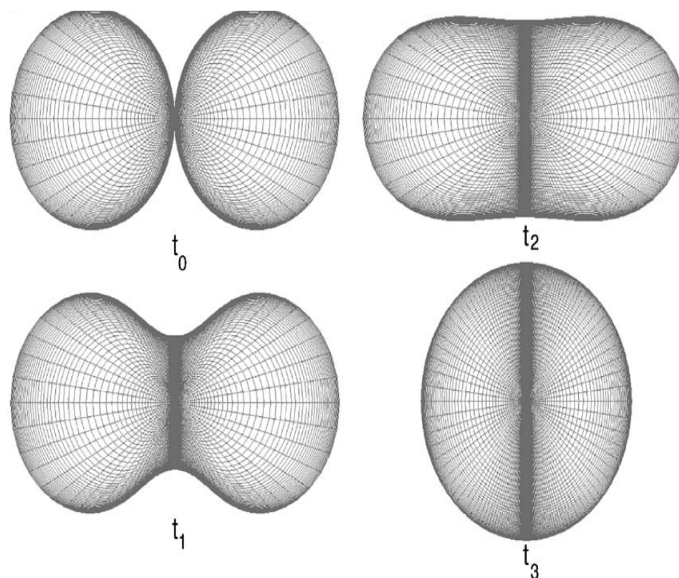


Fig. 1 – The schematic of two powder particles during sintering, carried out by finite element method at different sintering times, $t_0 < t_1 < t_2 < t_3$ [7].

In addition, the mechanical properties of steel powders can be modified depending on the composition, density and type of heat treatment applied. On hardening steels of low carbon powder, hard phases, as martensite and bainite are needed in microstructures. On the other hand, ferrite and pearlite areas specific in powder metallurgy steels help improve the tensile strength.

2. Experimental Procedure

This paper aims to analyze the thermochemical treatment of carburizing on sintered products based on iron powder. Studied powders are produced by water atomisation. The chemical composition of the two powders are shown in Table 1.

Table 1
Chemical Composition of Analyzed Powder

Powder type	Cu %	Mo %	Ni %	C %
P ₁	0.096	0.08	0.046	<0.01
P ₂	1.50	0.50	1.75	<0.01

High purity of powder assures a remarkable compressibility. Combination of purity, high compressibility and resistance in pressed state confers to the studied powder ideal for use as complex components, where strength and density are high. Table 2 presents the sieve distribution of the powders, determined by sieving machine.

Table 2
Sieve Distribution of Analyzed Powders

Sieve size	Granulate size distribution			
	P ₁		P ₂	
	m(g)	Xp(%)	m(g)	Xp(%)
>150 μm	2,78	3%	3,72	4%
>100 μm	17,73	18%	20,98	21%
>63 μm	25,01	25%	30,65	31%
>45 μm	20,19	21%	20,99	21%
Plate	32,22	33%	23,90	23%
m(g)	99,93	100 %	99,64	100 %

The analyzed powders were pressed at room temperature using a hydraulic press at a pressure of 600 MPa. Cylindrical samples were pressed into

8x6 mm dimensions. In order to minimize the effect of wall friction between the mold and powder, a lubricant that zinc stearate, 1% was added. Lubricant not only reduce friction between particles, but also facilitates removal mold parts.

Pressed samples were sintered at 1150°C in a sintering furnace. The total cycle lasted 2 h, 60 min was maintained at maximum temperature of 1150°C.

After sintering, samples were carburized in fluidized bed at a temperature of 900°C, with different times, respectively 20 minutes and 40 minutes, after which they were cooled in air. The purpose of this review is to highlight the layer formation and microhardness measurements.

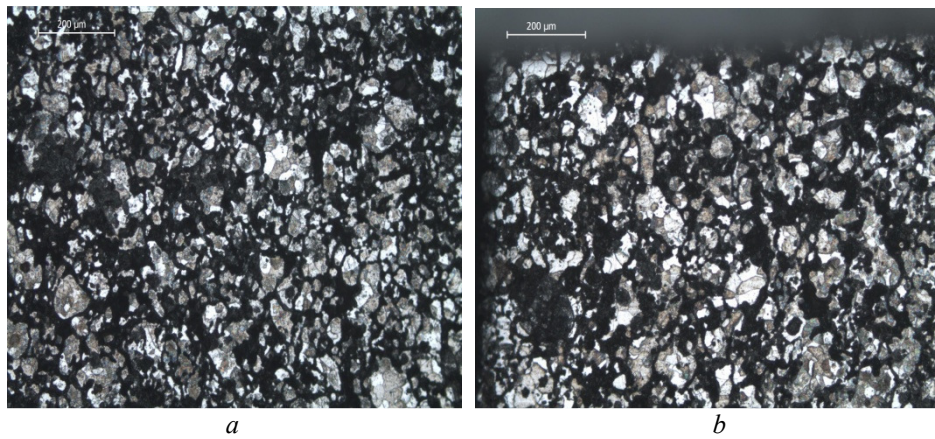


Fig. 2 – Microstructures of sample sintered (powder P₁) at 1150°C:
a – surface; *b* – core (100x).

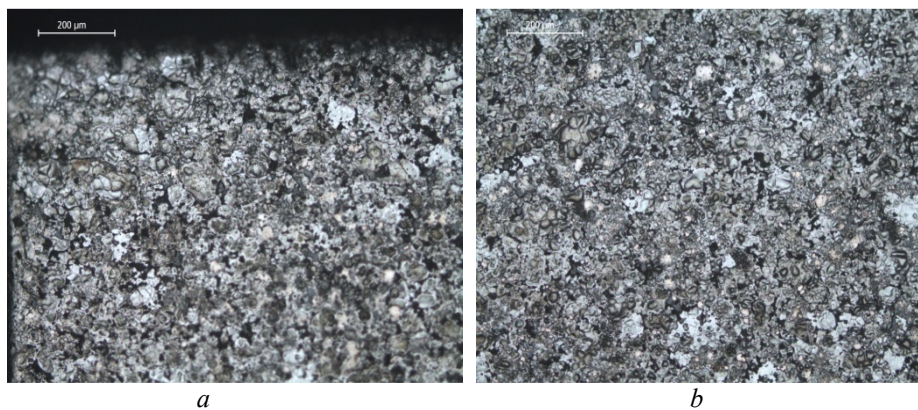


Fig. 3 – Microstructures of sample sintered (powder P₂) at 1150°C:
a – surface ; *b* – core (100x).

Carburizing is the addition of carbon to the surface of low-carbon steels at temperatures generally between 850 and 950°C (1560 and 1740°F), at which austenite, with its high solubility for carbon, is the stable crystal structure. Hardening is accomplished when the high-carbon surface layer is quenched to form martensite so that a high-carbon martensitic case with good wear and fatigue resistance is superimposed on a tough, low-carbon steel core.

Carburized steels have a complex microstructural composition at a high carbon surface, composed of martensite, residual austenite and carbides, which leads to high surface hardness and increased mechanical resistance to fatigue and wear. The combination of these properties is recommended for applications where high loads are required and cyclic loads, such as gears [8], [9]. Carburized layer depth is a function of carburizing time and carbon potential available surface [10].

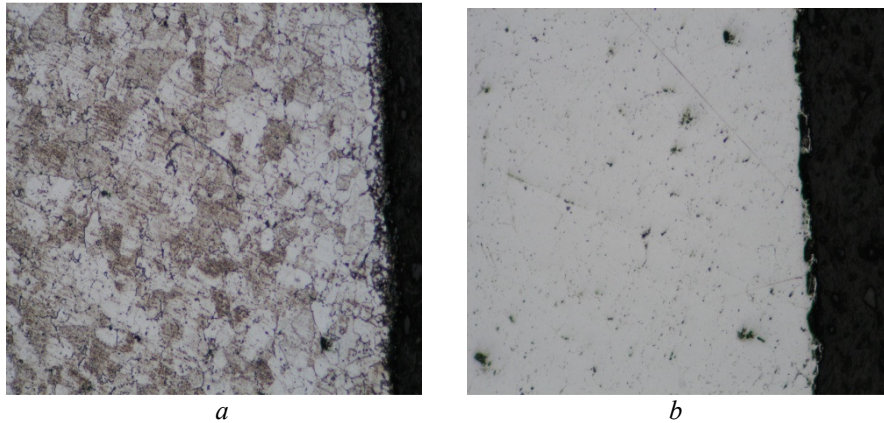


Fig. 4 – Microstructures of sample carburized (powder P_1) at 900°C, 20minutes (200x): *a* – unetched; *b* – etched Nital (2%).

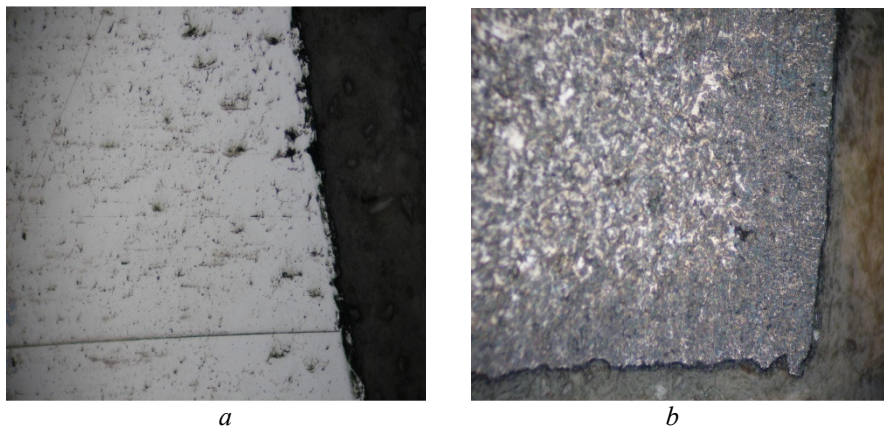


Fig. 5 – Microstructures of sample carburized (powder P_1) at 900°C, 40minutes (200x): *a* – unetched; *b* – etched Nital (2%).

When carburizing times are prolonged, deep carburized layers is obtained, a potential carbon produces a surface with a high carbon content, which can lead to a structure consisting of residual austenite in excess or free carbides. These two microstructural elements have adverse effects on residual stress distribution in the fuel layer. Therefore, a high carbon potential may be suitable for short carburizing times, but not for prolonged carburization. In this study, it appears that only the carburized sample with 40 minutes is showing the carburized layer. Microstructures of carburized samples for maintaining time of 20 minutes and 40 minutes are shown in Figs. 4 and 5 for powder P₁.

Microstructures of carburized samples for maintaining time of 20 minutes and 40 minutes are shown in Figs. 6 and 7 for powder P₂.

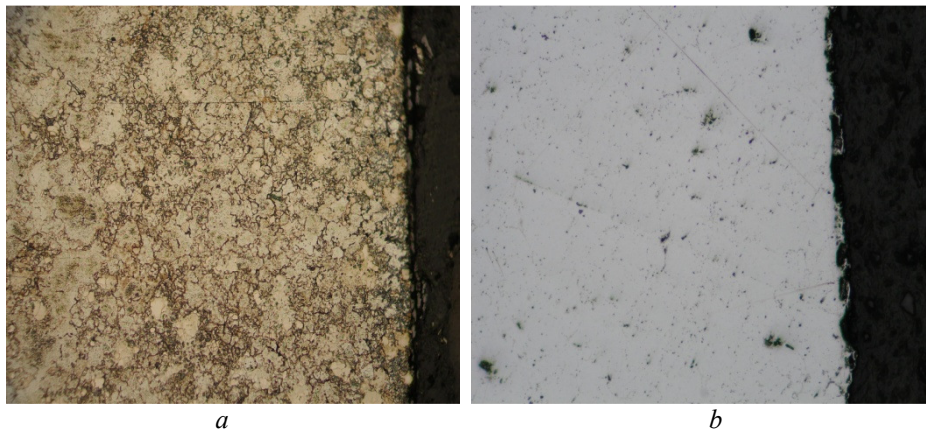


Fig. 6 – Microstructures of sample carburized (powder P₂) at 900°C, 20minutes (200x):
a – unetched; *b* – etched Nital (2%).

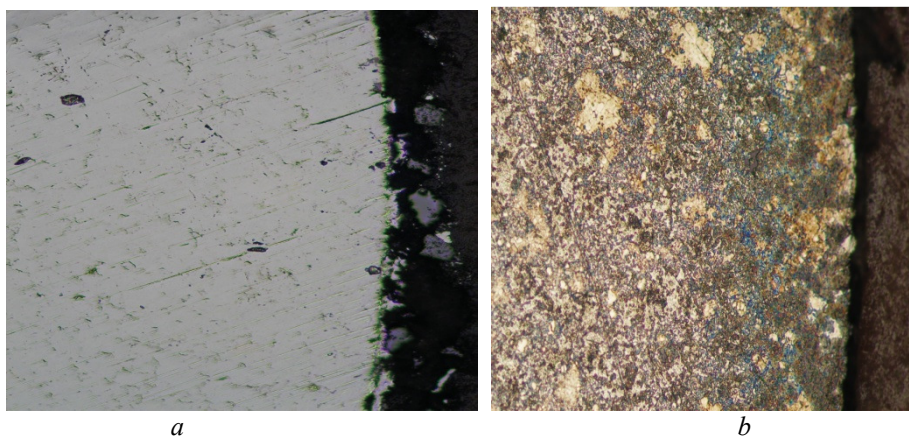


Fig. 7 – Microstructures of sample carburized (powder P₂) at 900°C, 40 minutes (200x):
a – unetched; *b* – etched Nital (2%).

Vickers microhardness tests were performed on carburized sample. The load was 100gf with standby time of 20s, each value represents an average microhardness of at least three determinations.

3. Results and Discussions

In Fig. 8 and Fig. 9 are presented the microhardness variation from surface to the center of carburized sample (P_1 and P_2) at $T=900^\circ\text{C}$, 40 minutes.

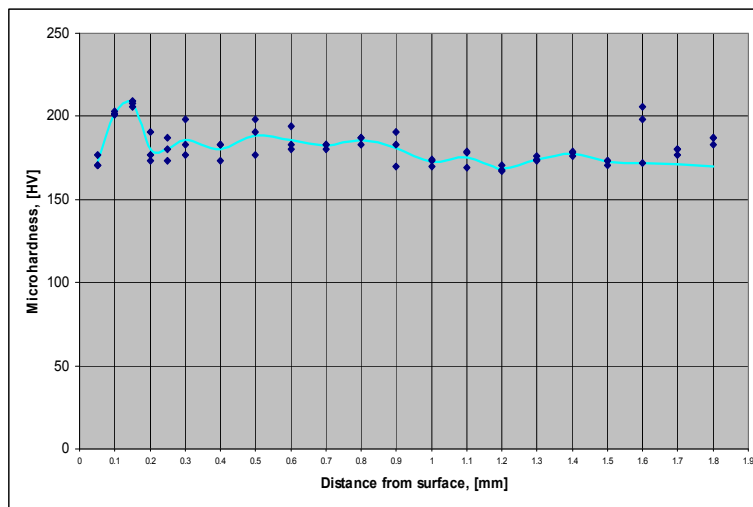


Fig. 8 – Microhardness variation from surface to the center for carburized sample (powder P_1) at $T=900^\circ\text{C}$, 40 minutes.

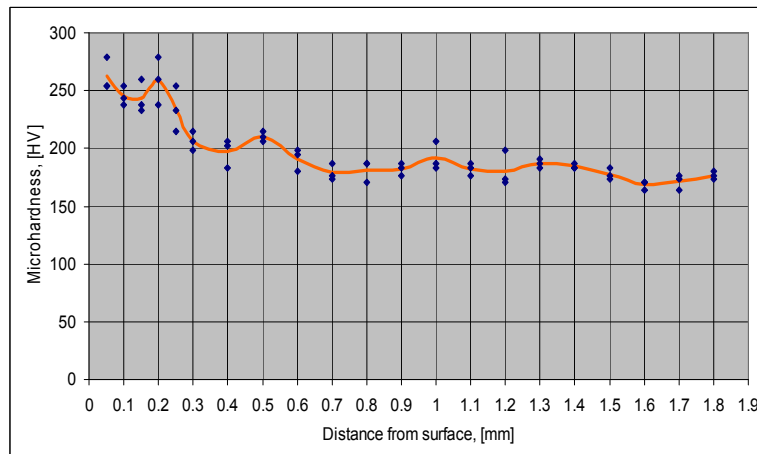


Fig. 9 – Microhardness variation from surface to the center for carburized sample (powder P_2) at $T=900^\circ\text{C}$, 40 minutes

As is depicted in the Fig. 8 for sample P₁, further cooling in the air, it allows easy decarburizing the superficial layer of the sample, which explains the amounts lower of microhardness to about 0.2 mm distance from surface.

Comparing the two types of powder, is found that the powder P₂ presents the best values of Vickers microhardness.

4. Conclusions

The experiments have shown that the best hardness values were recorded when the sample was carburizing at 900° C for 40 minutes, especially for powder P₂.

When carburizing times are prolonged, deep carburized layers is obtained, a potential carbon produces a surface with a high carbon content.

Carburized layer depth is a function of carburizing time and carbon potential available surface.

Received: May 14, 2010

University "Dunărea de Jos" of Galați
Department of Metallurgy and Materials Science
e-mail: mihaelagheorghe2003@yahoo.com

REFERENCES

1. Sudhakar K.V., *Fatigue Behavior of the High Density Powder Steel Metallic*. Int J. Fatigue, 22, 729-734 (2000).
2. Jang G.B. Hur, Kang S.S., *A Study on the Development of the Substitution Process by Powder Metallic in Automotive Parts*. J. Mater. Proc. Technol., 110-115 (2000).
3. Chawla N., Murphy T.F., Narasimhan K.S., Koopman M., Chawla K.K., *Axial Fatigue Behavior of Binder-Treated Versus Diffusion Alloyed Powder Metallic Steels*. Mater. Sci. Engng., A, 38, 180-188 (2003).
4. Suryanarayana C., Ivanov E., Boldyrev E.E., *The Science and Technology of Mechanical Alloying*. Mater. Sci. Engng., A, 304-306, 151-158 (2001).
5. Krauss G., *Residual Stress and Fatigue Microstructures of Carburized Steels*. Proc. of the Quenching and Carburizing, The Institute of Materials, Melbourne, 205-225 (1998).
6. Brândușan A., *Research on the Development of Sintered Materials Based on Iron Powders Having High Fatigue Resistance*. Tech. Univ. of Cluj-Napoca.
7. Dzhokhar H., Martinez-Herrera J., Jeffrey J., *Transport Mechanisms and Densification During Sintering: I. Viscous Flow Versus Vacancy Diffusion*. Dept. of Chem. Engng. a. Mater. Sci., Univ. of Minnesota, Minneapolis, MN55455-0132, USA, (2000).

8. Narasimhan K.S., *Sintering of Powder Mixtures and the Growth of Ferrous Powder*. *Metallic. Mater. Chem. Phys.*, 67, 56-65 (2001).
9. Krauss G., *Principles of Heat Treatment of Steels*. American Society for Metals, 1, 251 (2004).
10. * * *Case Hardening of Steel*. ASM Internat., 1, 4, 1987.

STUDIUL INFLUENȚEI CARBURĂRII ASUPRA PRODUSELOR SINTERIZATE

(Rezumat)

În această lucrare este prezentată influența tratamentului termochimic asupra produselor sinterizate din pulberi. Au fost analizate două tipuri de pulberi, o pulbere cu baza de fier (P_1) și o pulbere aliată (P_2) cu următoarele elemente: Cu, Ni și Mo. Carburarea a fost realizată în strat fluidizat, la temperatura de 900°C, cu timp de menținere diferit, respectiv 20 minute și 40 minute pentru cele două tipuri de pulberi studiate. Se constată că, cele mai bune valori ale microduranței Vickers au fost înregistrate în cazul carburării cu timpul de menținere de 40 minute și pentru tipul de pulbere P_2 .

INFLUENCING FACTORS OF CENTRIFUGAL SEDIMENTATION PROCESS

BY

VALENTIN MOLDOVAN, DOREL NEMEȘ and EMIL BRUJ

Abstract. We studied the influencing factors of centrifugal powder sedimentation process (defloculant agent concentration, centrifugation speed and time).

Key words: centrifugation, sedimentation, powder, influencing factors.

1. Introduction

The gravitational sedimentation process for obtaining gradual porous materials based on gravitational acceleration [1] are usually limited to particles with diameters over $1\mu\text{m}$. This limit may be lowered if we use centrifugal force instead of gravitational acceleration. In this way, even using ordinary laboratory centrifuges the particles size limit may be lowered to a diameter of $0.05\mu\text{m}$. Suspensions centrifugal sedimentation process ensures the reduction with (1-2) orders of magnitude of the sedimentary particles size (about below $0.100\mu\text{m}$ - 100nm). Consider a container with a suspension of solid particles, entrained in a rotating speed ω . Under the action of centrifugal force, these phases will be separated from each other making the deposit on the inner wall of the container. The techniques ensemble that allows such a separation is called centrifugation.

Depositions with addition material can use for increasing wear resistance of sliding surfaces of lathes beds, as well as pair-surfaces from mobile slide.

During rotation of the centrifuge container filled with particle suspension, the centrifugal force tends to stick solid particles to the inner wall of the container forming a sediment layer composed of particles [2].

Centrifugal sedimentation process allows the obtaining of porosity gradient membranes [3]. By this method porosity gradient filters were obtained with 18 mm in diameter, 0.1 mm and 1mm in thickness using TiO_2 powder in aqueous suspension containing particles with sizes between 10nm - $5\mu\text{m}$ [4], [5].

2. Experimental

For the experimental tests in order to determine the influencing factors of centrifugal powder sedimentation $\text{NiO} < 1\mu\text{m}$ powder particles were used. A suspension with 2.8% concentration of powder and 0.2% - 0.4% dispersant agent was prepared.

S1 - 2,8% NiO powder, 0,2% dispersant agent, 97% water.

S2 - 2,8% NiO powder, 0,4% dispersant agent, 96,8% water.

The test tube has a 7 ml volume. For each centrifuge test 7ml of the initially prepared suspension was used. The process was carried out using a laboratory centrifuge type “Janetzki T24” with variable speed in the range of 0-16000 rpm.

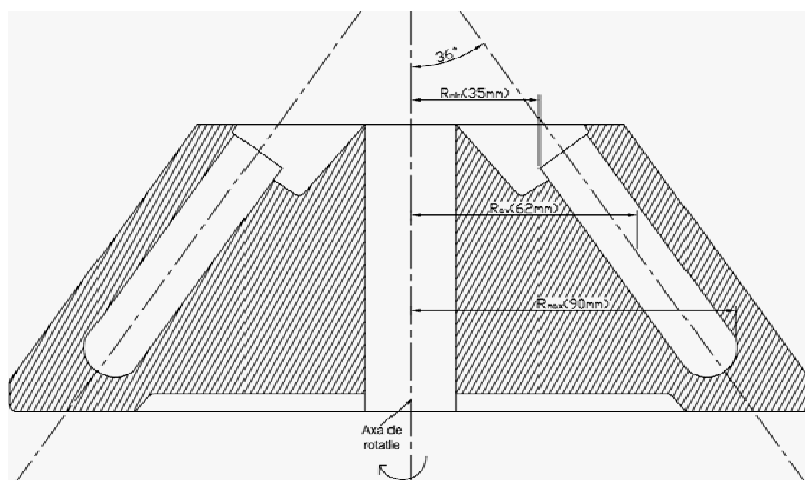


Fig. 1 – Schematic representation of centrifuge head.

Centrifugal force varies according to the length of the radius at which the particle is at a given moment. To emphasize this variation, Fig. 2 shows the relative acceleration (Z factor) dependence on speed for the minimum, mean and maximum of radius, of the used centrifuge head.

To study influencing factors of centrifugal sedimentation the fotosedimentation method was used (Turbidimetry) according to ASTM B 430 standard.

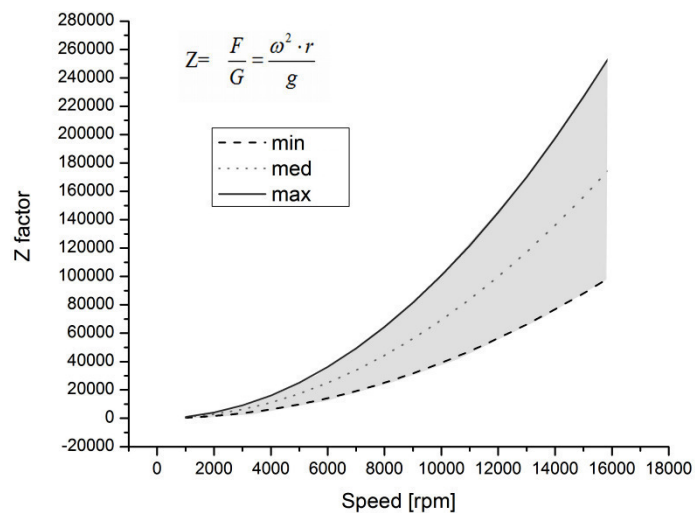


Fig. 2 – Variation of relative acceleration (Z factor) depending on speed and radius.

The centrifuged powder suspension was introduced in a glass cell. A collimated light beam passes through the cell. The intensity of light beam was measured by the generated voltage of the photo detector that captures the light beam passing through suspension. Generated voltage is measured using a milli voltmeter and a data recorder [6].

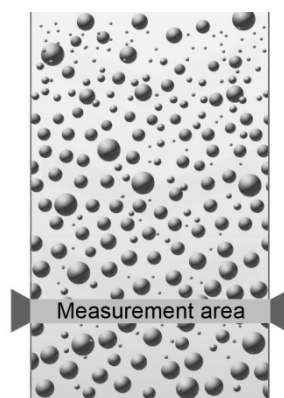


Fig. 3–The principle scheme of determining turbidity of homogeneous suspension.

Two important conditions are necessary for determining homogeneous suspension turbidity, which if not met can lead to erroneous analysis. First is correct sampling. Tests are conducted with relatively small amounts (from tenths of grams to several grams), and these samples must be representative for

the entire amount of powder. We can say that the most important factor for accurate and precise results is the dispersion. Coagulation process due to insufficient dispersion has the effect of different sizes particles agglomeration. Smaller particles agglomerated around the larger particles and settle simultaneously, therefore the Stokes law is not respected.

3. Results and Discussions

The influencing factors of centrifugal sedimentation process were revealed by centrifuging of $<1\mu\text{m}$ particle size powder suspensions with at different parameters, measuring and comparing the suspension turbidity values after each centrifugation.

3.1. Determination of the Optimal Dispersant Agent Concentration

Studies were done on the influence of dispersant agent concentration in suspension for different centrifugation parameters. For research S1 and S2 prepared suspension were used.

The results of experimental centrifugation tests for S1 and S2 suspensions at 1000rpm are shown in Table 1:

Table 1

Turbidity of the S1 and S2 Suspension According to the Time of Centrifugation

Time [min.]	0	1	2	3	4	5	6	7	8
S1Turbidity [a.u.]	0.2	0.9	1.7	3	5.2	5.8	8.4	10	13
S2Turbidity [a.u.]	0.2	0.2	0.2	0.2	0.21	0.22	0.22	0.23	0.24

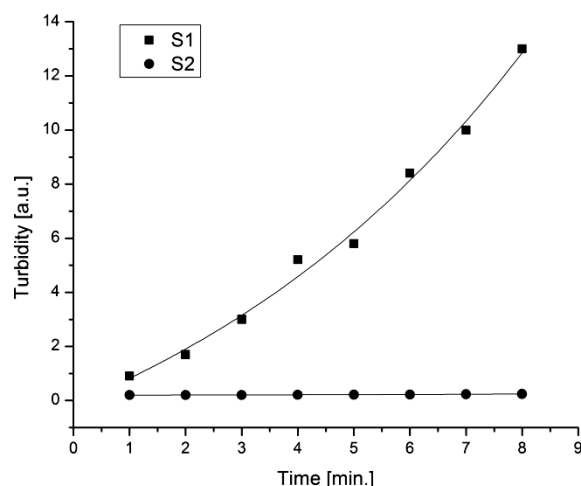


Fig. 4 – The influence of dispersant agent concentration on turbidity at 1000 rpm.

It was concluded that 0.2% concentration of dispersant agent in suspension (S1) was insufficient to disperse the powder particles and lead to increasing the size of powder particles by flocculation. In S2 suspension for a better dispersion was chosen a higher concentration of dispersant agent (0.4%). This concentration leads to a uniform dispersion of powder particles and stabilize the suspension.

Comparing the results of two experiments we show the importance and role of dispersant agent. In the first case we obtained a suspension of agglomerated powder particles 1000rpm was sufficient to deposit the particles in suspension. In the second case we obtained a stable suspension where the speed of 1000rpm had little influence on the desagglomerated particles in suspension.

3.2. Centrifugation Time

Starting from previous results with S1 and S2 suspension where the speed was relatively small, attempts were made by increasing the centrifugal sedimentation speed at 5000rpm but in this case only for S2 suspension. The results are presented in Table 2.

Table 2
Turbidity of the S2 Suspension According to the Time of Centrifugation

Time[<i>min.</i>]	0	1	3	5	8
Turbidity [a.u.]	0.2	0.24	0.5	0.94	3.4

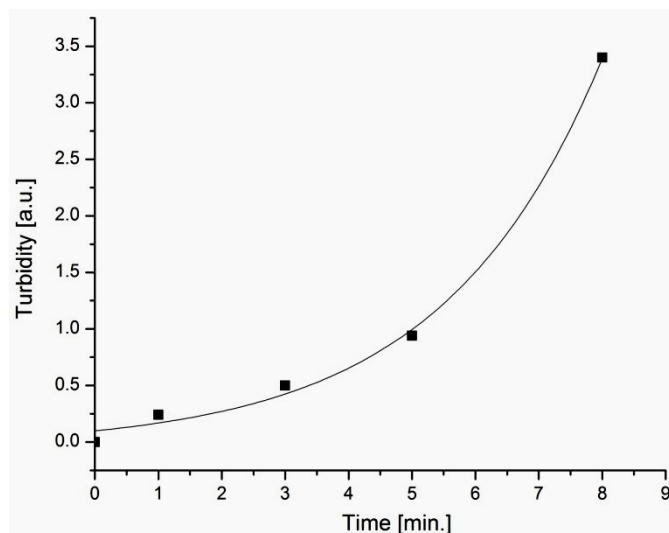


Fig. 5 – The influence of centrifugation time on turbidity at 5000 rpm.

Comparing graphs 4 and 5 is apparent a variation of turbidity values for S2 suspension in the same experimental conditions at different speeds. From this we can infer an influence of the centrifugation speed on the particles in suspension.

Starting from the conclusion above tests have been made in order to determine the influence of centrifugation speed on the particles in suspension.

3.3. Centrifugation Speed

Using the same suspension as in previous experiments (S2) centrifugal sedimentation attempts were made at different speeds. In this case, the centrifugation time was kept constant at 3 minutes for each determination. The results are shown in Table 3.

Table 3
Turbidity of the S2 Suspension Depending on Centrifugation Speed

Speed [rpm]	0	1000	3000	5000	8000	10000	12000
Turbidity [a.u.]	0.2	0.2	0.26	0.72	2	5	10

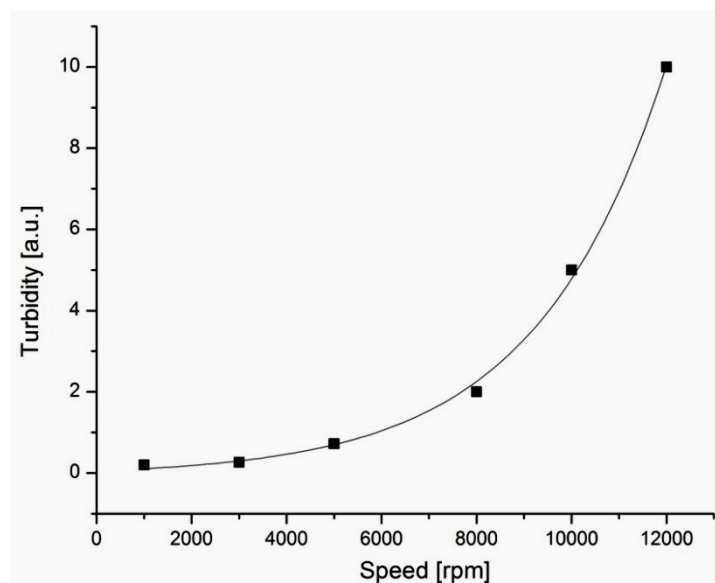


Fig. 6 - Turbidity of the S2 suspension depending on centrifugation speed at 3 minute centrifugation time.

Fig. 6 shows the variation of turbidity according to the centrifugation speeds. It may be noted that speed has a major influence on the centrifugal

sedimentation process of particles in suspension. There is a pronounced increase of turbidity values if the speed exceeds 8000 rpm. This increment can be achieved not only by increasing the centrifugation speed but also by increasing the centrifugation time, outlined in Fig. 5 where one can see a centrifugation efficiency more than 4 to 5 minute, even if the speed is lower.

4. Conclusions

The limit of the gravitational sedimentation process ($\sim 1\mu\text{m}$) may be lowered if we use centrifugal force instead of gravitational acceleration. In this way, even using ordinary laboratory centrifuges the particles size limit may be lowered to a diameter of $0.05\mu\text{m}$. Suspensions centrifugal sedimentation process ensures the reduction with (1-2) orders of magnitude the sedimentary particles size (about below $0.100\mu\text{m} = 100\text{ nm}$).

Studies were done on the influence of dispersant agent concentration in suspension for different centrifugation parameters. It was concluded that in S1 suspension the powder particles size has been increased by flocculation obtaining a suspension of agglomerated powders and the 1000rpm speed was sufficient to deposit the particles. The S2 suspension was stable at 1000rpm centrifugation speed even for eight minutes.

Experimental tests were conducted to determine the influence of the centrifugal sedimentation speeds on the powder particles.

There was a pronounced increase of the centrifugation efficiency (NiO powder with $<1\mu\text{m}$ grain size) with speeds above 8000 rpm, but also by increasing the centrifugation time over 4-5min at lower centrifugation speeds.

A c k n o w l e d g e m e n t s. The authors would like to thanks the UEFISCSU for financial support in Program IDEI”, Project no: 749/19.01.2009.

Received: May 14, 2010

Technical University of Cluj-Napoca,
Department of Materials Science and Technology
e-mail: Valentin.MOLDOVAN@stm.utcluj.ro

REFERENCES

1. Vida-Simiti I., Jumate N., Moldovan V., Sechel N., Thalmaier Gy., Bruj E., *Preliminary Studies and Researches on the Elaboration of Gradual Porous Sintered Structures by Powder Sedimentation*. Proc. of 4th Internat. Conf. on Powder Metal., RoPM2009, Editor: L. Brandusan, p. 124, Craiova, July, Risoprint, Cluj-Napoca, 2009.
2. Vida-Simiti I., *Procedee fizico-mecanice de separare a poluanților*. U.T. PRES, Cluj-Napoca, 233 (2007).
3. Moritz T., Werner G., Tomandl G., Mangler M., Eichler H., Lembke U., Hauffe W., in: W.A. Kaysser (Ed.), *Functionally Graded Materials*. Proc. of the 5th Internat.

Symp. on FGM, 1998.

4. Biesheuvel P.M., Breedveld V., Higler A.P., Verweij H., Chem. Eng. Sci. 56, 3517–3525 (2001).
5. Moritz T., Riedel H., Werner G., Tomandl G., J. Mater. Sci., 35, 2235–2240 (2000).
6. * * *Powder Metal Technologies and Applications*. ASM Internat. Handbook, 7, 562–563 (1998).

FACTORII DE INFLUENŢĂ AI SEDIMENTĂRII CENTRIFUGALE

(Rezumat)

S-a studiat factorii de influenţă ai procesului de sedimentare centrifugală a pulberilor (concentraţia de agent defloculant, viteza şi timpul de centrifugare).

BULETINUL INSTITUTULUI POLITEHNIC DIN IAȘI
Publicat de
Universitatea Tehnică „Gheorghe Asachi” din Iași
Tomul LVI (LX), Fasc. 3, 2010
Secția
ȘTIINȚA ȘI INGINERIA MATERIALELOR

POROUS MATERIALS OBTAINED BY ALUMINUM ANODIZATION

BY

DOREL-ȘTEFAN NEMEȘ, EMIL BRUJ and VALENTIN MOLDOVAN

Abstract. The paper presents the obtaining of alumina nanoporous membranes by the anodic oxidation method. Using this process, anodic porous structures can be obtained with different characteristics from those of membranes obtained by other methods.

Key words: anodic alumina, anodization, anodic oxidation, nanopores.

1. Introduction

The two-step anodization process for obtaining self-ordered alumina nanostructures was mentioned for the first time in 1995. This increasing attraction for these types of membranes is mainly due to their easy and relatively low cost processing. By two-step anodization it is possible to fabricate well-defined self-ordered porous alumina with different inter pore distances. Recently, the anodization of aluminum is one of the most widely used synthesis method of highly ordered nanostructures. The anodizing of aluminum can result in two different types of oxide film: a barrier-type anodic film, and a porous oxide film. The nature of an electrolyte used for anodizing aluminum is a key factor which determines the type of oxide grown on the surface. Thus, the adherent, non-porous and non-conducting barrier-type of anodic film can be formed by anodizing aluminum in neutral solutions ($\text{pH} = 5-7$) in which the anodic oxide layer stays practically insoluble. These films are extremely thin and dielectrically compact. Porous oxide films are made using strong acid anodizing electrolyte solutions [1],..., [6].

2. Experimental

The substrate used was an aluminum sheet having 0.3 mm in thickness. It was cut to a working diameter of 35 mm.

Before anodization it was initially done the preparation of the surface that will be anodized. To reduce the surface rugosity it was performed a mechanical polishing. To eliminate dislocations, the substrate was then annealed for 1 h at temperature of 350 °C. The aluminum oxide on surface of the layer was removed with a 5% NaOH solution at a temperature of 60°C for 1 min. Aluminum layer was subsequently electrochemically polished for 1 min in a 1:4 mixture of HClO₄ and C₂H₅OH at a current density of 100 mA/cm² at room temperature.

The anodizing process was carried out in two steps. Electrolytes used were two solutions of concentration 0.3 M of sulfuric and oxalic acids. Counter electrode was a Pt mesh and the working distance was chosen according to the type of the electrolyte used. The working bias was chosen depending on the anodizing acid solution, so for anodizing in sulfuric acid the voltage was 25 V and for anodizing in oxalic acid the voltage used was 40 V. For a better homogenization of temperature, the electrolyte was continuously stirred.

Tests of first anodization were made by varying the duration of the process, depending on the acid solution. After the first anodization step the formed alumina layer was chemically removed in a mixture of 1.8% and 7.1% H₃PO₄ CrO₃ in distilled water. The aluminum was re-anodized under the same anodizing conditions as those used in the first anodization. After anodization the remaining aluminum substrate was dissolved in a saturated solution of HgCl₂, thereby obtaining a porous anodic alumina thin film. The obtained samples were subjected to a chemical process for opening and enlarging the pores by immersion in a solution of H₃PO₄.

3. Results and Discussions

First anodization is done in order to obtain a pattern on the aluminum surface that will trigger a well-ordered growth of the alumina oxide layer by the second anodization. The first anodization in sulfuric acid was done for 1 hour. For oxalic acid the anodization time was 2 hours. Fig. 1 presents the structures of the layers obtained in the two electrolytes, after first anodization.

It was observed that in sulfuric acid the anodization process is faster due to increased growth rate of the oxidic layer.

The duration of the second anodization step will determine the thickness of the obtained porous alumina. Fig. 2 presents the structures of the oxidic films obtained by anodization in sulfuric acid for 2 hours, respectively in oxalic acid for 6 hours.

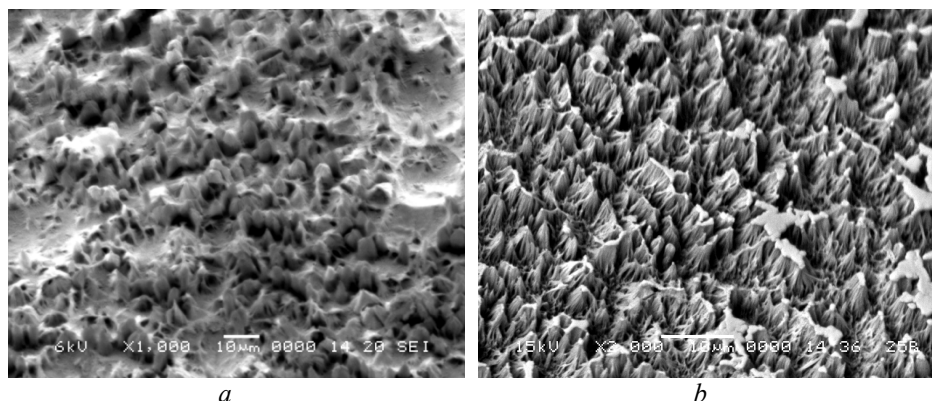


Fig. 1 – Oxidic structures obtained by first anodization: *a* – 2 h oxalic acid; *b* – 1 h sulfuric acid.

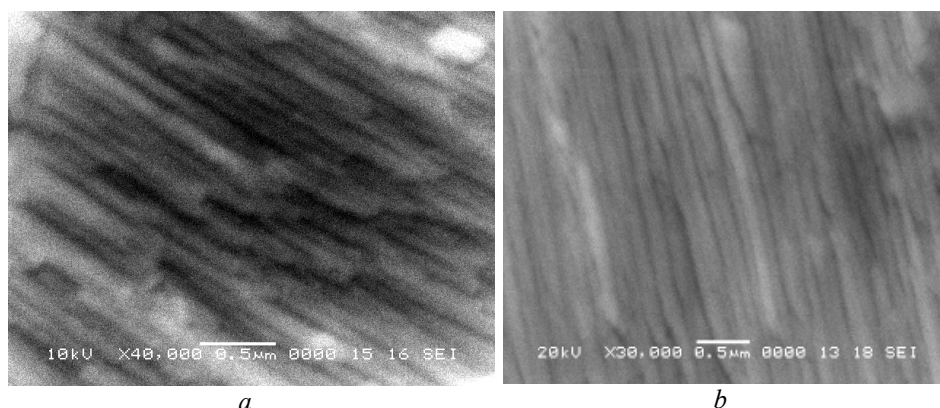


Fig. 1 – Oxidic structures obtained by a two step anodization process: *a* – 2 h sulfuric acid; *b* – 6 h oxalic acid.

3. Conclusions

Anodization time is one of the most important factors for obtaining self-ordered porous structures. During the first anodization irregular pores are formed on the aluminium surface. Depending on the anodization time due to repulsive forces between neighbouring pores the ordering can occur. Anodization process is faster in sulfuric acid electrolyte.

The thickness of the layer obtained after the second anodization step was found to be time dependent.

A c k n o w l e d g e m e n t s. The authors would like to thanks the UEFISCSU for financial support in "Program IDEI", Project no: 749/19.01.2009.

Received: May 14, 2010

*Technical University of Cluj-Napoca
Department of Materials Science and Technology
e-mail: Dorel.NEMES@stm.utcluj.ro*

REFERENCES

1. Grzegorz D. Sulka, Wojciech J. Stepniowski, *Structural Features of Self-Organized Nanopore Arrays Formed by Anodization of Aluminum in Oxalic Acid at Relatively High Temperatures*. *Electrochimica Acta*, *54*, 3683–3691 (2009).
2. Alexander Zahariev, Assen Girginov, *Formation of Complex Anodic Films on Porous Alumina Matrices*. *Bull. Mater. Sci.*, **26**, 3, 349–353 (2003).
3. Stefan Mátéfi-Tempfli, Mária Mátéfi-Tempfli, Luc Piraux, *Characterization of Nanopores Ordering in Anodic Alumina*. *Thin Solid Films*, *516*, 3735–3740 (2008).
4. Sulka G.D., Stroobants S., Moshchalkov V., Borghs G., Celis J.P., *Synthesis of Well-Ordered Nanopores by Anodizing Aluminum Foils in Sulfuric Acid*. *J. of the Electrochemical Society*, **149**, 7, 97-103 (2002).
5. Xiuli Yang, Xufei Zhu, Hongbing Jia, Ting Han, *Oxygen Evolution: the Mechanism of Formation of Porous Anodic Alumina*. *Monatsh Chem.*, *140*, 595–600 (2009).
6. Thompson G.E., Wood G.C., *Porous Anodic Film Formation on Aluminium*. *Nature*, *290*, 230–232 (1981).

MATERIALE POROASE OBȚINUTE PRIN ANODIZAREA ALUMINIULUI

(Rezumat)

Lucrarea prezintă obținerea materialelor nanoporoase prin metoda oxidării anodice. Prin acest procedeu se pot obține structuri poroase auto-ordonate, cu caracteristici diferite de cele ale membranelor obținute prin alte metode. Experimentele au fost făcute utilizând două tipuri de soluții electrolitice ale acizilor sulfuric, respectiv oxalic. Tensiunile de lucru au fost de 25 V în acid sulfuric și de 40 V în cel oxalic.

ACOUSTIC QUALITY CONTROL SYSTEM FOR CERAMIC PRODUCTS

BY

TIBERIU POTECASU

Abstract. In the current paper the authors studied the possibilities and limitations of a system intended to evaluate the quality of ceramic products directly on the production line. The system is based on a data mining specific approach in analyzing the sound produced by ceramic products when hit in a non-destructive manner.

The research showed that good results in discriminating among different quality grades can be obtained for products having similar shape and size even when working with up to six different quality grades. Reducing the number of quality grades to be discriminated increases the method's precision. In industry the number of necessary quality grades to be discriminated is usually no higher than three, thus the authors consider that the method is suited for industrial implementation.

Key words: ceramics; continuous flux production, non-destructive online quality control, data mining.

1. Introduction

In the current study coarse ceramic sample sets were used. They were made out of common clay using the moist fabrication method by extrusion. Six samples were chosen for testing. These were burned at the following temperatures: 600, 700, 800, 880, 920 and 970°C. For the studied clay different quality grades can be obtained starting from 600°C up to around 1000°C. In large production furnaces there is always a temperature gradient thus in a large batch there are always different quality grades depending on the local temperature in the area of the product. Thus having samples burned in a controlled manner at a specific temperature, different quality grades are obtained. From the six items sample set, two other sets were obtained by reducing the size of the items up to 113 mm and 75 mm. In Fig. 1 a photograph showing the third sample set (75mm) is presented.

1.1. Recording and Analysis of the Sound Pattern for Non-Destructive Percussion

In order to record the sound pattern for non-destructive percussion the samples were held by a thin string from the center of gravity. For percussion a light metal round shaped instrument with a curvature of about 8 cm was used. The curvature of the instrument allows more energetic hits without damaging the sample.

For every sample a number of about 100 percussions were recorded. Throughout the 100 hits set slight modifications were made at the position the sample was held at relative to the center of gravity. Also, slight variations were made regarding the point of impact when hit (closer to the extremities or towards the center). Variations of percussion energy were also made. All these slight modifications were made in order to replicate the probable conditions that might be dealt with when working in industrial conditions.

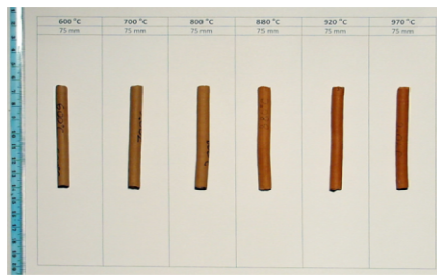


Fig. 1 – Third sample set, burned at: 600°C-75mm, 700°C-75mm, 800°C-75mm, 880°C-75mm, 920°C-75mm, 970°C-75 mm.

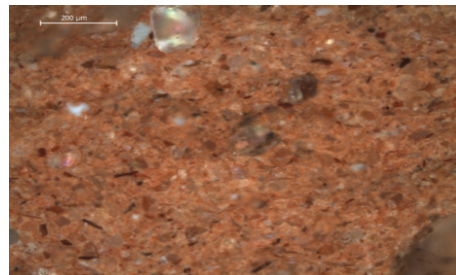


Fig. 2 – The optic microstructure of the studied samples.

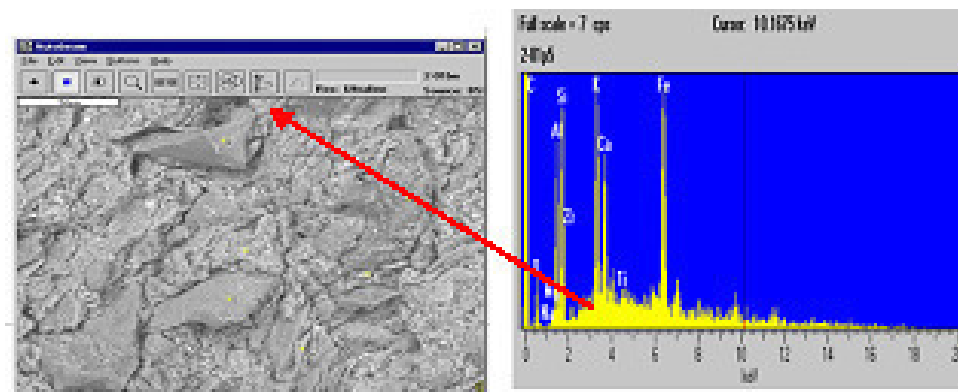


Fig. 3 – EDS analysis of the studied samples.

The recording of the sound patterns at non-destructive percussions was made in a silent environment in order to avoid the alteration of the power spectrum with non-specific elements.

2.1. Data Processing

a) *Calculation of the Power Spectrum*

The data recorded in wav files were loaded into Matlab and the power spectrum was calculated and recorded in a structure with 18 records, one for each item (3_sample_sets x 6_items_per_set). The Matlab code that calculates the power spectrum is:

```
...
[y,Fs,bits] = wavread(fisier);
N = 2.^(ceil(log(length(y))/log(2)));
FFTY = fft(y,N);
NumUniquePts = ceil((N+1)/4);
FFTY = FFTY(1:NumUniquePts);
Pyy = conj(FFTY).*FFTY / N;
f=(99:floor(NumUniquePts/2)-1)*2*Fs/N;
frecvente{i} = f;
Pyy = Pyy(100 : floor(NumUniquePts/2));
putere{i} = Pyy;
```

b) *Scaling the Power Spectrum in [0,1] Domain and Modification of the Sampling Step*

In order to efficiently compare the data visually and in an algorithmic manner it was necessary to scale the all the data in the same domain and to synchronize the power spectrum sampling rate. The chosen domain for scaling was [0, 1], the choice being arbitrary without any special meaning; the sampling rate was chosen to be the highest in the data set.

2.2. Techniques for Exploring the Data Set

The visual exploration of the data set is very important and needs to be realized in collaboration with a human expert. A strategy needs to be established in order to present the data in manner that is concise, easy to understand and representative for the aspects that need to be analyzed. Also after analysis it is possible to determine the direction that has to be followed for the algorithmic analysis of the data.

For the study regarding the possibility of implementation of a quality evaluation system through the sound pattern obtained through non-destructive percussion the following aspects have to be studied.

a) *The Homogeneity of the Data Set is Good Enough in Order to Observe Common Characteristics for the 100 Recordings of One Item of the Data Sets*

In order to answer this questions the approximately 100 recordings of each sample have been represented in graphical form in two dimensions using a color code for intensity, the ordinate for the number of the recording [1:100] and the abscissa for the frequency [250Hz:11000Hz].

In Fig. 4 the least favorable case encountered in the data set is presented. As it can be observed, there is an important dispersion of the maxima, but in the same time a specific pattern can be distinguished. This pattern is more clearly highlighted in Fig. 6 where on the abscissa there is the frequency [250Hz:11000Hz] and on the ordinate there is the sum of the power spectrum of all the 100 recordings for the sample. As a comparison in Fig. 5 and Fig. 7 the same representations are presented that can be considered as typical for the data set.

b) *Are There Common Characteristics for all the Samples in the Data Set?*

In order to answer to this question it is needed to calculate the median of the power spectrum of all the samples in the data base. This is presented in Fig. 8. From the figure it can be observed that there are common frequencies around 6200Hz, 8000Hz and 10650Hz. The most important maxima being at the frequency of 8000Hz. These common frequencies represent an error source for discriminating among the different quality grades. This error is maximum for the sample burned at 600°C having 113mm, where these maxima common for all the samples overlap the specific maxima for this given sample. Because of this overlapping we cannot filter the entire set to eliminate these common maxima.

c) *Are There Common Characteristics for Samples Burned at the Same Temperature for all Shapes and Sizes?*

This question can be answered by comparing the power spectrum of the samples burned at the same temperature and having different length.

In order to clearly put into evidence these common characteristics, two representations were used. The first one has on the ordinate the length of the sample and on the abscissa the frequency in the domain of [250Hz:11000Hz], the grayscale lighting representing the value of the power spectrum at the given frequency. The second representation overlaps the power spectrums using different colors for different samples. Analyzing these representations it can be observed that the only common frequencies that we can highlight using an algorithm in a robust manner would be the frequencies that were presented in the previous section as being common to

all the samples in the data set. Thus it can be stated that by analyzing the sound pattern at non-destructive percussion in the domain of [250Hz:11000Hz] it is not possible to highlight characteristics specific to the burning temperature without regard to the shape and size of the product.

In Fig. 9 the comparative spectrum for the samples burned at 970°C having the lengths of: 75mm, 113mm and 197mm is presented. Besides the maximums in the vicinity of 8kHz and 10.6kHz which are common to all the samples there is also a slight overlapping near 3kHz for the samples having 113mm and 197mm but for the sample having 75mm there is no maximum in this vicinity.

The above shown figures prove that it is possible to distinguish between products having the same shape and size burned at different temperatures, and thus having different quality grades. It is however likely to have in isolated cases classification errors as a result of the overlapping of some sample characteristic maxima with maxima common to all samples. The phenomenon is most probably generated by limitations in the sound production and recording. More specific, the percussion instrument will produce its own characteristic spectra and the microphone might also work as an antenna and capture some electromagnetic noise in the frequency domain of the sound waves that are analyzed. All these perturbations will however be of relatively low amplitude, thus their influence on the sound pattern will be significantly lower than the influence of the characteristic spectra.

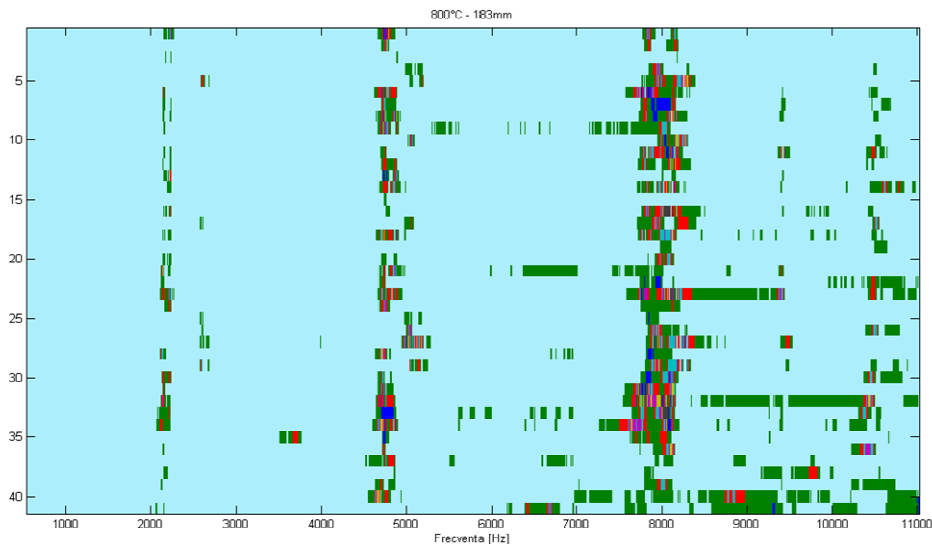


Fig. 4 – The power spectrum for individual percussions for the sample burned at 800°C having a length of 183mm.

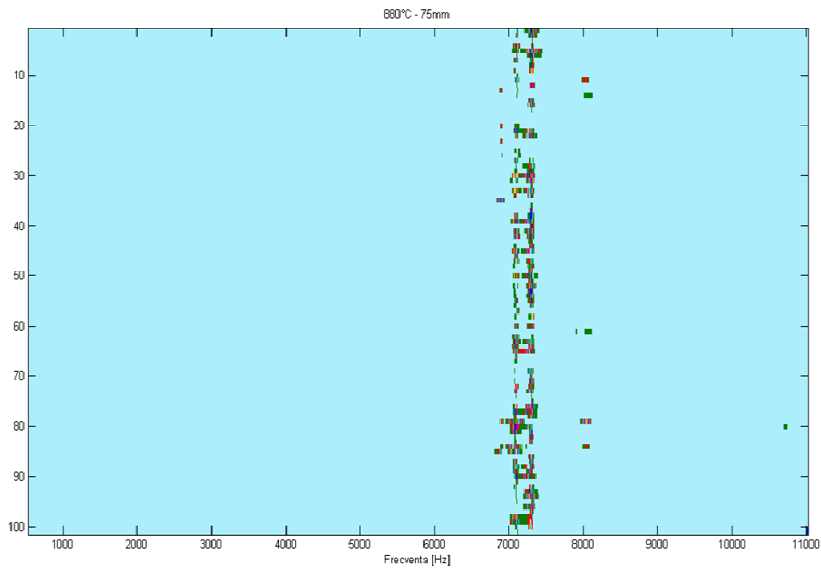


Fig. 5 – The power spectrum for individual percussions for the sample burned at 880°C having a length of 75mm.

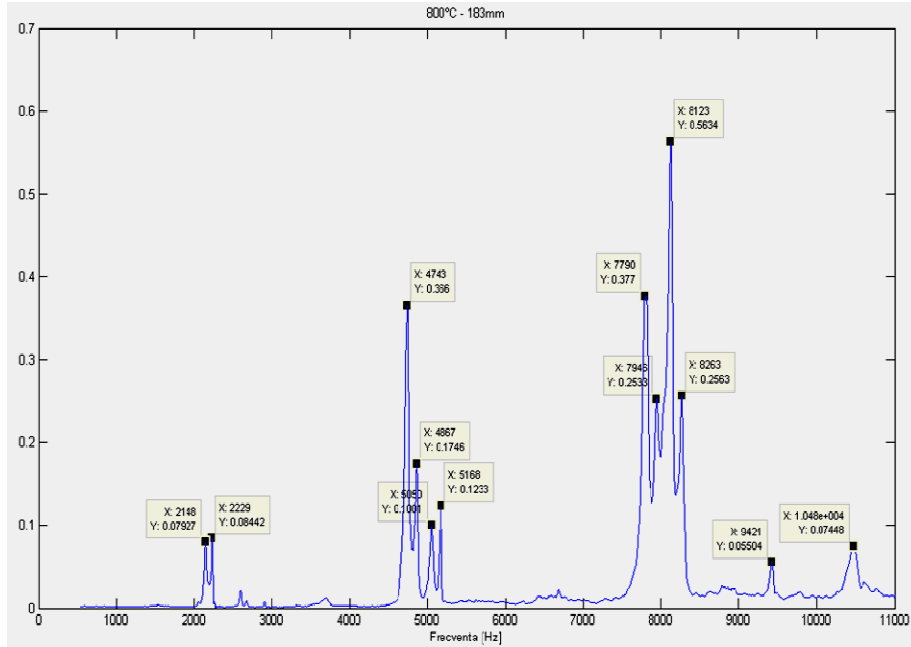


Fig. 6 – The sum of the power spectrum of all the recordings made for the sample burned at 800°C having the length of 183mm.

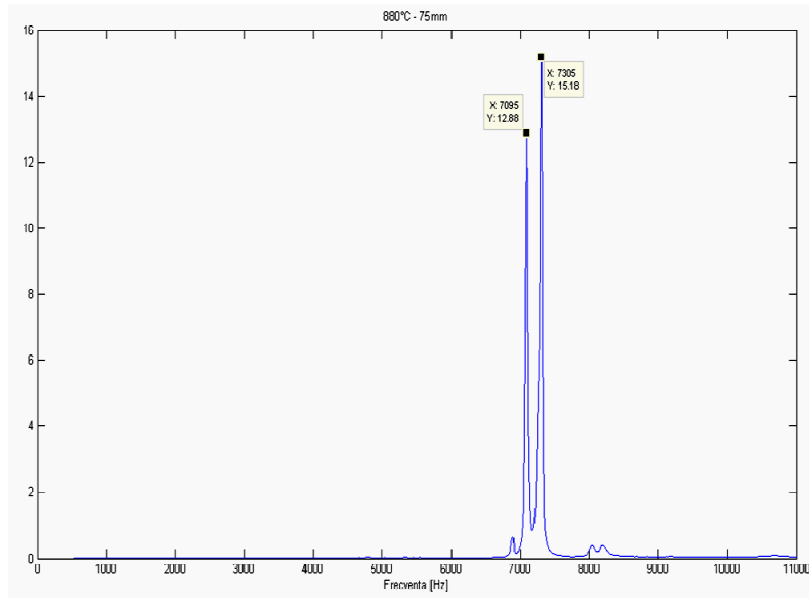


Fig. 7 – The sum of the power spectrum of all the recordings made for the sample burned at 880°C having the length of 75mm.

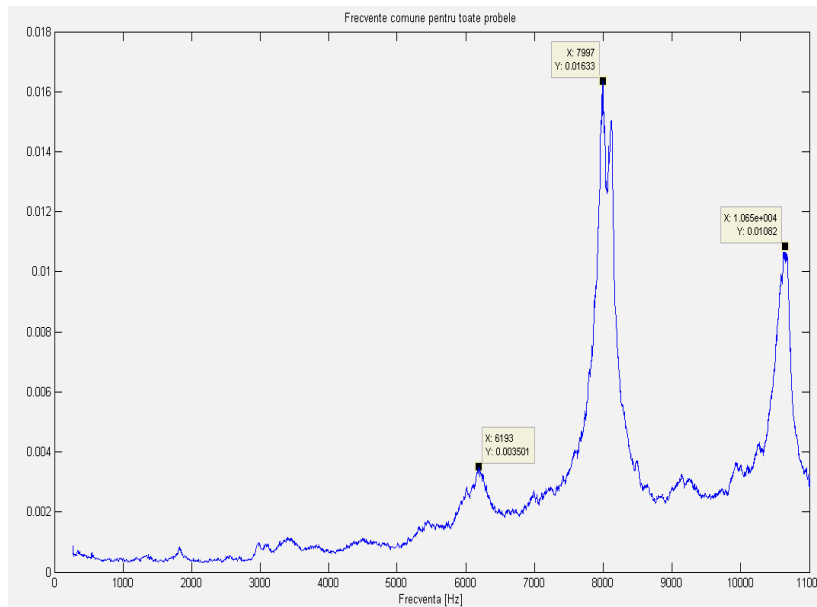


Fig. 8 – Common frequencies for all the samples in the data set highlighted by calculating the median values of the power spectrums of every sample for each frequency point.

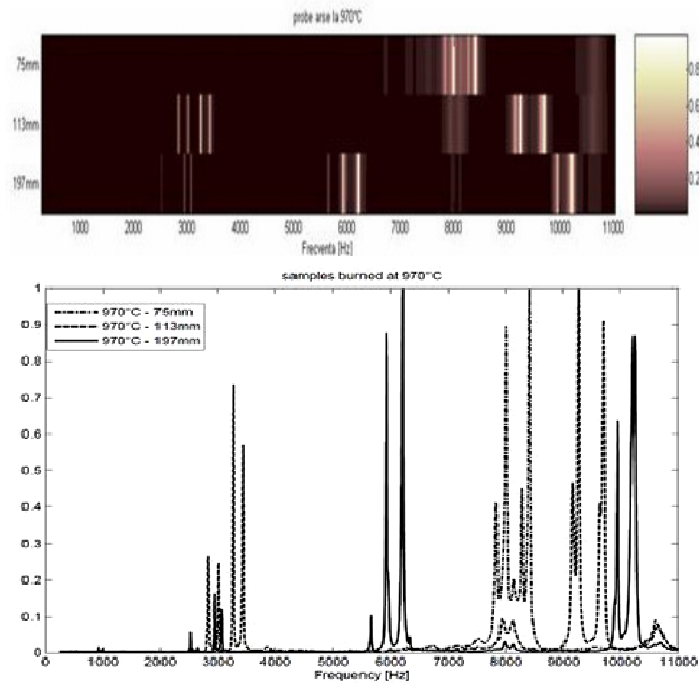


Fig. 9 – Comparative spectra for samples burned at the same temperature 970°C but having different lengths: 75mm, 113mm si 197mm.

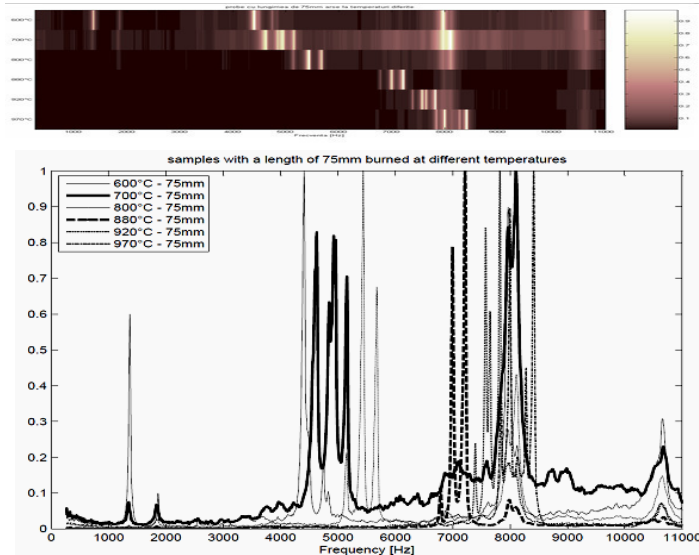


Fig. 10 – The compared spectra for samples with the dimensions of $\Phi 8 \times 75$ mm burned at: 600°C, 700°C, 800°C, 880°C, 920°C and 970°C.

2. Conclusions

As a result of visual data exploration it can be said that regarding the possibility to evaluate the ceramic products quality by using the sound pattern recorded at non-destructive percussion it is not possible to distinguish common characteristics of the power spectrum for products burned at the same temperature that have different shape and/or size.

It is however possible to evaluate the quality grade for products that have a given shape and size. In this case it is possible to improve the classification accuracy by choosing a low number of quality grades to be distinguished among (a maximum of 6 quality grades would give good results). Also improvements in the classification accuracy can be obtained by improving the quality of the sound recording system and choosing an appropriate percussion instrument.

Received: May 14, 2010

University "Dunărea de Jos" of Galați,
Department of Materials Science
e-mail: tpotecasu@gmail.com

REFERENCES

1. Dumitriu Luminița, *Achiziția de cunoștinț.* Edit. Did. și Ped., București, 2003.
2. Hand David, Mannila Heikki, Smyth Padhraic, *Principles of Data Mining.* The MIT Press, Cambridge, Massachusetts, 2001.
3. Witten I.H., Frank E., *Data Mining Practical Machine Learning Tools and Techniques.* Sec. Ed., Morgan Kaufmann Publ., San Francisco, CA, 2005.
4. Renevey P., *Speech Recognition In Noisy Conditions Using Missing Feature Approach.* Thèse présentée au département d'électricité, Lausanne, epfl, (2000).
5. Bengtsson T., *Speech Recognition Using Multilayer Perceptron Artificial Neural Network.* Dept. of Computer Sci., Lund University.
6. http://en.wikipedia.org/wiki/Ceramic_materials - online encyclopedia, Ceramic materials section.
7. <http://en.wikipedia.org/wiki/Wav> - online encyclopedia, .wav file format section.
8. <http://en.wikipedia.org/wiki/Fft> - online encyclopedia, FFT algorithm section.
9. * * *Enciclopedia de chimie.* Vol 2, Edit. Șt. și Enciclop., București, 1986.

SISTEM ACUSTIC DE CONTROL AL CALITĂȚII PRODUSELOR CERAMICE

(Rezumat)

În lucrarea de față autorii au studiat posibilitățile de implementare ale unui sistem de evaluare a calității direct pe linia de producție a produselor ceramice și

limitele unui astfel de sistem. Sistemul propus se bazează pe tehnici specifice data mining pentru analizarea sunetului produs de produsele ceramice la lovire nedistructivă.

Studiile au arătat că se pot obține rezultate bune în ceea ce privește clasificarea pe grupe calitative diferite pentru produse cu formă și dimensiuni cunoscute chiar și atunci când se lucrează cu șase grupe calitative distincte. Reducerea numărului de grupe calitative în care trebuie încadrat produsul analizat are ca rezultat creșterea preciziei de clasare. În industrie numărul de grade calitative pentru un produs în general nu va fi mai mare de trei, astfel autorii consideră ca metoda propusă este potrivită pentru utilizarea în industrie.

CYCLING EFFECTS ON MARTENSITE REVERSION IN Cu-BASED SMAs

BY

**BOGDAN PRICOP, NICOLETA-MONICA LOHAN (MAHU)
and LEANDRU GHEORGHE BUJOREANU**

Abstract. For this experiment, from a hot rolled water quenched Cu-15 Zn-6 Al (mass. %) SMA three fragment was cut and, after careful mechanical removal under water cooling of any marks of superficial corrosion, it was subjected to two, three and five series of thermal cycles up to 453K with a heating rate $1.67 \times 10^{-1} \text{ K} \cdot \text{sec}^{-1}$, isothermal maintaining for 180 sec and a cooling rate of $8.33 \times 10^{-2} \text{ K} \cdot \text{sec}^{-1}$. In all cases, during heating, an endothermic peak was observed corresponding to martensite reversion to parent phase. The DSC charts were analyzed with Proteus software.

Key words: shape memory alloys, differential scanning calorimetry.

1. Introduction

Cu-based shape memory alloys (SMAs) have been studied since 1970 by L. Delaey [1] and since then they have become commercially available. Cu-Zn-Al alloys are derived from Cu-Zn, some of the old shape memory alloys [2]. Among the commercial shape memory alloys (SMA) [1] the Cu-Zn-Al (a Cu-based alloy) is ranked after Ni-Ti because relatively low cost and good electrical and thermal conductivity, higher high ductility than NiTi, and resistance to intergranular fracture [3]. Consequently some industrial applications have been developed such as high work-output thermal actuators [4] or hydraulic and electric couplings [5], or fastening device [3]. Given the good properties of CuZn alloys, they were used to obtain electric actuators [6], heat engines [7], anti-seismic dampers [8] or high temperature applications [9].

In spite of the promising development perspectives as constrained-recovery

or work-generating applications, the use Cu-Zn-Al SMAs has been hindered by a series of drawbacks caused by metallurgical processing [10], training [11] and cycling [12]. Thermal fatigue was reported to be the primary cause for the change of critical temperatures for reverse martensitic transformation. As a result, the degradation of shape memory effect (SME) was noticed in Cu-Zn-Al which was ascribed to the high temperature stabilization of martensite [13]. Considering that, under such cycling conditions, the direct and reverse martensitic transformations occur in different ways and often even the thermal cycling range is varied, a gradual depreciation of thermal memory behavior is expected to occur. Therefore, the present paper aims to monitor the evolution of a Cu-Zn-Al SMA during thermal cycling comprising controlled heating.

Several experimental techniques are used in characterizing the reversible martensitic transformation which governs SM phenomena in alloys [14]. Between them, the calorimetry enables one of the easiest and most accurate determinations of transformation temperatures and energy dissipation [15].

2. Experimental Procedure

From plates of Cu-15 Zn-6 Al (mass.%) SMA obtained via casting - hot rolling - instant water quenching [16-18] three small fragment were cut and, after careful mechanical removal under water cooling of any marks of superficial corrosion, it was subjected to two, three and five thermal cycles. The samples were heated to 453 K using a NETZSCH differential scanning calorimeter type DSC 200 F3 Maia was used (found in to laboratory SIM-TM-06 from Department of Materials Engineering and Industrial Safety, Faculty Materials Science and Engineering). A technical specification of DSC F3 Maia is: sensitivity: $< 1\mu\text{W}$, temperature accuracy: 0.1 K and enthalpy accuracy: generally $< 1\%$. The device was calibrated with Bi, In, Sn and Zn standards.



Fig. 1 – Calorimeter DSC F3 Maia.

Each thermal cycle comprised: (1) heating, with $1.67 \times 10^{-1} \text{ K} \cdot \text{sec}^{-1}$; (2) isothermal maintaining for 180 sec and (3) cooling to 300 K with a cooling rate of $8.33 \times 10^{-2} \text{ K} \cdot \text{sec}^{-1}$. In all cases, the first heating was accompanied by an endothermic peak on DSC charts associated with martensite reversion to parent phase. Subsequent cooling enabled the return to the same thermally induced martensitic structure. The measurements were performed under Ar protective atmosphere using corresponding correction to 570 K. Since no cooling stage was attached to the DSC device, it was able to provide a controlled cooling rate only very briefly at the beginning of cooling.

3. Results and Discussion

The DSC charts illustrating the calorimetric evolution of the specimen during the heating stages. It is noticeable that an endothermic peak occurs during first heating suggesting that the specimen in initial state contains a large amount of thermally induced martensite, which reversibly transforms to parent phase (austenite) [19].

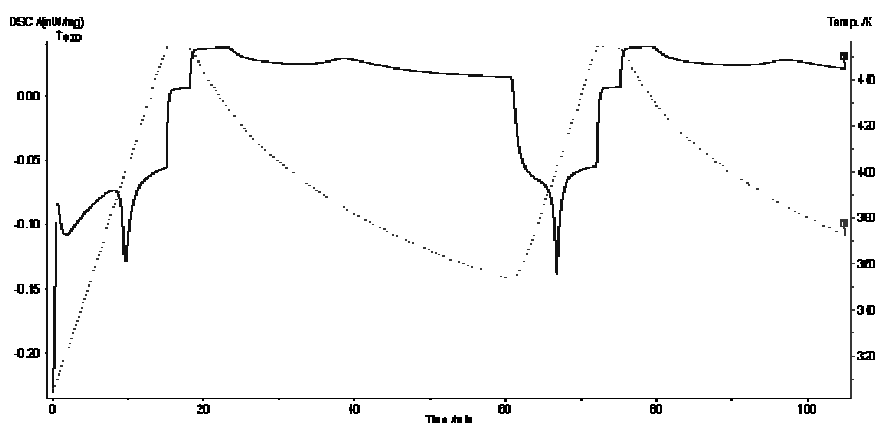


Fig. 2 – DSC charts for two thermal cycles.

The Table 1 summarizes the results obtained via PROTEUS from the experimental series of measurements. According to data evaluation results given by Proteus, reverse martensitic specific the first sample (Fig.2), the first transformation occurs during first heating at $A_s=394.9 \text{ K}$, reaches maximum transformation rate and 50 % of transformed phase at $A_{50}=399.7 \text{ K}$ and ends at $A_f=407.6 \text{ K}$, and for a two heating starts $A_s=397.2 \text{ K}$, maximum transformation is $A_{50}=401.2 \text{ K}$ and ends at $A_f=406.6 \text{ K}$.

After two cycling, A_{50} increases with 1.5 K and specific enthalpy decreases with 7%. When the sample cycle three times (Fig. 3), retainer's tendency to peak two to move to higher temperature.

Table 1
Summary of Data Evaluation with Proteus Software

Number of cycles	Sample mass, 10^{-6} kg	Tangent method		A_{50} K	$\Delta H / m$ kJ/kg	dT/dt	
		A_s K	A_f K			Heating [K/sec]	Cooling [K/sec]
2	40.8	394.9	407.6	399.7	-3.870	1.67×10^{-1}	8.33×10^{-2}
		397.2	406.6	401.2	-3.628		
3	57.3	393.3	404.4	397.8	-5.157	1.67×10^{-1}	8.33×10^{-2}
		398.0	406.3	402.1	-4.945		
		397.8	405.8	401.9	-4.922		
5	45.1	393.0	402.1	396.7	-5.283	1.67×10^{-1}	8.33×10^{-2}
		398.0	405.0	401.2	-5.953		
		398.0	405.0	401.2	-5.724		
		398.1	404.7	401.1	-5.267		
		397.9	404.6	401.0	-5.224		

During the third heating, starts and end temperatures of transformation decreases.

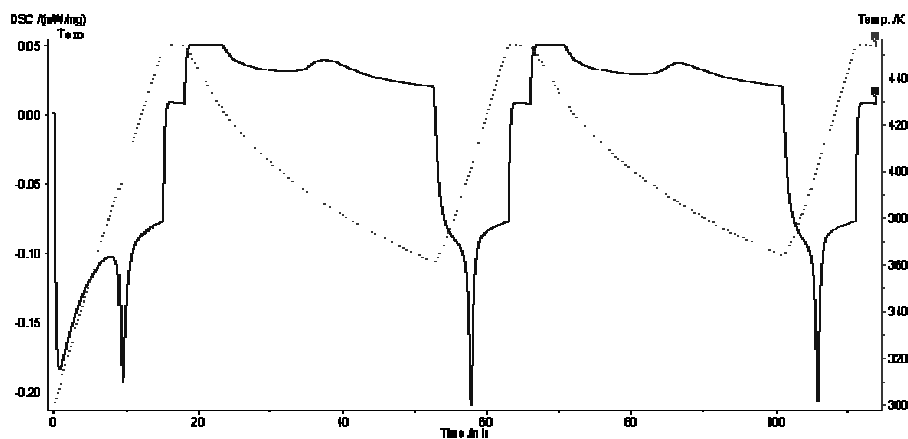


Fig. 3 – DSC charts for three thermal cycles.

The sample cycle five times keep the same trend of moving sites peak at higher temperatures in cycle two, three and four, followed by the last heating they decreases. These observations are confirmed by the values listed in Table 1. From Table 1 observed after five heating A_s decreases with 4.9K and A_f with 2.5K.

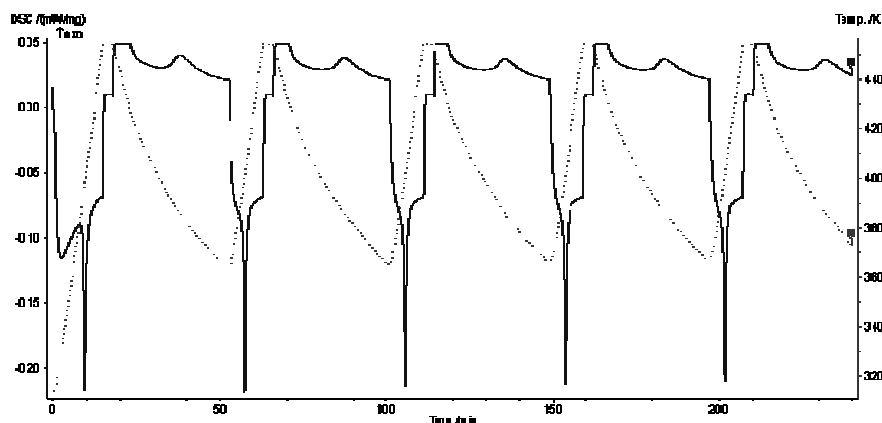


Fig. 4 – DSC charts for five thermal cycles.

Also is obvious a decrease in peak intensity. Two main causes could be the origin of this degradation of thermal memory cause by thermal cycling: the lack of thermally induced martensite or the formation of stabilized martensite.

3. Conclusion

A hot-rolled water quenched Cu-15 Zn-6 Al (mass. %) SMA, with self-accommodated thermoelastic martensite structure, experienced cyclic reversion to austenite during two, three and five series of consecutive thermal cyclings, comprising controlled heating up to 453K, with a heating rate $1.67 \times 10^{-1} \text{ K} \cdot \text{sec}^{-1}$ isothermal maintaining for 180 sec and a cooling rate of $8.33 \times 10^{-2} \text{ K} \cdot \text{sec}^{-1}$.

The peaks are changed in two manners during thermal cycling: 1 - they tend to move to larger temperatures and to increase in intensity during the second cycling series and 2 - they tend to move to lower temperatures and to become less intense, up to total extinction, during the third and fifth cycling series.

A c k n o w l e d g e m e n t. This paper was realised with the support of EURODOC “Doctoral Scholarships for research performance at European level” project, financed by the European Social Found and Romanian Government.

Received: May 14, 2010

“Gheorghe Asachi” Technical University of Iași,
Department of Materials Science and Engineering
e-mail: monica.lohan@yahoo.com

REFERENCES

1. Khan AQ, Delaey L., *Martensite-Plate-Size Dependence of Yield Strength of Copper-Aluminium-Zinc Martensite*. Scripta Metall, **4**, 12, 981-987 (1970).
2. Bujoreanu L.G., *Materiale Inteligente*, Edit. Junimea, Iași, 48, 2002.
3. Kumar P.K., Lagoudas D.C., *Introduction to Shape Memory Alloys, Shape Memory Alloys. Modeling and Engineering Applications*. Edit. Springer, New York, 1-51, 2008.
4. Tautzenberger P., *Thermal Actuators: A Comparison of Shape Memory Alloys with Thermostatic Bimetals and Wax Actuators, Engineering Aspects of Shape Memory Alloys*. Melton K.N., Stöckel D., Wayman C.M. (Eds.), Butterworth-Heinemann, Oxford, 207-218 (1990).
5. Duerig T.W., Melton K.N., Proft J.L., *Wide Hysteresis Shape Memory Alloys, Engineering Aspects of Shape Memory Alloys*. Duerig T.W., Melton K.N., Stöckel D., Wayman C.M. (Eds.), Butterworth-Heinemann, Oxford, 130-136 (1990).
6. Bujoreanu L.G., Stanciu S., Enache A., Lohan C., Rusu I., *Influence of Some Extrinsic Factors on the Two Way Shape Memory Effect of Electric Actuators*. J. Optoelectron. Adv. M., **10**, 3, 602-606 (2008).
7. Delaey L., Smeesters J., *Discussion to Paper 31, Shape Memory Effects in Alloys*. J. Perkins, Edit. Plenum Press, New York, 577-578 (1975).
8. Si Nai-chao, Sun Ke-qing, Sun Shao-chun, Liu Hai-xia, *Damping Performance of Cu-Zn-Al Shape Memory Alloys in Engineering Structures*. J. Cent. South Univ. Technol., **11**, 246-251 (2004).
9. Guilemany J.M., Fernandez J., Franch R., Benedetti A.V., Adorno A.T., *A New Cu-Based SMA With Extremely High Martensitic-Transformation Temperatures*. J. Phys., **IV**, C2, 361-365 (1995).
10. Franz M., Hornbogen E., *Martensitic Transformation of a CuZnAl-Shape Memory Alloy Strengthened by Hot-Rolling*. Mater. Sci. Engng., **A**, 252, 157-165 (1999).
11. Lovey F.C., Torra V., *Shape Memory in Cu-Based Alloys: Phenomenological Behavior at the Mesoscale Level and Interaction of Martensitic Transformation with Structural Defects in Cu-Zn-Al*. Prog. Mater. Sci., **44**, 189-289 (1999).
12. Sade M., Damiani C., Gastien R., Lovey F.C., Malaria J., Yawni A., *Fatigue and Martensitic Transitions in Cu-Zn-Al and Cu-Al-Ni Single Crystals: Mechanical Behaviour, Defects and Diffusive Phenomena*. Smart Mater. Struct., **16**, 126-136 (2007).
13. Bhuniya A.K., Chattopadhyay P.P., Data S., Banerjee M.K., *On the Degradation of Shape Memory Effect in Trace Ti-Added Cu-Zn-Al Alloy*. Mater. Sci. Engng., **A**, 393, 125-132 (2005).
14. Harrison J.D., *Measurable Changes Concomitant with the Shape Memory Effect Transformation*. In: Duerig T.W., Melton K.N., Stöckel D., Wayman C.M. (Eds.), *Engng. Aspects of Shape Memory Alloys*, Butterworth-Heinemann, Oxford, 106-111 (1990).

15. De Jonghe W., De Baptist R., Delaey L., De Bonte M., *Internal Friction Measurements on Copper-Zinc Based Martensite*. In: Perkins J. (Edt.), *Shape Memory Effects in Alloys*, Plenum Press, New York, 451-466 (1975).
16. Bujoreanu L.G., *On the Influence of Austenitization on the Morphology of α -Phase in Tempered Cu-Zn-Al Shape Memory Alloys*. Mater. Sci. Engng., **A**, 481-482, 395-403 (2008).
17. Bujoreanu L.G., Craus ML, Rusu I, Stanciu S, Sutiman D., *On the β to α -Phase Transformation in a Cu-Zn-Al-Based Shape Memory Alloy*. J Alloys Compd., 278, 190-193 (1998).
18. Bujoreanu L.G., Craus M.L., Stanciu S., Dia V., *Thermally and Stress Induced Changes in Three Structure of Cu-Zn-Al-Fe Shape Memory Alloy*. Mater. Sci. Technol., 16, 612-616 (2000).
19. Spielfield J., *Marforming and Martempering of a Cu-Zn-Al Shape Memory Alloy*. Mater. Sci. Engng., **A**, 273-275, 639-643 (1999).

EFECTELE CICLĂRII ASUPRA REVERSIEI MARTENSITEI ÎN AMF PE BAZĂ DE Cu

Pentru acest experiment dintr-o bară de aliaj cu memoria formei pe bază de Cu au fost tăiate 3 fragmente și supuse încălzirii cu ajutorul unui calorimetru cu scanare diferențială DSC F3 Maia. După ce probele au fost șlefuite pentru a îndepărta orice urmă de impuritate, acestea au fost încălzite până la temperatura de 453K cu o viteză de încălzire de $1.67 \times 10^{-1} \text{ K} \cdot \text{sec}^{-1}$ și supuse ciclărilor termice după cum urmează: prima probă a fost supusă la două cicluri termice, a doua probă a fost supusă la trei cicluri termice iar ultima la cinci cicluri termice. În toate cazurile, în timpul încălzirii a fost observat un peak endotermic care corespunde reversiei martensitei. Graficele DSC au fost analizate cu software-ul Proteus.

PREPARATION OF PROSTHETIC IMPLANTS RESEARCH

BY

EMANUELA-DANIELA STOICA

Abstract. Electrochemically hydroxyapatite coating can be a good cover for implants if it is found a perfect combination of parameters during the producing process.

Key words: hydroxyapatite, titanium substrate, dissolution, electrodeposition.

1. Introduction

Over the years research has been conducted for the purpose of finding a methods bone replacement Metallic biomaterials have increasingly gained ground because of their special properties used to make ortopedic, dentare as well as neural and cardiovascular implants [1].

However, the lack of a full compatibility with the physiological environment, the corrosion susceptibility, mechanical properties with the skeletal properties make that these metallic biomaterials to be used like substrate covered with various ceramics that complete disadvantages above. Titanium has the advantage of passivation being able to acquire a TiO_2 layer [2].

The purpose of this project is to prepare the surfaces before the electrochemical deposition of hydroxyapatite paying special attention to the influence of surface roughness on the hydroxyapatite layer. The present paper to improve the $\text{Ti}_6\text{Al}_4\text{V}$ alloy sublayer and in the implicitly the electrochemically deposited hydroxyapatite, as well as for test resistance of the hydroxyapatite deposited layer by dissolution in distilled water and phosphate buffer saline solution. All experiments has been conducted at Surface Engineering Laboratory Strasbourg, National Institute of Applied Sciences, Strasbourg, France (INSA Strasbourg, France).

2. Experimental

The method chosen was the electrochemical deposition, an inexpensive method of producing the hydroxyapatite. The sample preparation consists of the following steps: cutting, integration in “bakelita”, polishing (with abrasive paper between 600, 1200, 2400, 4000 granulation respectively), ultrasound cleaning, electrochemical pickling (using NaOH) [3]. All these steps are very important for a good quality of HAp deposition because each flaw or impurity of the surface can affect the hydroxyapatite layers morphology and/or mechanical properties. The surface morphology is a very important criterion. For the hydroxyapatite the following parameters have been used: Eliaz’s solution, temperature 90°C, no steering for 30 minutes, potential (-1mA), deposition time 1 h and 2 h and 3 h respectively, all parameters are constant throughout the process.

Hydroxyapatite dissolution in aqueous system is governed by the mass action law and concentration law. Hydroxyapatite dissolution can be performed both in distilled water and PBS -Cl, 0.6g KCl, 3.6g Na₂HPO₄, 0.6g KH₂PO₄-(physiological serum). Many inorganic biomaterials like HAp have been used as a biological model for mineralization and demineralization. Most studies claim that the dissolution is a spontaneous process which continues until the balance is reached or until all the phases solid disappear [4].

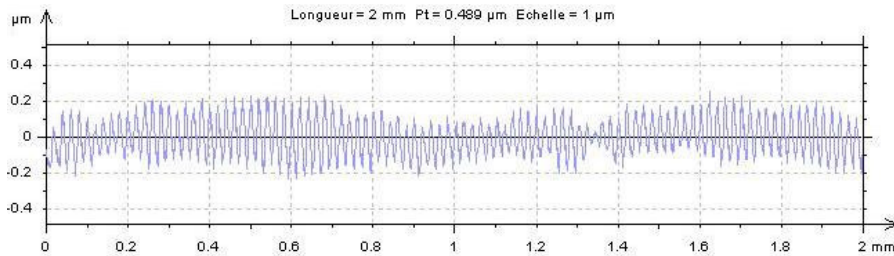
It is well known that crystallization is not spontaneous until nucleus or the displacement source from the crystal surface reaches a critical size or until conduction force (over the saturation) is big enough. Similarly, the hydroxyapatite dissolution is accompanied by hole formation in the area throughout all the stages of dissolution. When the size of the dissolved crystals approaches the critical value for the active holes, the dissolution may stop. Only holes that are larger than the critical size contribute to dissolution.

Morphology and growth of hydroxyapatite coating have been observed by Scanning Electron Microscope (Philips 30FEG Environnement). The chemical composition and hydroxyapatite crystals orientation have been studied with X-ray diffraction under grazing incidence [5]. Hydroxyapatite coating stability has been analyzed by dissolution in distilled water and phosphate buffer saline (PBS) for 1 hour and filing evidence 2 hour. Topographic studies were performed with profilometer (Logiciel Micromesure 2).

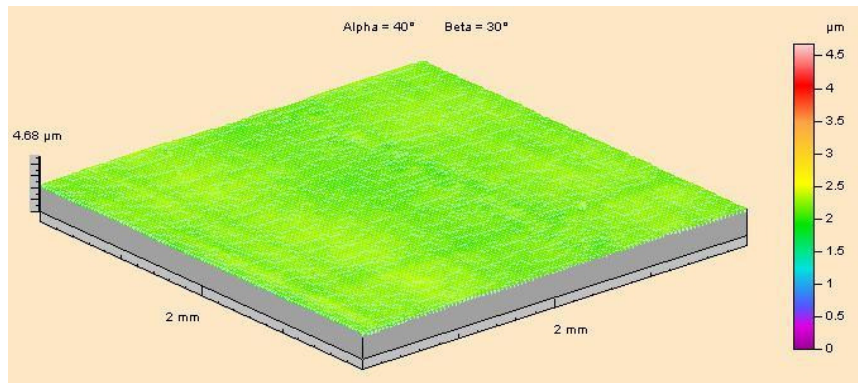
3. Results and Discussions

3.1. Before Dissolution Process

Both representations show that the surface is nearly smooth, without irregularities.

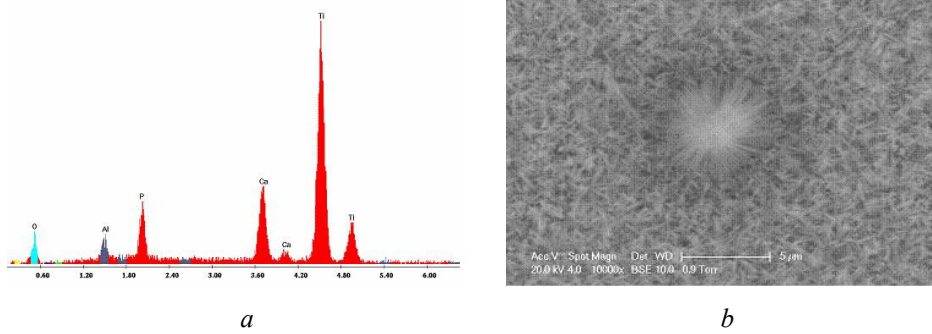


a



b

Fig. 1 – Ti alloy surface: *a* – 2D profile; *b* – 3D.



a

b

Fig. 2 – SEM analysis for 1h deposition sample: *a* – Chemical composition for 1h sample deposition; *b* – Sample section for 1 h.

The crystals had acicular shape. The 30 minutes without steering during the deposition process is cell growth time. Ratio Ca / P is 1.28 and Ti is present in big quantities. The deposition time is very short until the surface is fully cover with Ti alloy sublayer. After determining the quantity ratio of Ca/P

by EDX, the analysis shown that the report for hydroxyapatite is not the specific ratio of 1,67.

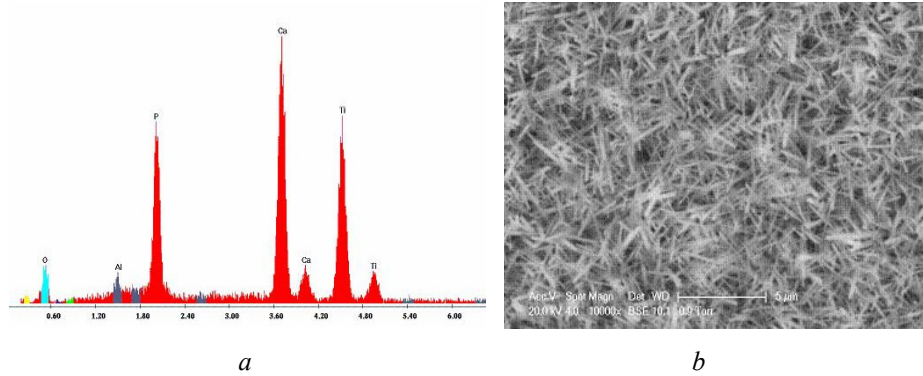


Fig. 3 – SEM analysis for 2h deposition sample: *a* – Chemical composition for 2h sample deposition; *b* – Sample section for 2 h.

3.2. After Dissolution Process

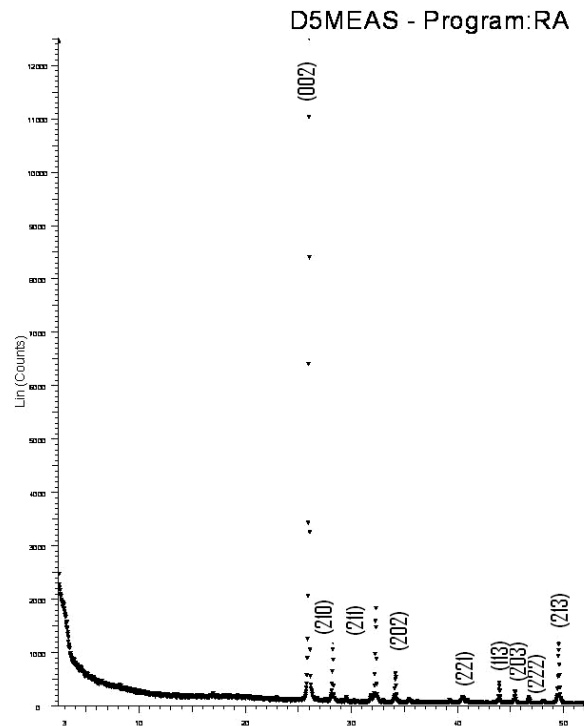


Fig. 4 – Sample after dissolution in phosphate buffer saline solution (SEM).

After 2h, deposition Ca and P quantity are important. Titanium sublayer is covered and the report Ca/P is 1.46. Forma crystal is needle with various orientations. After dissolution in water for seven days report the Ca/P 2.14.

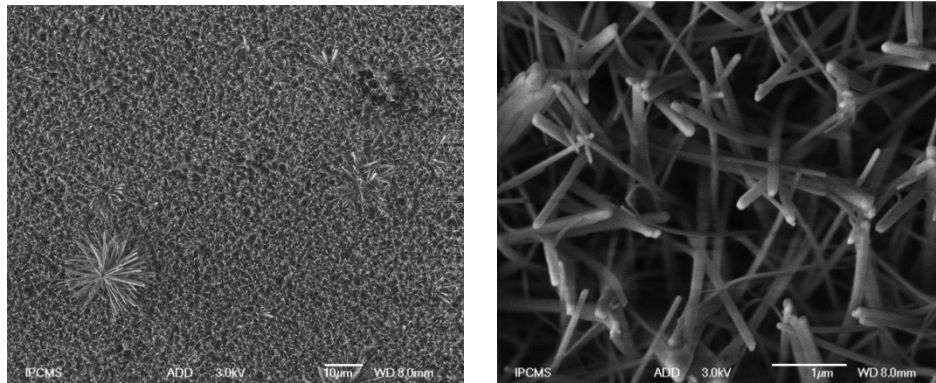


Fig. 5 – Sample after dissolution in distilled water.

The crystals have a needle shape and there are several flower-shaped crystals. Their different sizes and their tips are rounded. Orientation of the crystals is oblique or perpendicular. After dissolution, crystals can have perpendicular and inclined orientation. After a period of seven days dissolution in phosphate buffer saline, the Ca/P ratio is 2.29 higher compared with the dissolution sample in distilled water.

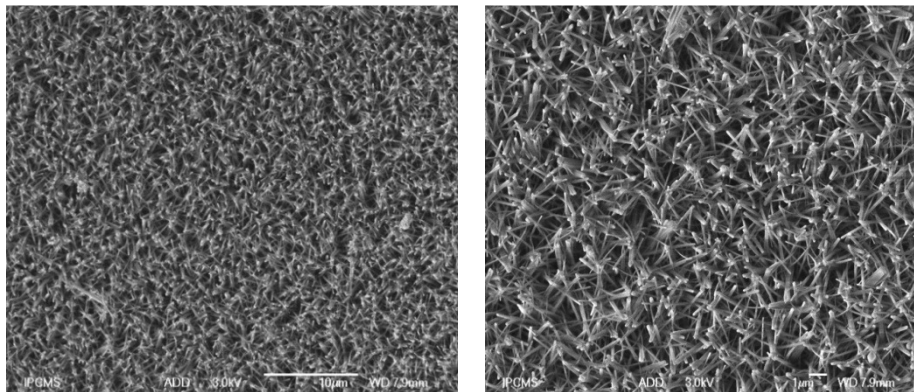
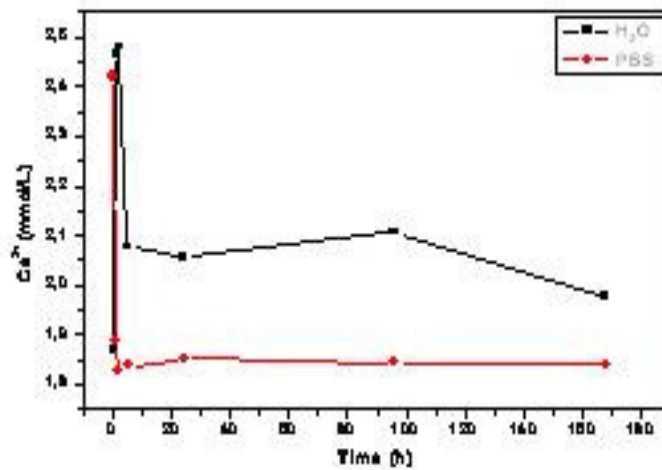


Fig. 6 – Sample after dissolution in phosphate solution.

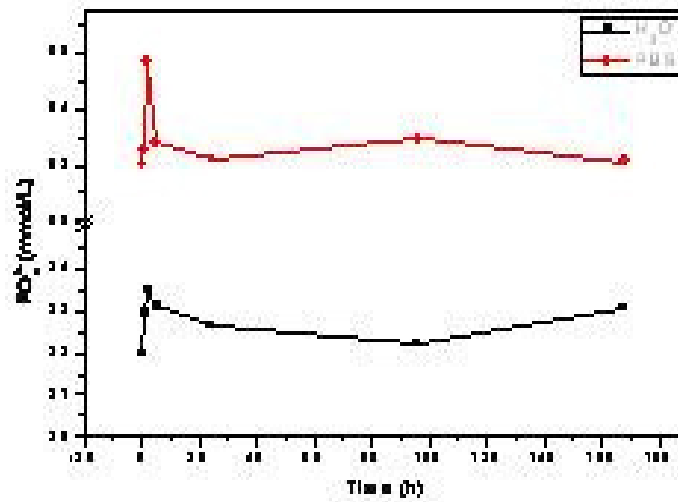
All crystals have a rounded shape with oblique and perpendicular orientation needle peaks. Contrary to distilled water sample dissolution, the dissolution sample in phosphate buffer saline solution does not submit drill

crystal flowers.

This study was performed with samples of phosphate buffer saline solution and distilled water each time set. It may be noted that both the amount of Ca^{2+} and PO_4^{3-} in the beginning is increased.



a



b

Fig. 7 – Ca^{2+} and PO_4^{3-} after dissolution in distilled water and phosphate buffer saline solution: *a* – Ca^{2+} Analysis; *b* – PO_4^{3-} analysis.

Followed by stagnation and then a reprecipitation. It can be said that two behaviors are similar. But small differences can be observed: in the figure a) the amount of calcium ions is slightly higher at a time close to 100 hours for dissolution in water while the dissolution in saline can letup; in figure b) representation around the same time the 100 hours amount of PO_4^{3-} is higher for saline solution while the amount of PO_4^{3-} in distilled water drops.

4. Conclusions

Electrochemical deposition is an available technique to achieve a uniform hydroxyapatite coating while having an ideal structure to cover the implant, if it can be found a perfect combination of parameters and the suitably roughness. Roughness has a large influence on the appearance, form and orientation of particles produced by deposition.

Hydroxyapatite obtained by electrochemical deposition is a distribution of crystals of "nails" and "petals". Obviously, there are treatment for reducing crystal size by "crushing" to get a structure that allows growth cell, but unfortunately this type of treatment increases the production cost of hydroxyapatite and also outgoings implant.

Received: May 14, 2010

Polytechnical University of București,
Department of Materials Science and Engineering
e-mail: stoicaemanueladaniela@yahoo.com

REFERENCES

1. Parker J.B., Bronzino J.D., *The Biomedical Engineering Handbook, 2nd ed Biomaterials Principles and Applications*. CRC Press, Boca Raton, FL, 1-21 (2000).
2. Ciobanu G., Carja G., Ciobanu O., *Structural Characterization of Hydroxyapatite layer Coatings on Titanium Supports*. Elsevier-Surface and Coatings Technol., **202**, 11, 2467-2470 (2008).
3. Dos Santos E.A, Moldovan M.S, *Oriented hydroxyapatite Single Crystals Produced by the Electrodeposition Method*. Mater. Sci. and Engng., **B**, *Bioinspired and Biointegrated Materials as New Frontiers Nanomaterials* (I). Symp. M of the 2009 E-MRS Spring Meeting Strasbourg, France, **169**, 1-3, June 8-12, 2009, 138-144 (2010).
4. Tang R. și al., *Size-Effects in the Dissolution of Hydroxyapatite: an Understanding of Biological Demineralization*. J. of Mater. Chem. (2004).
5. Geru N., *Structure Analysis of Metallic Materials*. Edit. Tehnică, București, 90, 1991.

CERCETARE PRIVIND PREGĂTIREA IMPLANTURILOR PROTETICE

(Rezumat)

În această lucrare a fost utilizat aliajul Ti6Al4V ca substrat pentru depunerea de hidroxiapatită pe cale electrochimică. S-au efectuat studii de soluție a hidroxiapatitei în apă distilată și soluție salină de fosfat. Aliajul de Ti₆Al₄V poate fi considerat aliajul biomedical standard. Obiectivul acestui proiect este focusat asupra pregătirii suprafețelor înainte de depunerea electrochimică a hidroxiapatitei în special influența rugozității asupra startului de hidroxiapatită. După depunerea de hidroxiapatită, probele au fost analizate cu difracție de raze X, analiză SEM, microscopie optică precum și înainte de depunere prin profilometrie și microscopie optică. Depunerile de hidroxiapatită realizate pe substratul de Ti₆Al₄V au fost realizate pentru protezele de șold.

WHAT IS SUBMITTED BY CHEMICAL VAPOR (C-CVD)?

BY

IRINA-ELENA SURDU and DAN-GELU GĂLUȘCĂ

Abstract: Analyzing the evolution process of chemical vapour deposition from the beginning until the present stage. Chemical vapour deposition (CVD) is a chemical process used to produce high-purity, high-performance solid materials. The process is often used in the semiconductor industry to produce thin films. In a typical CVD process, the wafer (substrate) is exposed to one or more volatile precursors, which react and/or decompose on the substrate surface to produce the desired deposit.

Key words: deposition, cvd, layers, gas mixt.

1. Definition and Purpose Type CVD Layers

The parts required to wear, for which lubrication is not possible or not recommended, and for heavy tools required to wear and corrosion, classical thermo chemical fail to obtain sufficient durability in exploitation of.

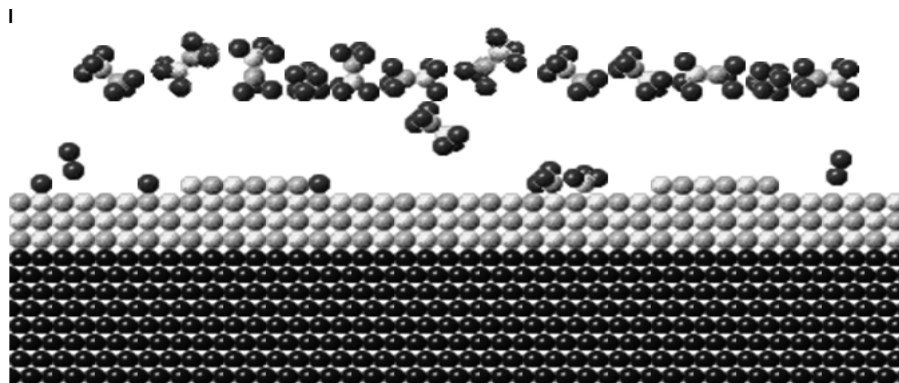


Fig. 1 – Chemical Vapour Deposition (CVD).

As a result, have developed a number of new active surface layers of protection against wear and corrosion applications for known CVD layer generic Chemical Vapor Deposition.

Chemical vapour deposition is a part of physical vapour deposit. The time difference between PVD and CVD was blurred due to the emergence of new technologies. Chemical vapour deposition include spraying, coating ion coating low pressure chemical vapour, laser coating, reactive evaporation, ion beam, laser evaporation and other variations.

2. Deposit CVD: Theoretical Principles

Variants differ by converting gas to reactive gas mixtures. In a CVD process reactant gas mixture contacts the part surface. The gases are heated to form a reactive gas mixture.

The coating is made of another material known as reactive vapours can be dispersed as solid or liquid gas. The gases are introduced into the chamber at normal pressure and temperature, while the solids and liquids at temperatures and high pressures. Inside the enclosure parts get energy to facilitate reaction with carrier gas.

The main stages in the CVD process are:

- the formation of reactive gas mixtures;
- the transport of reactant gas to the surface of the piece;
- the reactants absorption layer;
- the reaction to absorb the layer forming the deposit.

Surface treatment is very important Vapour Deposition and particularly CVD. Primary treatment involves the use of chemical and mechanical means before submission reactor parts.

The piece should be cleaned before submission and reactor chamber must also be clean, sealed, no dust and moisture. Cleaning is done with ultrasound and vapour degreasing to increase adherence with Vapour polishing is required.

During the coating process operators must maintain the area clean to prevent accumulation of particles. Manufacturers use acid or low concentration gas to clean the oxide layers that formed during the preheating.

Final treatment may include heat treatment to facilitate diffusion of coating material. Companies use CVD for corrosion resistance and wear. CVD is used mainly to obtain specific properties that are difficult to obtain by other processes. CVD process is important because the ability to control the microstructure of the material stored.

Microstructure CVD deposits depends on the chemical mixture, the energy of atoms, ions or molecular fragment, chemical properties of the surface, the surface of the piece, temperature part, the presence or absence of a current play. The metals used are: Ni, W, Cr, Ti carbide.

Firms also use CVD to create films, coatings, powders, composite materials, bodies, spherical particles, filaments and whiskers. Most applications are in electronics, optics, Optoelectronic, photovoltaic and chemical industry. Starting costs are high.

Technology for obtaining such layers on the metal surface consists in passing over this area, heated in a watertight enclosure relatively radiates temperatures, a reactant gas mixture, which contains the chemical elements of the layer in the form of volatile chemicals.

In the role of protective layers to wear, the gas mixture generally confines vapours of a volatile campus of a transition metal. This chemical compound is usually a metal halide that, playing the role of donor metal.

The complete chemical reactions that occur at process temperatures between donors (donors) of metal, gas mixture and other metal parts inside the area on the surface precipitation type layer CVD.

Regarding the nature of type CVD layers, they can be made of pure metals or their compounds harsh, such as carbides, nitrides, borides or oxides. CVD layers are compounds that make up metal type - non-metals, characterized by hardness and/or refractory high.

Precipitation layer of CVD gas mixture inside the normal pressure can occur (rarely) or subatmospheric pressure (usually vacuum field coarse or fine). In most CVD processes, maintaining temperature at which the growth layer is set within the area 900 - 1100°C, but there are processes that occur later in lower temperatures (500 to 700°C).

In CVD processes, diffusion phenomena at the interface layer-based material are reduced in weight, they are manifested mainly by finding some of the alloying elements of the basic material in the layer. Therefore, it is believed that CVD layers are layers of additive.

In this area we are using the term originating from the galvanic deposition technique. Thus, the process for obtaining layer is often called filing or CVD coating and parts to cover are called substrates.

3. Procedures for Obtaining Layers CVD

The principles of process to obtain high-temperature CVD layers.

In chronological order, first appeared was the CVD process which takes place at high temperatures, the process is named HT - CVD (High Temperature Chemical Vapour Deposition). As the CVD layers used for protection against wear than are those consisting of carbides, nitrides and cabinetries of titanium, the conduct of trials in HT-CVD process will be exemplified below for CVD layers of this type.

General reaction which occurs in HT-CVD processes can be written as:



where:

Me = transition metal, respectively (in this case titanium)

X = halogen (Cl, I, Br, etc.).

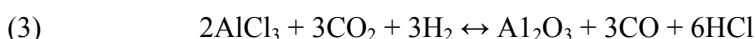
n, x, y, z, w = index chemical compound of the formula that (carbide, nitride, boride or oxide).

Donors non-metal consists of a gaseous compound or a mixture of gases, which assigns appropriate non-metallic layer formation (nitrogen for nitrides, carbon carbide, etc.). Donors of metalloids used more frequently in the HT-CVD techniques are CmHn gaseous hydrocarbons (mainly methane CH₄), molecular nitrogen N₂, carbon monoxide CO, carbon dioxide CO₂, etc. BCl₃ boron trichloride.

If the layer is formed only by titanium carbide, the general reaction (1) becomes:



The reaction occurs at temperatures above 1000°C, in atmosphere with excess hydrogen. It is likely that this high-temperature reaction as:



which justify the beneficial effect of excess H₂ on reaction kinetics. Apparent from these reactions result in a reaction product corrosive hydrochloric acid. Moreover, in almost all CVD processes also result corrosive nature-products, such as halogenated acids and chlorides. This installation requires execution components of filing of stainless materials and neutralization of exhaust gases from the process.

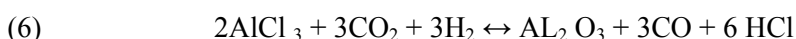
Customizing reaction (1) to obtain layers of nitrides, titanium carbide respectively, becomes:



to deposit layers of aluminium oxide, the reaction is:



As you can see, all these reactions, hydrogen plays an important role. In addition to chemical reactions between metal halides and gaseous compounds with non-metal role of donors in CVD processes is involved in other types of chemical reactions:



a) Reactions of thermal decomposition (pyrolysis)

In this case, a gaseous compound, unstable temperature deposit, decays. Such reactions may occur as side effects or even the main reactions of submission. One example is the deposition of carbon by methane decomposition at temperatures above 1000°C:



b) Reactions with hydrogen reduction. This is to reduce the metal halide with hydrogen at high temperatures. They are used for CVD deposition of layers consisting of pure metals (Ti, Ta, W, Zr). One example is the deposition of Ti by the reaction:



c) Oxidation reactions

Generally occur between volatile compounds of a metal which is deposited and an oxidizing compound nature (O_2 , CO_2 , etc.). Getting silicon oxide layers from silane is typical for this kind of reaction:



The reactions described above take place in sealed enclosures (wall reaction tubes warm or cold wall), in which production processes of heat and mass transfer specific CVD technology. The complete process takes place in different areas in relation to the play area, presented schematically in Fig. 2.

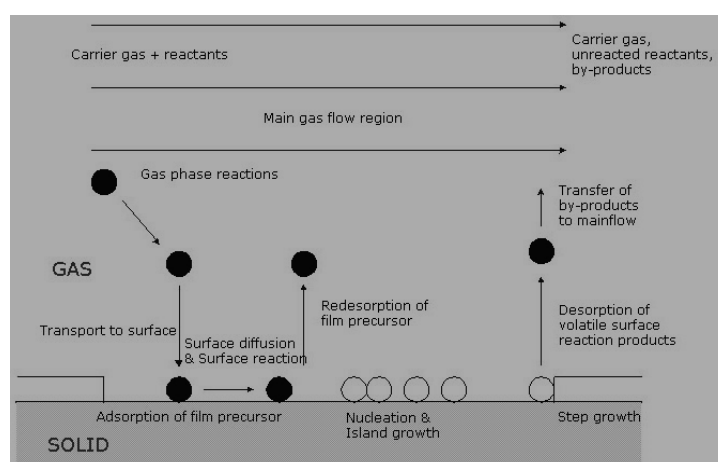


Fig. 2 – Schematic representation of mass and heat transfer in CVD processes.

Of these areas, the fundamental role in the processes of mass transfer boundary layer plays, which is defined as the area adjacent to the substrate surface, where gas differ in speed, chemical composition and temperature of the atmosphere from the rest of the enclosure.

Mass transfer processes taking place at the deposition by CVD is illustrated in Fig. 2. One can distinguish the following stages of filing:

- transport of reactants to the boundary layer (1), caused by convection;
- transport of reactants through the boundary layer (2), the phenomena of diffusion in the gas;
- processes in gas-solid interface (adsorption, germination and phenomena of rearrangement ions and atoms);
- proper growth of the crystals;
- desertion of reaction products (4);
- transport of the product gaseous reaction flask back in the atmosphere (5).

As you can see the main chemical reactions of type (1) above, they are characterized by being mixed reactions, with increasing the number of moles. Therefore, low pressure in the calibrated, the values below the atmospheric pressure will favour the production of these reactions in the desired direction, however, unlike other deposits, the type CVD technology is used only a coarse vacuum pressure in the flask during deposit generally ranging between 200 and 800 mbar abs.

A prerequisite for the success of any deposition by CVD is a reaction using high purity gases. Thus, an impurity gas only 3 ÷ 6 ppm oxygen or water vapor leads to surface oxidation of substrates inside the vacuum, leading in turn to lack of adhesion between coating and substrate.

4. Conditions Imposed Substrates and CVD Layers Properties

Substrate on the carrying place submission must meet the condition that the structure does not change irreversibly deposit temperature and possess sufficient corrosion resistance against the gases used in the process. To obtain a good adhesion of the layer, it is necessary that the substrate surface to be smooth and clean. In general, this area is subject, before filing several stages of cleaning, the last of which took place in the ultrasonic bath. Another condition is compatibility between the coating and substrate.

The set consists of layer and substrate is a true composite. Different expansion coefficients of layer and substrate are responsible for the internal tensions that arise from the cooling temperature and requests submission of the composite thermal shock.

Differences too large expansion coefficients in the layer give rise to a specific defect called "craquelure" which consists of a network of fine cracks. He does not mind very much in those applications where wear is not

accompanied by corrosion. Regarding the shape of the substrate by CVD processes may be covered with layers of high uniformity complex geometry parts including the inner surfaces of fine holes.

Intermetallic compounds, which form the most common layers deposited by CVD are titanium carbide (TiC), titanium nitrides (TiN), chromium carbide (Cr_7C_3), tungsten carbide (W₂C), aluminium oxide (Al_2O_3), iron boride (Fe_xB) and silicon carbide (SiC). All these deposits have thicknesses ranging from 2 to 10 layers such μm . is characterized by a series of specific properties. Of these, the most remarkable is the hardness, which is in most cases large and very large values.

Resistances to oxidation of the fuels are different. Chromium carbide and silicon are stable to oxidation until at least 1000°C , while the titanium carbide to the tungsten and titanium nitrides, oxidation starts already at 540°C .

Tribological behavior of CVD layers is strongly dependent on the material layer on the surface, the hardness of his nature and the couple of materials. The friction abrasive solids the lower friction coefficients present titanium carbide and iron boride largest, as seen from Table 1. In conditions of mixed friction, all couples of materials have low coefficients of friction, but large differences occurred in what the limit of application.

Hardness CVD layers and their low tendency to cold weld formation for obtaining a very high wear resistant type adhesive.

Table 1
Wear and Friction Coefficients of CVD Hard Material Layers

Type layer	Type abrasive friction between solids (2.5N)		Rubbing a composite (50N)		
	Attrition rate	μ	Attrition rate	μ	Pregnancy failure N
	$10^{-6} \text{ mm}^3 / \text{m}$		$10^{-6} \text{ mm}^3 / \text{m}$		
Iron borides	<0.1	0.35 - 0.60	1.5	0.09	≈ 200
Titanium carbide	1.4	0.11 - 0.15	1.0	0.09	> 2400
Titanium nitrides	0.5	0.17 - 0.21		0.1 - 0.06	1000 - 1700
Chromium carbide	8.3	0.30 - 0.50	5.9	0.08	> 2400

Cutting removable cover plates with layers of ICT monophasic, TiN and Ti (C, N) with thicknesses of $3 \div 6$ microns has allowed improving their sustainability $3 \div 5$ times, and covering them with double layers, composed of a phase $3 \div 6$ microns in ICT and a phase $1 \div 3$ μm in Al_2O_3 allowed increasing the sustainability even of 8-10 times compared to uncoated plates.

Corrosion protection exerted by the layers obtained by CVD depends on their porosity and the extent to which these layers are cracked. TiN layers deposited by, although CVD cutting tool gives a high resistance to wear, does not protect the substrate against corrosion requests. Therefore, it is

recommended their use in aggressive environments where pitting occurs frequently. The cause of this adverse reaction is that transition metal nitrides are more electrochemically noble than steel substrate on which they are applied. In itself, the material deposited (TiN) is highly resistant to corrosion and acts as a noble metal. Unfortunately, just because of this, small layer flaws inherent listed by leading to the formation of local galvanic cells between layer and substrate material less noble steel. Therefore, local substrate can be attacked unless nai chemical deposition of TiN is missing. These effects are illustrated in Fig. 3. This raises the effect of detachment of the layer, which annihilate its good mechanical properties.

Porosity layers deposited in vacuum is an inherent consequence of the process of atomic layer growth during submission. After germination, clusters with different orientations simultaneously grow and accommodate mismatches network is realized by the appearance of tension gradient, the areas of defects and vacancies.

If some vacancies are merged, may form microspore. Of course, the greater the size of species condenses the more big pores. If a por extends from substrate to the surface, it is called por entered, and if not, por open.

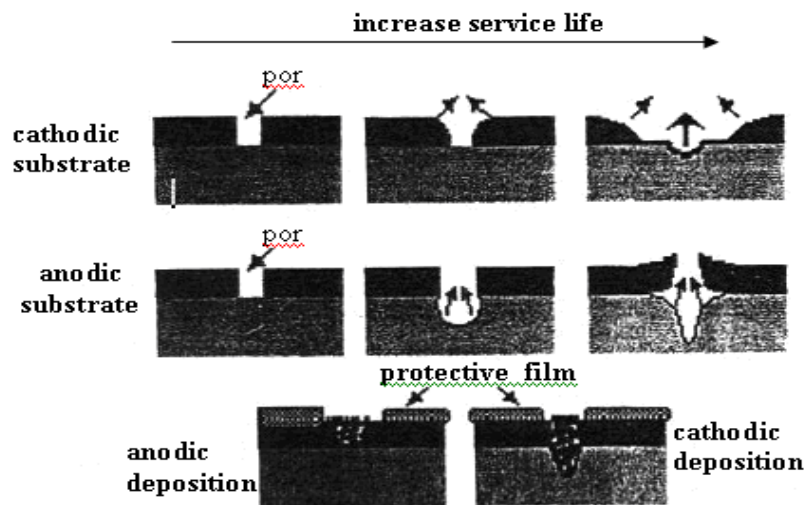


Fig. 3 – Coupling Anodic - cathodes parts covered by a CVD.

In general, macroscopic defects are as a consequence of the surface layer defects, which are responsible for most of the porosity of deposit, although usually these pores are not entered. Local cracks in rosette or local detachment of the layer named „macro porosity”.

5. Conclusions

Hard layers for tribological purposes

The HT-CVD processes, is getting tough layers of ICT, TiN and Al₂O₃ on sintered carbide tools. Since 1980, we achieved the ICT and TiN deposition by low temperature CVD processes (MOCVD, PACVD) and high alloyed tool steels. The increase in the durability of tools for different types of layers deposited by CVD processes.

O items also special tribological properties of CVD deposition, published recently, is represented by soft layers with high adhesion to substrate, which have lubricating effect, characterized by low coefficients of friction and their affinities reduced compared to alloying elements. In this category are a series of monometallic layers, such as Al, Ti, Cu, precious metals.

Received: May 14, 2010

“Gheorghe Asachi” Technical University of Iași
e-mail: irina.surdu@yahoo.com

REFERENCES

1. Pedraza F., Gómez C., Carpintero M.C., Hierro M.P., Pérez F.J., Surf. Coat. Technol., **190**, 2–3, 223 (2005).
2. Voudouris N., Chistoglou C.H., Angelopoulos G.N., Surf. Coat. Technol., *141*, 275 (2001).
3. Chistoglou C., Voudouris N., Angelopoulos G.N., Pant M., Dahl W., Surf. Coat. Technol., *184*, 149 (2004).
4. Pérez F.J., Hierro M.P., Carpintero M.C., Bolivar F.J., Surf. Coat. Technol., *184*, 361 (2004).
5. Choy K.L., Prog. Mater. Sci., *48*, 57 (2003).
6. Leclere K., Briens C., Gauthie T., Bayle J., Guigon P., Bergougnou M., *Experimental Measurement of Droplet Vaporization Kinetics in a Fluidized Bed*. Chem. Engng. A. Proc., **43**, 693 (2004).
7. Bruhns S., Werther J., *An Investigation of the Mechanism of Liquid Injection Into Fluidized Beds*. AIChE J., **51**, 3, 766 (2005).

CE ESTE DEPURAREA CHIMICĂ DE VAPORI (C-CVD)?

(Rezumat)

Analizând evoluția procesului de depunere chimică de vapori de la început până la etapa actuală. Depunerea chimică de vapori (CVD) este un proces chimic

utilizat pentru producerea de puritate înaltă, materiale de înaltă performanță. Procesul este adesea utilizat în industria de semiconductori pentru a produce filme subțiri. Într-un proces tipic CVD, substratul este expus la unul sau mai multi precursori volatili, care reacționează și/sau se descompune pe suprafața substratului pentru producerea depozitului dorit.